

GC  
7.1  
F85  
1980

OBSERVATIONS AND MODELS OF  
INERTIAL WAVES  
IN THE DEEP OCEAN

by

LEE-LUENG FU

B.S., National Taiwan University  
(1972)

SUBMITTED IN PARTIAL FULFILLMENT  
OF THE REQUIREMENTS FOR THE  
DEGREE OF DOCTOR OF  
PHILOSOPHY

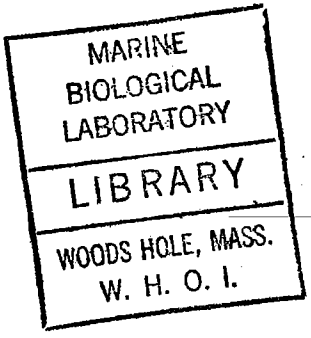
at the

MASSACHUSETTS INSTITUTE OF TECHNOLOGY

and the

WOODS HOLE OCEANOGRAPHIC INSTITUTION

February, 1980



© Massachusetts Institute of Technology 1980

Signature of Author Lee-lueng Fu

Joint Program in Oceanography, Massachusetts Institute  
of Technology-Woods Hole Oceanographic Institution, and  
Department of Meteorology, Massachusetts Institute of  
Technology, February, 1980.

Certified by Carl Wunsch

Thesis supervisor

Accepted by M. Edmond

Chairman, Joint Oceanography Committee in Earth  
Sciences, Massachusetts Institute of Technology-  
Woods Hole Oceanographic Institution.

OBSERVATIONS AND MODELS OF INERTIAL WAVES  
IN THE DEEP OCEAN

by

Lee-Lueng Fu

Submitted to the Massachusetts Institute of Technology-  
Woods Hole Oceanographic Institution Joint Program in  
Oceanography on December 7, 1979 in partial fulfillment  
of the requirements for the degree of Doctor of Philosophy

Abstract

The structure of the inertial peak in deep ocean kinetic energy spectra is studied here. Records were obtained from Polymode arrays deployed in the Western North Atlantic Ocean ( $40^{\circ}\text{W}$  to  $70^{\circ}\text{W}$ ,  $15^{\circ}\text{N}$  to  $42^{\circ}\text{N}$ ). The results are interpreted both in terms of local sources and of turning point effects on internal waves generated at lower latitudes.

In most of the data, there is a prominent inertial peak slightly above  $f$ ; however, the peak height above the background continuum varies with depth and geographical environment. Three classes of environment and their corresponding spectra emerge from peak height variations: class 1 is the 1500 m level near the Mid-Atlantic Ridge, with the greatest peak height of 18 db; class 2 includes (a) the upper ocean (depth less than 2000 m), (b) the deep ocean (depth greater than 2000 m) over rough topography, and (c) the deep ocean underneath the Gulf Stream, with intermediate peak height of 11.5 db; class 3 is the deep ocean over smooth topography, with the lowest peak height of 7.5 db. Near  $f$ , the horizontal coherence scale is  $O(60\text{ km})$  at depths from 200 m to 600 m, and the vertical coherence scale is  $O(200\text{ m})$  just below the main thermocline.

A one turning point model is developed to describe inertial waves at mid-latitudes, based on the assumption that inertial waves are randomly generated at lower latitudes (global generation) where their frequency-wavenumber spectrum is given by the model of Garrett and Munk (1972 a, 1975). Using the globally valid wave functions obtained by Munk and Phillips (1968), various frequency spectra near  $f$  are calculated numerically. The model yields a prominent inertial peak of 7 db in the horizontal velocity spectrum but no peaks in the temperature spectrum. The model is latitudinally dependent: the frequency shift and bandwidth of the inertial peak decrease with latitude; energy level near  $f$  is minimum at about  $30^{\circ}$  and higher at low and high latitudes. The observations of class 3 can be well-described by the model; a low zonal wavenumber cutoff is required to produce the observed frequency shift of the inertial peak.

The differences between the global generation model and the observations of class 1 and class 2 are interpreted as the effects of local sources. A locally forced model is developed based on the latitudinal modal decomposition of a localized source function. Asymptotic eigensolutions of the Laplace's tidal equation are therefore derived and used as a set of expansion functions. The forcing is through a vertical velocity field specified at the top or bottom boundaries of the ocean. For white noise forcing, the horizontal velocity spectrum of the response has an inertial peak which diminishes in the far-field. With the forcing located at either the surface or the bottom, several properties of the class 2 observations can be described qualitatively by a combination of the global and local models.

The reflection of inertial waves from a turbulent benthic boundary layer is studied by a slab model of given depth. Frictional effects are confined to the boundary layer and modelled by a quadratic drag law. For given incident waves, reflection coefficients are found to be greater than 0.9 for the long waves which contain most of the energy. This result suggests that energy-containing inertial waves can propagate over great distance as is required by the validity of the model of global generation.

Thesis Supervisor : Carl Wunsch  
Title : Cecil and Ida Green Professor of  
Physical Oceanography  
Chairman, Department of Earth and  
Planetary Sciences

Acknowledgements

I wish to thank Professor Carl Wunsch of M.I.T., my thesis supervisor, for his introducing me to this research field and for his constant guidance and encouragement through this work. Without his illuminating comments on the presentation of this work, this thesis would be much less readable.

I thank Dr. Nicholas Fofonoff of W.H.O.I. for his careful review of this manuscript and constant encouragement through my graduate study. I am grateful to Professor Glenn Flierl of M.I.T. and Dr. Nelson Hogg of W.H.O.I. for several valuable discussions and critical reviews of this manuscript. I thank Dr. Melbourne Briscoe of W.H.O.I. for discussions and comments on this manuscript. I thank Professor Charles Eriksen of M.I.T. for discussions.

I thank Professor Walter Munk of Scripps Institution of Oceanography for his comments on this manuscript.

I am grateful to Dr. William Schmitz and the Buoy Group of W.H.O.I. for providing unpublished data for the use in this study.

I thank Dr. Thomas Sanford of the University of Washington for his generosity to share some unpublished results with me. I am also grateful to Professor Peter Niiler of Oregon State University for allowing me to use his unpublished data (PMIII C).

I thank Charmaine King and Barbara Grant of M.I.T. for their programming assistance for most of the computation in this study.

Above all others, I wish to express my special thanks to my dear wife, Cecilia, for her endless encouragement and self-sacrifice as being a graduate student's wife. To her I owe so much.

This work was supported by the National Science Foundation through grant OCE 76-80210 and its continuation OEE 78-19833.

To Cecilia

Table of Contents

	<u>Page</u>
Abstract .....	2
Acknowledgements .....	4
List of Figures .....	9
Chapter 1 Introduction .....	13
Chapter 2 Spectral Description of Inertial Waves in the Western North Atlantic	
2.1 Introduction .....	23
2.2 Data base and analysis procedure .....	23
2.3 The observed spectra .....	30
2.3a Variability and classification .....	35
2.3b Frequency shift of the inertial peak .....	40
2.3c Bandwidth .....	42
2.3d Rotary spectrum .....	45
2.4 Coherences .....	48
2.4a Horizontal separation .....	48
2.4b Vertical separation .....	53
2.5 Summary .....	57
Chapter 3 Theory of Low Frequency Internal Waves on a Rotating Sphere	
3.1 Dynamical equations .....	59
3.2 The traditional approximation .....	61
3.3 Asymptotic solutions .....	63
3.4 The WKBJ approximation .....	72
3.5 Discussion .....	74

Table of Contents (contd.)

	<u>Page</u>
Chapter 4    A Model Spectrum for the Global Inertial Wave Field	
4.1 Introduction .....	75
4.2 The Garrett and Munk model .....	76
4.3 The global inertial wave model	
4.3a Normalization .....	79
4.3b Construction of frequency spectra .....	80
4.3c Model results and their sensitivity .....	84
4.4 Comparisons with observations	
4.4a Horizontal kinetic energy spectrum .....	99
4.4b Potential energy spectrum .....	105
4.4c Rotary spectrum .....	105
4.5 Latitudinal limits of the model .....	105
4.6 Summary and discussion .....	111
Chapter 5    A Forced Model for the Local Inertial Wave Field	
5.1 Introduction .....	114
5.2 The model and methods of solutions .....	118
5.3 Asymptotic solutions of Laplace's tidal equations in the parameter regime of inertial waves	
5.3a Introduction .....	125
5.3b Solutions .....	126
(i) Positive modes .....	127
(ii) Negative modes .....	137
5.4 Results .....	139
5.4a Surface forcing .....	147

Table of Contents (contd.)

	<u>Page</u>
5.4b Bottom forcing .....	157
5.5 Summary and discussion .....	160
Chapter 6 The Reflection of Inertial Waves from the Benthic Boundary Layers	
6.1 Introduction .....	162
6.2 The model .....	164
6.3 Results .....	171
6.4 Summary and discussion .....	177
Chapter 7 Conclusions .....	181
Appendix A Temperature Spectra in the Inertial Frequency Band ....	185
A.1 Advection of horizontal temperature gradient by inertial waves .....	187
A.2 Mooring motion in the inertial frequency band .....	189
A.3 Summary .....	191
Appendix B Evaluation of Elliptic Integrals with Parameters Greater than One .....	192
References .....	196
Biographical Note .....	202



List of Figures

	<u>Page</u>
Figure 2.1 Mooring positions and topography. Stations in rough areas are enclosed with square boxes for identification. ....	24
Figure 2.2 Spectra of u and v components at 600 m at Station 5 of the PMII. CPH represents cycle per hour. The straight line represents the power law $E_0 N \omega^{-p}$ with $N = 2.27$ cph, $E_0 = 0.096 \text{ cm}^2/\text{sec}^2/\text{cph}^2$ , and $p = 2.23$ . Shown on the bottom are the 95 % confidence intervals. ....	31
Figure 2.3 Normalized horizontal kinetic energy spectra at (a) Station 3 of the PMII (smooth topography) and (b) Station 546 of the PMI (rough topography). Error bar is 95 % confidence limit. ....	36
Figure 2.3c As in Fig. 2.3 except at Station 623 of the PMIII cluster B (near the Mid-Atlantic Ridge, very rough topography). ....	37
Figure 2.4 Histogram of the peak height (PH) distribution. ....	39
Figure 2.5 Normalized horizontal kinetic energy spectrum at 4000 m, Station 6, PMII. The straight line represents the power law fit. Error bar is 95 % confidence limit. ....	41
Figure 2.6 Ratio of the peak frequency $\omega_p$ to f against instrument depth. Upper panel is for smooth topography areas; lower panel is for rough topography areas. Special symbols : X -- measurements underneath the Gulf Stream; + -- PMIII C. Dashed lines represent the frequency resolution limits associated with $\omega_p/f = 1$ . ....	43
Figure 2.7 $\omega_p/f$ against peak height (PH) at 4000 m. Dashed lines are the same as in Fig. 2.6. ....	44
Figure 2.8 Rotary spectra of the same record as in Fig. 2.2. $E_-$ -- clockwise component; $E_+$ -- counter-clockwise component. ....	46
Figure 2.9 $E_-/E_+$ against peak height (PH). " X " represents the stations roughly along $28^\circ\text{N}$ . ....	49
Figure 2.10 Clockwise component coherence and phase between Stations 1 and 2 of the PMII at 600 m. Arrows represent the location of f. Dashed lines in the coherence plot are the 95 % confidence levels of no significance. ....	51
Figure 2.11 Clockwise component coherence against horizontal separation : (a) at upper levels from 200 m to 600 m; (b) at 4000 m. Special symbols : + -- PMI ; • -- PMII ; o -- PMIII A ; Δ -- PMIII B ; X -- PMIII C. Dashed lines are the 95 % confidence levels of no significance. ....	52

List of Figures (contd.)

	<u>Page</u>
Figure 3.1 Turning latitudes of waves with $\sigma = 0.5878$ as functions of zonal wavelength for different vertical modes. The number next to each curve is the mode number. Dashed line indicates the inertial latitude ( $36^\circ$ ). . . . .	69
Figure 3.2 Schematic diagram showing the variation of the wave function $V$ with respect to $k$ and $\epsilon$ . Horizontal axis is the sine of latitude; $\sigma$ corresponds to the inertial latitude. $k \nearrow$ means increasing the value of $k$ . . . . .	71
Figure 4.1 Schematic representation of the zonal wavenumber spectra of (a) Model 1 and (b) Model 2. . . . .	85
Figure 4.2 Model normalized spectra of (a) horizontal kinetic energy and (b) potential energy at five latitudes, with $D(k, j, \omega)$ given by Model 1, $m = 20$ , $j_* = 6$ , $t = 2.5$ , and $E_0/N_0 = 0.03$ $\text{cm}^2/\text{sec}^2/\text{cph}^2$ . The numbers are latitudes in deg.; the vertical bars indicate the locations of $f$ . . . . .	87
Figure 4.3 Model normalized spectra of horizontal kinetic energy (solid line) and potential energy (dashed line) at $32^\circ$ , with $D(k, j, \omega)$ given by Model 2 and the other parameters the same as in Fig. 4.2. . . . .	88
Figure 4.4 Model results of $\text{Log}(P.E./H.K.E.)$ at the same latitudes and with the same model parameters as in Fig. 4.2. The envelope of the curves represents the WKBJ result. . . . .	92
Figure 4.5 Model rotary spectra at $32^\circ$ with the same model parameters as in Fig. 4.2 . . . . .	93
Figure 4.6 Model results of $\text{Log}(E_-/E_+)$ , i.e., $\Gamma$ , at the same latitudes and with the same model parameters as in Fig. 4.2. The envelope curve is the WKBJ result. . . . .	94
Figure 4.7 Model normalized horizontal kinetic energy spectra at $32^\circ$ with different values of $j_*$ . Other model parameters are the same as in Fig. 4.2. The arrow indicates the local $f$ . . . . .	96
Figure 4.8 As in Fig. 4.7 except for different values of $t$ . . . . .	97
Figure 4.9 As in Fig. 4.7 except for different values of $m$ (number of modes summed). . . . .	98
Figure 4.10 Model (smooth curves) and observed normalized spectra of H.K.E. at 4000 m. Latitude, station number, and 95 % confidence error bar for each record are shown. . . . .	100

List of Figures (contd.)

	<u>Page</u>
Figure 4.11 As in Fig. 4.10 except for potential energy. 95 % confidence error bar is the same for each record. ....	106
Figure 5.1a Eigensolutions of v-velocity (upper one) and pressure (lower one) with $\sigma = 0.5878$ , $k = 50$ , $n = 63$ , and $\epsilon_n^{1/2} = 370.2$ . ....	135
Figure 5.1b As in Fig. 5.1a except that $k = -50$ , and $n = 62$ . ....	136
Figure 5.2a As in Fig. 5.1a except that $n = 31$ and $(-\epsilon_n)^{1/2} = 573.1$ . .	140
Figure 5.2b As in Fig. 5.1a except that $n = 31$ , $(-\epsilon_n)^{1/2} = 573.1$ , and $k = -50$ . ....	141
Figure 5.3 The forcing function $\hat{w}_b(\phi)$ (solid curve) and its expansion in terms of $P_{n,\sigma}$ (symbols) for (a) $\sigma = \sin \phi_0$ and (b) $\sigma = 1.12 \sin \phi_0$ , where $\phi_0 = 36^\circ$ and the forcing scale $L = 300$ km. ....	145
Figure 5.4 Response spectra of (a) w-velocity and (b) v-velocity at four different depths (numbers are in meters). The unit of the vertical axis is $\text{cm}^2/\text{sec}^2/\text{cph}$ . The forcing is imposed at the surface ( $z_b = 0$ ) with $L = 300$ km and $\phi_0 = 36^\circ$ . A straight line representing the $\omega^{-2}$ spectrum is drawn for reference. ....	148
Figure 5.5 As in Fig. 5.4 except that $L = 150$ km. ....	150
Figure 5.6 As in Fig. 5.4 except that $L = 75$ km. ....	151
Figure 5.7 Schematic diagram showing the ray paths of the local wave field (dashed lines) and the global wave field (solid lines). A mooring with two current meters measuring the wave field is also shown. ....	153
Figure 5.8 Response spectra of v-velocity at (a) $15^\circ$ and (b) $50^\circ$ , with $L = 150$ km. ....	155
Figure 5.9 As in Fig. 5.4 except for bottom forcing ( $z_b = -1$ ) and $L = 150$ km. ....	158
Figure 5.10 Response spectra of v-velocity with both surface forcing ( $ \hat{w}_b ^2 = 2 \times 10^{-3} \text{ cm}^2/\text{sec}^2/\text{c.p.}2\Omega$ ) and bottom forcing ( $ \hat{w}_b ^2 = 8 \times 10^{-3} \text{ cm}^2/\text{sec}^2/\text{c.p.}2\Omega$ ). ....	159
Figure 6.1 Schematic diagram showing two different interpretations of the observed dominance of downward energy propagation of inertial waves. The left figure is Leaman's (1976), and the right figure is ours. The arrow represents the direction of propagation and its length is proportional to the corresponding amount of energy. ....	163

List of Figures (contd.)

	<u>Page</u>
Figure 6.2 Schematic diagram of the model configuration. Solid arrows represent the ray paths and their directions of propagation; dashed arrows represent the directions of phase propagation. ....	165
Figure 6.3 $r$ and $d$ as functions of frequency for different values of vertical wavelength (labelling numbers are equivalent mode numbers). ....	173
Figure 6.4 As in Fig. 6.3 except for different values of the mixed layer depth $D$ (numbers are in meters). ....	175
Figure 6.5 As in Fig. 6.3 except for different values of the buoyancy frequency $N_b$ (in cph) on top of the mixed layer. ....	176
Figure 6.6 As in Fig. 6.3 except for different values of the drag coefficient $C_D$ . ....	178
Figure 6.7 As in Fig. 6.3 except for different values of the incident wave amplitude $ \hat{u}_i $ (in m/sec). ....	179
Figure A.1 Temperature spectra at 600 m at Station 1 (36°N, 55°W), and at 3500 m at Station 7 (31.6°N, 55°W) of the PMII. Arrows showing the location of the local $f$ ; error bar showing the 95 % confidence interval. ....	186
Figure A.2 Pressure spectrum of Record 5482 (31°N, 60°W) at 800 m. ....	188

Chapter 1 Introduction

Inertial waves (sometimes called inertial oscillations, or inertial motions, etc.) have been observed in the ocean for almost half a century (for a historical review see Webster, 1968). They are characterized as a transient rotation (clockwise in the Northern Hemisphere) of horizontal current with frequency near the local inertial frequency  $f$ , defined as  $2\Omega \sin \phi$ , where  $\Omega$  is the rotational frequency of the earth and  $\phi$  is latitude. Webster (1968) documented their world-wide existence at all depths and described their general properties. In his words, inertial waves are "essentially transient phenomena of thin vertical extent". Their coherence scale is at least several kilometers in the horizontal (Webster, 1968 ; Schott, 1971) but only a few tens of meters in the vertical (Webster, 1968 ; Fomin and Savin, 1973). In frequency space, inertial waves are represented by a rather broad spectral peak located slightly above  $f$ ; they are the most energetic components of the internal wave field. One of the important recent observations of inertial waves was their vertical phase propagation reported by Sanford (1975) and Leaman and Sanford (1975). They showed evidence of a dominant upward phase propagation with near-inertial periods in their profiler measurements in the open ocean. The same feature has also been observed in near-shore regions (Johnson et al, 1976; Kundu, 1976) and shallow seas (Fomin and Yampol'skiy, 1975). These findings constitute direct evidence for the interpretation of inertial waves as propagating internal waves. In the atmosphere, inertial waves have not been observed in the troposphere; however, evidence of their existence and downward

phase propagation in the stratosphere has been recently reported by Thompson (1977). Thus the observed helical vertical structures of ionospheric winds at heights from 90 km to 150 km (Rosenberg, 1968) may be indeed manifestations of inertial waves generated in the lower atmosphere as proposed by Moses (1971).

The importance of inertial waves as transient response of the ocean to impulsive external forcing has been recognized for a long time (e.g., Rossby, 1938; Pollard, 1970). Hence knowledge of inertial waves is crucial to the understanding of the energetics of ocean circulation as the result of atmospheric forcing. On the other hand, recent work on resonant interactions of internal waves (e.g., Olbers, 1976; McComas and Bretherton, 1977) suggests that inertial waves are important in internal wave dynamics at mid-latitudes: low vertical wavenumber inertial waves serve as an energy source for high frequency waves with relatively high wavenumbers through a diffusive mechanism in wavenumber space; high vertical wavenumber inertial waves serve as an energy sink for waves with twice the frequency and relatively low wavenumbers as the result of subharmonic instability, and the energy then is dissipated through the mechanism of shear instability. Garrett and Munk (1972 b) have shown that the shear instability in the latter case could be an important dissipation mechanism for oceanic internal waves and hence provide the turbulent mixing energy in the thermocline. Disturbances caused by the internal wave field in which inertial waves are most energetic are the major sources of noise in undersea acoustic communications; hence the study of inertial waves also has its important military and commercial applications.

In the last decade, research in oceanic internal waves was greatly enhanced by the advent of the frequency-wavenumber spectrum ( $f$ - $w$  spectrum hereafter) developed by Garrett and Munk (1972 a, 1975). With the synthesis of a great number of observations, they deduced a universal model spectrum for internal waves in the deep ocean using linear dynamics under the hypothesis of horizontal isotropy and vertical symmetry of the wave field. This attempt to estimate the complete energy spectrum of internal waves from existing observations led to the design of critical experiments such as the Internal Wave Experiment (IWEX; Briscoe, 1975) to directly measure the wave field in frequency and wavenumber space. The results reported by Müller et al (1978) have confirmed the general validity of the Garrett-Munk model (GM model hereafter) in the frequency regime away from  $f$ ,  $N(z)$ , and the tidal frequencies ( $N(z)$  is the buoyancy frequency at depth  $z$ ). The problem at  $f$  is two-fold: theoretically, the WKBJ approximation of wave functions underlying the GM model fails near  $f$ , which is a latitudinal turning point; observationally, the IWEX record is too short (40 days) to draw statistically significant conclusions with sufficient resolution near  $f$ . The latter limitation also explains the general lack of a detailed spectral description of inertial waves after so many years' proliferation of moored measurements. For example, a frequency resolution of the order of two percent of  $f$  at mid-latitudes requires six months' data to obtain five degrees of freedom for spectral estimates. Most pre-Polymode (for a description of Polymode see US POLYMODE Organizing Committee, 1976) observations simply do not meet this requirement. Because the Polymode arrays were originally designed

to study the variability of meso-scale eddy field in the North Atlantic, there was at least nine months' continuous record at each mooring site. Thus, the Polymode arrays have provided an excellent data base for us to attempt an up-to-date spectral description of inertial waves in a wide-range of latitude and geographical environment in a typical open ocean. Such a description is presented in Chapter 2 with emphases on the answers to the following questions:

- (a) Is there a universal frequency spectrum near  $f$  in the deep ocean? If not, how does the spectrum vary with the physical environment (instrument depth, topography, etc.) ?
- (b) What are the coherence scales of inertial waves in the deep ocean ? Are they consistent with existing theories and observations ?

Because this study is confined to inertial waves in the ocean interior (we will call it the "deep ocean"), i.e., away from both the horizontal and vertical boundaries, those data within 100 m from either the surface or the bottom were excluded from the discussion. Due to the fact that in the inertial frequency band moored temperature measurements are subject to possible contamination from both the mooring motion and horizontal advection (discussed in Appendix A), the descriptions in Chapter 2 are restricted to velocity data only.

The failure of the WKBJ approximation also accounts for the inaccuracy of the GM model near  $N(z)$ , which is a vertical turning point. Using an exponential  $N(z)$ , Desaubies (1975) derived uniformly valid vertical wave functions with a single turning point to remove this



apparent singularity and to successfully describe observed spectra near  $N(z)$ . Eriksen (1978) used a two turning point model to describe high frequency waves trapped in the main thermocline. Thus by using appropriate latitudinal wave functions, we can proceed in the same way to describe the observed spectra near  $f$  in terms of the GM model. Latitudinal wave functions with global validity were obtained by Munk and Phillips (1968; MP hereafter). They used the spheroidal wave equation to approximate the Laplace's tidal equation and obtained approximate one turning point solutions which are valid globally with error terms no greater than  $O(\epsilon^{-1/3})$ , where  $\epsilon$  is a large parameter ( $\geq 10^5$ ). For the description of mid-latitude inertial waves which are our major concerns, the one turning point solutions are appropriate because the waves are unlikely to form latitudinal modes by phase locking between the two turning latitudes. However, at low latitudes where there is strong evidence for the existence of latitudinal modes (Wunsch and Gill, 1976), two turning point solutions must be used. Using equatorial modes on a beta plane, Eriksen (1979) developed a spectral model for equatorially trapped waves.

The latitudinal wave functions of horizontal velocity obtained by MP are proportional to the Airy function which is evanescent poleward (oscillatory equatorward) of the turning latitude. The Airy function reaches its maximum when the argument is slightly above zero. Thus, by using these wave functions in the construction of various frequency spectra, one would expect to obtain a spectral peak slightly above  $f$  in the horizontal velocity spectrum simply due to the kinematic turning point effects on internal waves, without the need of a specific forcing

mechanism. The possible use of such a model to account for the observed inertial peak was independently noticed in a recent review paper by Garrett and Munk (1979), and has been investigated using a beta plane model by Munk (1979).

With the appropriate wave functions available, an adequate f-w spectrum is needed to calculate various spectral quantities. Munk and Phillips (1968) attempted to calculate the velocity spectrum using a crude model of the f-w spectrum, with a relatively weak inertial peak in the resulting spectrum. Today a decade later, detailed knowledge of the f-w spectrum near f is still lacking. The GM model is not applicable near f; nevertheless, it is a good description of high frequency waves far from f, i.e., far from their turning latitudes. Hence the part of the inertial wave energy which results from random sources sufficiently equatorward of the observation site can be readily calculated using the GM model. Under the assumption of linear propagation, all the low frequency internal waves can be traced to the equator where the  $\omega^{-2}$  GM frequency spectrum is valid over an extensive frequency range. Thus, once the f-w spectrum at the equator is known, we can, in principle, calculate the spectrum at all latitudes and obtain a unified interpretation of measurements at different latitudes. It is quite reasonable to define this part of the inertial wave field as the "global wave field". However, with a beta plane model whose validity is restricted to low latitudes, such calculations would be very inaccurate.

Apart from the random global generation mechanism, it is well known that the local wind could be an effective source for inertial waves in

the upper ocean. Ekman (1905) in his classical paper showed that inertial waves could be generated by changes in the wind field. Rossby (1938) pointed out that inertial waves could be generated as transients during the flow adjustment toward geostrophic equilibrium. Using a two-layer model with a body force acting on the upper layer, Veronis (1956) showed that inertial waves were most efficiently generated by an impulsive wind field. Pollard (1970) refined Veronis' model to include continuous stratification and showed that the amplitudes of wind-generated inertial waves were realistic at the surface but too small to account for the maximum amplitude observed in the deep ocean. Furthermore, Pollard and Millard (1970) demonstrated that observed inertial currents in the surface layer could indeed be simulated by their model using local wind data. Using a different approach, Kroll (1975) considered the forcing imposed by a vertical velocity field which resulted from the divergence of a viscous Ekman layer generated by surface winds. For sudden onset of the wind field, inertial oscillations were generated in the Ekman layer with frequencies slightly above  $f$ ; these disturbances radiated downward along their ray paths which Kroll derived from a beta plane model. Because the wave amplitudes generally increase with decreasing forcing scale which enhances the divergence of the Ekman layer, small scale severe storms (scale  $\sim 100$  km, stress  $\sim 10$  cm<sup>2</sup>/sec<sup>2</sup>) could, in Kroll's model, give wave amplitudes of 10 cm/sec at great depths. But the forcing used in Pollard's model is the wind stress itself, not its curl, and hence is insensitive to forcing scales; even for a wind stress of 10 cm<sup>2</sup>/sec<sup>2</sup>, the maximum speed at great depths is only order 1 cm/sec.

In the context of wave-current interaction, Stern (1977) showed that deep inertial waves could be reinforced by surface wind through an over-reflection mechanism at the base of the mixed layer. Ageostrophic instability of the mean flow as a local source for inertial waves is currently being investigated by Tai (ongoing PhD thesis, Harvard University).

The observed dominance of downward energy (upward phase) propagation with near-inertial frequencies is a direct evidence of significant local generation (Leaman and Sanford, 1975). It seems relevant to define a "local wave field" to represent these inertial waves which are forced by some specific local sources. The distinction between the global and local wave field is that, the latter is generated locally as inertial waves, whereas the former is generated at lower latitudes as super-inertial internal waves, which are well described by the GM model and only appear as inertial waves when they reach their turning latitudes. As pointed out in MP, the observed inertial wave energy is most likely a mixture of these two sources. To distinguish these two contributions from each other in moored measurements is the main task of this study. The first step is to calculate a model spectrum for the global wave field using globally valid wave functions and the GM model.

In Chapter 3, the general theory of low frequency internal waves on a rotating sphere is reviewed. In Chapter 4, the construction of a model spectrum for the global wave field is presented; its limitations and sensitivities to model parameters are discussed; comparisons between the model and observations are made with the differences interpreted as the

contribution from local sources.

In order to explain the observed spectra in terms of forced waves, we need the oceanic response spectrum for a specified forcing spectrum. The ratio of these two is usually called the transfer function. Because most of the existing models of this kind are based on the  $f$ -plane approximation, a spurious infinite response at the inertial frequency usually occurs. For instance, using a balance between wind generation and dissipation by vertical friction, Käse and Tang (1976) derived a response spectrum which had an infinite cusp at  $f$ . However, this apparent singularity can be removed by including the variation of  $f$  with latitude (i.e., the beta effect) in the equations of motion. In Chapter 5, the spectral response of the ocean to a highly idealized forcing is derived, using asymptotic eigenfunctions of the Laplace's tidal equation. The purpose is to explain the qualitative difference between some of the observed spectra and the global wave model.

The existence of the global wave field requires that the dissipation of low frequency waves, especially those energetic long waves, be small enough. Presumably most of the dissipation of these waves with large vertical wavelengths is taking place near the bottom. Because most of the existing models (e.g. Phillips, 1963; Leaman, 1975) of the reflection of near-inertial waves off rigid boundaries are of laminar Ekman layer type, they become singular (boundary layer depth is of order one) when  $\omega \approx f$ . However, the benthic boundary layer is turbulent and of small depth -- of order 20 m (c.f. Wimbush and Munk, 1970; Armi and D'Asaro, 1979); its dynamics are different from the ocean interior and this should be taken into account. A simple model is presented in

Chapter 6 to describe the possible effects of the benthic boundary layer on the reflection of inertial waves propagating from a laminar, inviscid interior. A slab model is used to describe the boundary layer and the frictional effects are modelled by a conventional quadratic drag law. The major purpose is to calculate the resulting reflection coefficient and to assess the possibility of the existence of the global wave field.

Conclusion and discussion appear in Chapter 7.

## Chapter 2 Spectral Description of Inertial Waves in the Western North Atlantic

### 2.1 Introduction

The major purpose of this chapter is to describe the internal wave spectrum based on long term (usually  $\geq 9$  months) moored current velocity data. These data are primarily from various Polymode arrays located in the Western North Atlantic. The emphasis is in the inertial frequency band; with sufficient frequency resolution, characteristics of the inertial peak -- energy level, frequency, and bandwidth -- were analyzed to study their variability; spatial coherences were calculated wherever there were closely spaced instruments, and coherence scales (both horizontal and vertical) were estimated. Theoretical interpretation of these observational results is the main task of later chapters.

### 2.2 Data base and analysis procedure

Listed in Tables 2.1 and 2.2 are the moored current velocity data used in this study. All of them are from the Polymode Array I, II, and III (PMI, PMII, PMIII hereafter) except mooring 520, which is part of the Muir Seamount Experiment (c.f. Wunsch, 1976). There are altogether thirty-five stations and ninety-nine instrument levels. The mooring positions and topography (from Uchupi, 1971) are displayed in Fig. 2.1. The area covers approximately twenty-seven degrees of latitude (from  $15^{\circ}\text{N}$  to  $42^{\circ}\text{N}$ ) and a variety of topographic features : abyssal plains, seamounts, mid-ocean ridge and its associated fracture zones.

At each instrument level of the Polymode arrays, there is at least one segment of continuous data of approximately eight months duration.

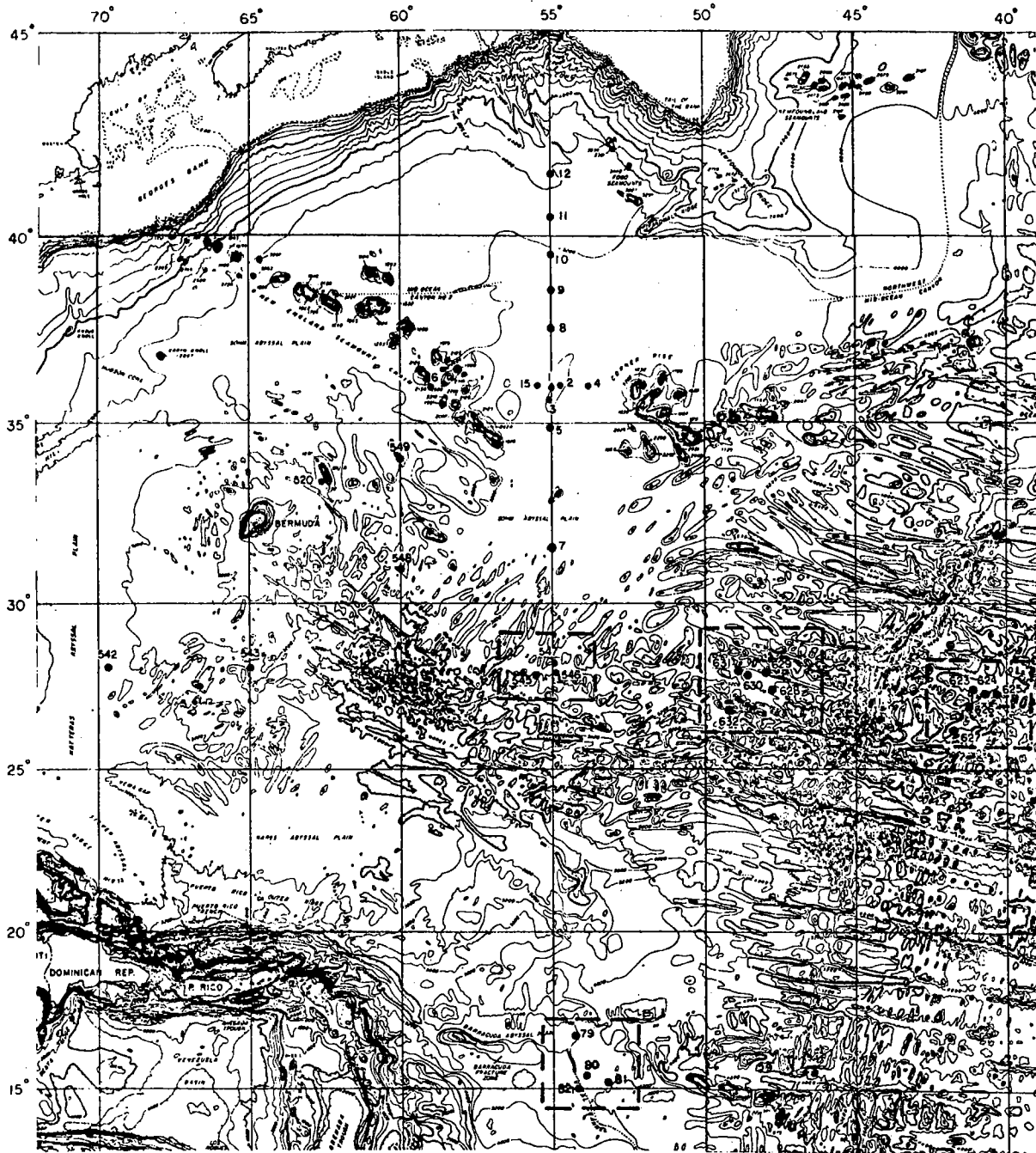


Figure 2.1 Mooring positions and topography. Stations in rough areas are enclosed with square boxes for identification.



Table 2.1

Tabulation of Records From the Polymode Array II. Latitudes are North, Longitudes West (in deg). Depths Are in Meters, Data Lengths in Hours. Record ID are WHOI Designation Numbers.

Station # (latitude, longitude) water depth	Record ID	Instrument Depth	Data Length	$\Delta\omega/f$	PH(db)	$\omega_p/f$	Class
1 (35.9, 55) 5054	5571	6081	5460 x 2	.05	14	1.05	2a
	5573	6083	4320 x 3	.13	10.5	.99	2a
	5575	6085	5460 x 3	.18	9.5	.99	2a
	55710	58310	5460 x 2	.05	7.5	1.02	3
2 (36, 54.7) 5318	5791	6001	5664 x 2	.1	11	1.03	2a
	5793	6003	"	.15	11	.96	2a
	5794	6004	"	.05	11	1.00	2a
	5589	6006	5312 x 3	.15	6.5	1.08	3
3 (35.6, 55.1) 5115	5651	6091	5336 x 3	.1	11.5	1.05	2a
	5653	6093	5336 x 2	.04	15	1.00	2a
	5654	6094	"	.03	12.5	1.00	2a
	5656	6096	"	.13	7.5	1.03	3
4 (36, 53.8) 5467	5591	6011	5280 x 3	.1	9	1.01	2a
	5783	6013	5640 x 2	.07	12.5	1.01	2a
	5594	6014	5280 x 3	.05	9.5	1.02	2a
	5595	6015	4300 x 3	.14	8	1.13	3
5 (34.9, 55) 5506	5661	6111	5320 x 3	.05	13.5	.99	2a
	5663	6113	"	.1	12	.99	2a
	5664	6114	5312 x 3	.11	10	.99	2a
	5665	5815	5312 x 2	.1	6.5	1.08	3

Table 2.1 (cont'd.)

Station # (latitude, longitude) water depth	Record ID	Instrument		Data Length	$\Delta\omega/f$	PH(db)	$\omega_p/f$	Class
		Depth						
6 (35.9, 59) 5206	5681	600		5220 x 1	.1	10	.98	2a
	5683	1000	5983	4770 x 3	.04	14	1.02	2a
	5684	1500	5984	5220 x 3	.14	10	1.04	2a
7 (31.6, 55.1) 5595	5845	4000	5985	5664 x 2		4.5	1.04	3
	5671	600	5801	4032 x 2	.09	10	.99	2a
	5673	1000	5803	5152 x 3	.09	13	1.02	2a
	5804	1500	6126	5856 x 3	.1	11	1.07	2a
	5675	4000	5805	5152 x 3	.1	9.5	1.06	3
8 (37.5, 55) 5334	5641	600	5771	5170 x 2	.08	12.5	.99	2a
	5643	1000	5773	5152 x 3	.19	9	1.04	2a
	5644	1500	5774	"	.13	10	.96	2a
	5645	4000	5775	"	.15	7.5	1.04	3
9 (38.5, 54.9) 5340	5761	4000	6051	6384 x 2	.05	9.5	1.05	2c
	5751	4000	6041	6432 x 2	.08	9	1.04	2c
10 (39.5, 55) 5266	5611	4000	6031	5152 x 3	.05	11	1.00	2c
	5173	4000	6021	6552 x 1	.08	15	1.01	2c
11 (40.5, 55.1) 5173	5611	4000	6031	5152 x 3	.05	11	1.00	2c
	5173	4000	6021	6552 x 1	.08	15	1.01	2c
12 (41.5, 55) 4772	5611	4000	6031	5152 x 3	.05	11	1.00	2c
	5173	4000	6021	6552 x 1	.08	15	1.01	2c

Table 2.2

As Table 2.1 Except For Records Other Than the Polymode Array II.

Station # (latitude, longitude) water depth	Experiment	Record ID	Instrument		$\Delta\omega/f$	PH(db)	$\omega/p/f$	Class
			Depth	Data Length				
542 (28, 69.7) 5462	PMI	5421	500	6500	.1	14	1.01	2a
		5424	1500	5000	.1	11.5	1.04	2a
		5427	4000	"	.09	9.5	1.07	3
543 (28, 65) 5363	"	5431	500	6496	.06	15	.96	2a
		5435	4000	5700	.05	12	.97	2b
545 (27.8, 55.6) 6015	"	5451	500	6720	.11	12.5	1.07	2a
		5453	1000	"	.1	11	.99	2a
		5454	2000	"	.06	12.5	1.02	2a
		5456	4000	5616	.09	11	1.03	2b
546 (27.9, 54.9) 5773	"	5461	500	6720	.1	12.5	.99	2a
		5463	1000	"	.09	12.5	1.02	2a
		5465	2000	"	.1	13.5	1.04	2a
		5467	4000	5616	.13	12	.96	2b
547 (28.2, 54.9) 5785	"	5471	500	6720	.06	14	1.03	2a
		5473	1000	"	.09	12.5	1.00	2a
		5475	4000	5616	.05	12	.98	2b
548 (31, 60) 5550	PMI	5481	500	6664	.09	11	.98	2a
		5485	2000	6600	.07	15	.98	2a
		5486	4000	5160	.1	12	1.01	2b
549 (34, 60) 4687	"	5491	500	6400	.07	11.5	1.03	2a
		5494	2000	5670	.08	12	1.08	2a
		5495	4000	6400	.07	11	1.08	2b

Table 2.2 (cont'd.)

<u>Station #</u> (latitude, longitude) <u>water depth</u>	<u>Experiment</u>	<u>Record ID</u>	<u>Instrument</u> <u>Depth</u>	<u>Date</u> <u>Length</u>	<u><math>\Delta\omega/f</math></u>	<u>PH(db)</u>	<u><math>\omega_p/f</math></u>	<u>Class</u>
520 (33.5, 62.6) 4400	Muir Smt.	5202	3023	3182	.21	7.5	1.01	3
623 (27.4, 41.1) 4307	PMIII B	6231 6234 6237	128 1426 3927	8160 " "	.2 .06 .11	10 18.5 11	1.03 1.00 1.06	2a 1 2b
624 (27.3, 40.8) 4372	"	6242 6243 6245	529 1528 4028	" " 4150	.09 .06 .2	15 19 9.5	1.00 1.00 1.12	2a 1 2b
625 (27.2, 40.4) 4723	PMIII B	6251 6253 6255	189 1488 3990	8160 " "	.21 .09 .11	9 17.5 13	1.12 1.02 1.02	2a 1 2b
626 (26.9, 41.2)	"	6263 6265	1514 4014	" "	.1 .08	18 10	1.03 1.1	1 2b
627 (26.2, 41.7) 3857	"	6271 6273	206 1505	" "	.12 .2	8.5 15	1.03 1.03	2a 1
628 (27.4, 47.8) 4961	PMIII A	6283	1489	7920	.1	17	1.05	1
629 (28, 48.1) 4954	"	6291 6293 6295	203 1500 4006	" " "	.18 .08 .05	10 20 16	1.04 1.01 1.04	2a 1 2b

Table 2.2 (cont'd.)

<u>Station #</u> (latitude, longitude) <u>water depth</u>	<u>Experiment</u>	<u>Record ID</u>	<u>Instrument</u> <u>Depth</u>	<u>Data Length</u>	<u><math>\Delta\omega/f</math></u>	<u>PH(db)</u>	<u><math>\omega_p/f</math></u>	<u>Class</u>
630 (27.9, 48.7)	PMIII A	6301 6304	200 1498	7920 "	.09 .1	13 17.5	.99 .99	2a 1
631 (27.9, 48.9)	"	6311 6315	212 4016	" "	.05 .14	14.5 14	1.02 .99	2a 2b
632 (26.9, 49.2)	"	6321 6323 6325	190 1488 3993	" 3936 7920	.15 .1 .05	11.5 18.5 15.5	1.03 1.00 .99	2a 1 2b
79 (16.7, 54.3)	PMIII C	7901 7903 7904 7908	194 338 538 4038	8400 " " "	.1 .16 .21 .27	10.5 10.5 7.5 7.0	1.03 1.01 1.06 1.15	2a 2a 2a 2b
80 (15.4, 53.9)	"	8003 8004 8008	319 520 4020	" " "	.16 .11 .19	9.5 9.5 9.5	1.04 1.06 1.13	2a 2a 2b
81 (15.2, 53.2)	PMIII C	8101 8104 8107 8108	160 510 2508 4008	8400 " " "	.11 .13 .19 .15	9.5 9.5 9.5 10.0	1.01 1.09 1.00 1.04	2a 2a 2b 2b
82 (15, 54.2)	"	8201 8203 8204 8207 8208	172 322 522 2446 3946	" " " " "	.1 .15 .26 .19 .24	10.0 9.5 6.5 9.0 10.0	1.00 1.02 1.03 1.08 1.13	2a 2a 2a 2b 2b

Up to three consecutive segments of data have been collected ( $\sim 27$  months) at some sites of the PMII. In order to avoid contamination from low frequency motions, each segment of data was first tapered to zero at both ends and then Fourier transformed. The tapering data window is

$$w_t = 0.5 - 0.5 \cos(10\pi t/T) \quad \text{for } 0 \leq t \leq 0.1 T$$

$$\text{and } 0.9 T \leq t \leq T, \quad (2.1)$$

$$w_t = 1 \quad \text{for } 0.1 T \leq t \leq 0.9 T,$$

where  $T$  is the data length. The leakage of power to adjacent bands is less than 10 % (see Hendry, 1975, Appendix A). Compromising between resolution and stability, the spectral estimates were obtained by averaging the resulting periodogram over several adjacent frequency bands. Near the inertial frequency  $f$ , the resulting resolution is about 0.0012 cph, which is, for instance, 2.4 % of  $f$  at  $36^\circ$ . For those stations with more than one segment of data, the spectrum of each segment was then ensemble averaged to obtain more degrees of freedom. The least degrees of freedom is 14.

### 2.3 The observed spectra

For a typical record in the main thermocline (600 m at Station 5), the two cartesian components of horizontal kinetic energy spectrum are displayed in Fig. 2.2. Because these two spectra generally cannot be distinguished in the whole internal wave band, either one can be used to represent the horizontal kinetic energy spectrum  $F_H(\omega)$ . For frequencies remote from the inertial, tidal, and buoyancy frequencies,  $F_H(\omega)$  can be well described by a power law of the following form :

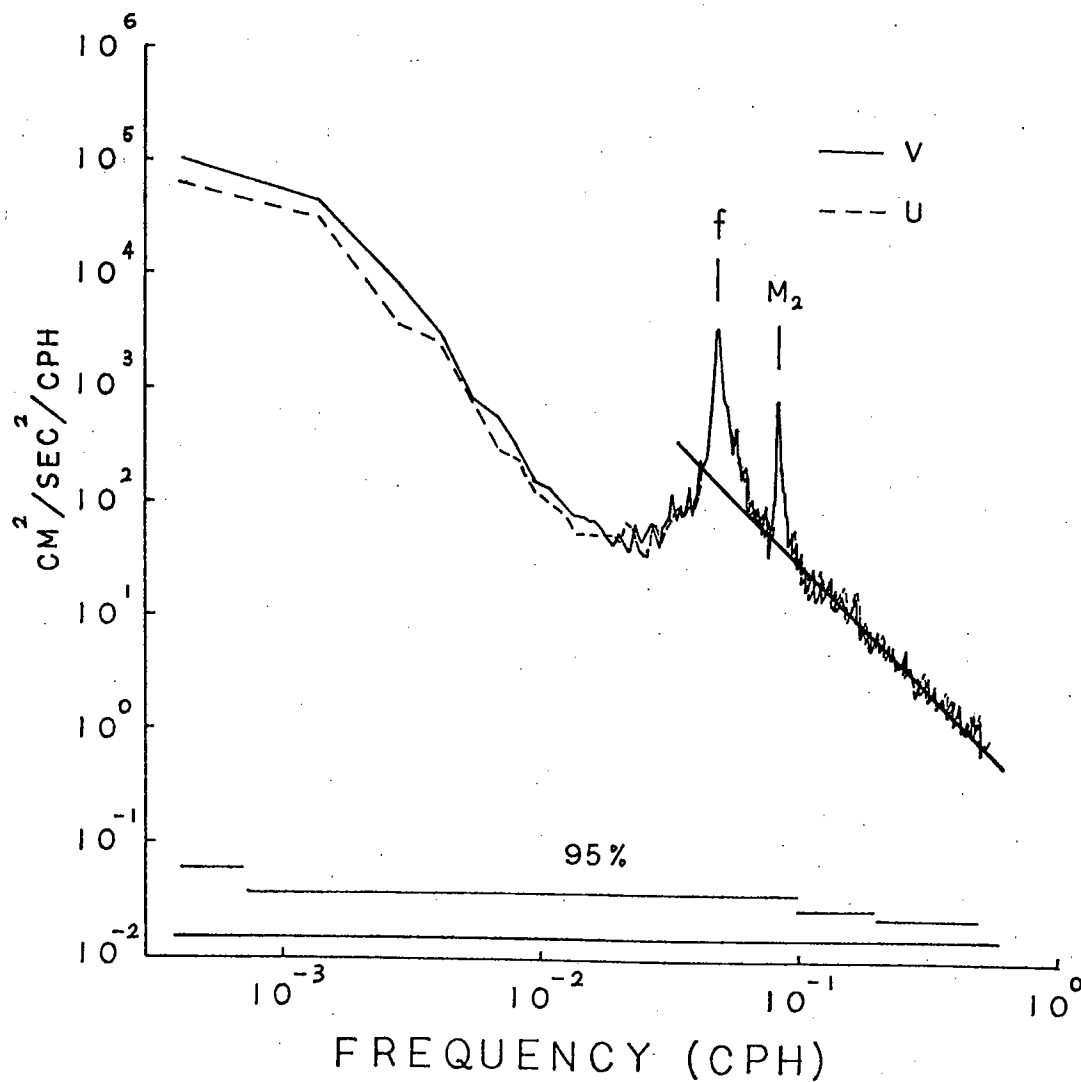


Figure 2.2 Spectra of u and v components at 600 m at Station 5 of the PMII. CPH represents cycle per hour. The straight line represents the power law  $E_0 N \omega^{-p}$  with  $N = 2.27$  cph,  $E_0 = 0.096 \text{ cm}^2/\text{sec}^2/\text{cph}^2$ , and  $p = 2.23$ . Shown on the bottom are the 95% confidence intervals.

$$F_H(\omega) = N(z) E_0 (\omega/\omega_0)^{-p}, \quad (2.2)$$

where  $N(z)$  is the buoyancy frequency in cph at depth  $z$ ,  $E_0$  a constant in  $\text{cm}^2/\text{sec}^2/\text{cph}^2$ ,  $\omega$  a frequency in cph,  $\omega_0 = 1$  cph, and  $p$  a dimensionless constant. Presumably the constants  $E_0$  and  $p$  are independent of  $z$ , because in this frequency regime  $F_H(\omega)$  should be proportional to  $N(z)$  as consistent with the WKBJ scaling. As  $\omega$  approaches  $f$ , the spectral level begins to rise above that given by (2.2) and forms a prominent peak near  $f$  -- the so-called inertial peak. Because the essential characteristics of a spectral peak are its energy level, frequency  $\omega_p$ , and bandwidth  $\Delta\omega$ , we have tabulated these three parameters for each record in Tables 2.1 and 2.2. The bandwidth is defined as the difference between the frequencies where the power falls to one half of its peak value. The tabulated values of both  $\omega_p$  and  $\Delta\omega$  are in units of  $f$ . The energy level of the peak is expressed in terms of its ratio to the value given by (2.2) with  $\omega$  equal to the peak frequency, and the logarithm of this ratio is defined as the "peak height", denoted by PH in decibels (db hereafter, defined as  $10 \times \log_{10}$ ). For the spectrum shown in Fig. 2.2,  $\Delta\omega = .05 f$ ,  $\omega_p = f$ , and PH = 13.5 db (with  $E_0 = .096$ ,  $p = 2.23$ ).

In order to determine the peak height in a precise way, we first need a standard procedure to determine the constants  $E_0$  and  $p$  in (2.2). For the universal spectrum proposed by Garrett and Munk (1972),  $E_0 \approx 0.13$ , and  $p \approx 2$ . Because significant deviations from the universal spectrum have been documented by Wunsch (1976) and Wunsch and Webb (1979), we will not use the universal values but apply a



least-squares to fit the observed spectra to (2.2) between 0.1 cph and 0.8 N(z) for each record, with  $E_0$  and  $p$  as parameters to be found. All the tabulated values of PH were estimated based on  $E_0$  and  $p$  obtained through this procedure. As expected, the values of  $E_0$  and  $p$  do not vary much over most of the records, but we have found some anomalous records. For selected stations which are representative of nearby ones, if any, within 200 km, the values of  $E_0$  and  $p$  are listed in Table 2.3 together with those of  $E_{H5}'$ , which is the value of  $F_H(\omega)/N(z)$  calculated at the frequency corresponding to a 5-hour period (for GM spectrum,  $E_{H5}' \approx 3.3$ ). Note that  $E_{H5}'$  is different from  $E_5'$  tabulated by Wunsch (1976); this latter is the normalized total energy at 5-hour period.

The anomalous records are those of the PMIII clusters A and B, where the values of  $E_0$  and  $p$  at nominal depths 1500 m and 4000 m are significantly different from the others --  $E_0$  is higher and  $p$  is lower. The values of  $E_{H5}'$  are also higher here, but by less than an order of magnitude; together with the small values of  $p$ , the higher values of  $E_{H5}'$  imply that internal wave energy at periods shorter than 5 hours is significantly higher in these records than the others, up to an order of magnitude. The WKBJ scaling does not work here at all (see Fig. 2.3c), but it works so well at other stations that the values at one depth are representative of the whole water column (away from the upper and lower boundaries though). The reason for the breakdown of WKBJ scaling here is unclear; however, it is very likely associated with the proximity to the Mid-Atlantic Ridge (about 300 km from either cluster) and the very rough underlying topography.

Table 2.3

Tabulation of Estimated Buoyancy Frequency  $N$ , Parameters  $E_0$  and  $p$  in Eq. (2.2) (parenthetical values are standard errors of fit), and the normalized horizontal kinetic energy at 5 h period ( $E_{H5}$ ) for selected records.

Station #	Experiment	Latitude (N), Longitude (W)		Instrument	Depth (m)	$N$ (cph)	$E_0$	$p$	$E_{H5}$
		Latitude (N)	Longitude (W)						
1	PMII	35.9, 55		600		2.16	.14 (.17, .12)	2.13 + .11	4.3
4	"	36, 53.8		600		2.23	.087 (.11, .071)	2.28 + .13	3.4
5	"	34.9, 55		"		2.27	.096 (.12, .078)	2.23 + .14	3.5
6	"	35.9, 59		"		2.34	.084 (.1, .071)	2.13 + .11	2.6
7	"	31.6, 55.1		"		2.3	.061 (.073, .051)	1.97 + .12	1.5
8	"	37.5, 55		"		2.35	.097 (.12, .079)	2.25 + .13	3.6
10	"	39.5, 55		4000		.4	.078 (.11, .057)	2.41 + .18	3.8
12	"	41.5, 55		"		.36	.041 (.064, .027)	2.56 + .25	2.6
542	PMI	28, 69.7		500		2.18	.042 (.05, .035)	2.03 + .11	1.1
543	"	28, 65		500		2.32	.046 (.055, .039)	2.04 + .11	1.2
546	"	27.9, 54.9		"		2.32	.066 (.084, .051)	1.96 + .16	1.6
548	"	31, 60		"		2.1	.047 (.057, .039)	2.2 + .13	1.6
549	"	34, 60		"		2.12	.053 (.066, .043)	2.3 + .14	2.2
6231	PMIII B	27.4, 41.1		128		2.92	.16 (.2, .12)	1.65 + .15	2.2
6234	"	"		1426		.97	1.2 (1.6, .96)	.86 + .16	4.9
6237	"	"		3927		.22	1.7 (4.2, .66)	1.05 + .5	9.0
6291	PMIII A	28, 48.1		203		2.32	.14 (.18, .11)	1.71 + .16	2.2
6293	"	"		1500		.96	.96 (1.2, .75)	.97 + .16	4.6
6295	"	"		4006		.32	.59 (1.25, .28)	1.27 + .41	4.6
82	PMIII C	15, 54.2		522		2.03	.061 (.071, .053)	1.91 + .1	1.3

### 2.3a Variability and classification

The three parameters discussed above can be used as three different indices for the description of the spectral shape near  $f$ , while the corresponding energy level can be inferred with the aid of Table 2.3. A variety of spectral shapes have been reflected in the great variability of these parameters : from 4 db to 20 db for PH; from .03  $f$  to .27  $f$  for  $\Delta\omega$ ; from 0.96  $f$  to 1.15  $f$  for  $\omega_p$  . Hence a universal frequency spectrum near  $f$  is impossible. One of the major tasks of this chapter is to find if there is any correlation between this variability and the physical environment (instrument depth, topography, etc.) in which the measurements were taken. Because the spectral shape is grossly determined by its peak height, we first consider the variability of the peak height.

Normalized spectra of horizontal kinetic energy at three stations which are typical of three different topographic features -- abyssal plain, rough relief, and very rough relief close to the Mid-Atlantic Ridge-- are displayed in Figs. 2.3a, b, and c respectively. In Fig 2.3a the peak height at 4000 m ( $\sim 7$  db) is significantly less than that at upper levels ( $\geq 10$  db), but the high frequency portion of the spectra scale in the WKBJ sense. In Fig. 2.3b spectra at different levels are almost indistinguishable from one another through the whole internal wave band, with peak height about the same as that at upper levels in Fig. 2.3a. Displayed in Fig. 2.3c are the anomalous spectra noted before; the peak height at 1426 m is outstanding as compared to the other two levels where the peak height is about the same as in Fig. 2.3b. The separation of spectral levels at high frequencies is striking here; at

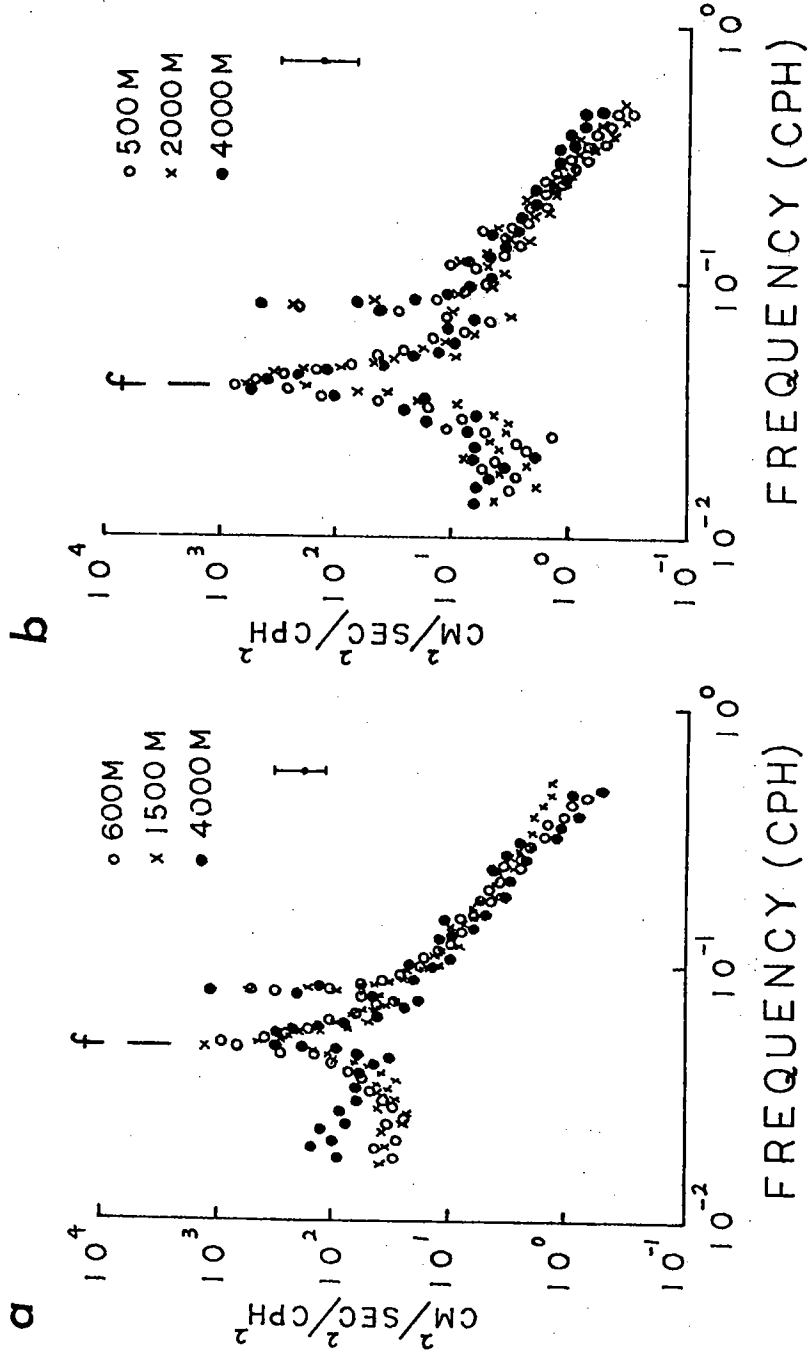


Figure 2.3 Normalized horizontal kinetic energy spectra at (a) Station 3 of the PMII (smooth topography) and (b) Station 546 of the PMI (rough topography). Error bar is 95 % confidence limit.

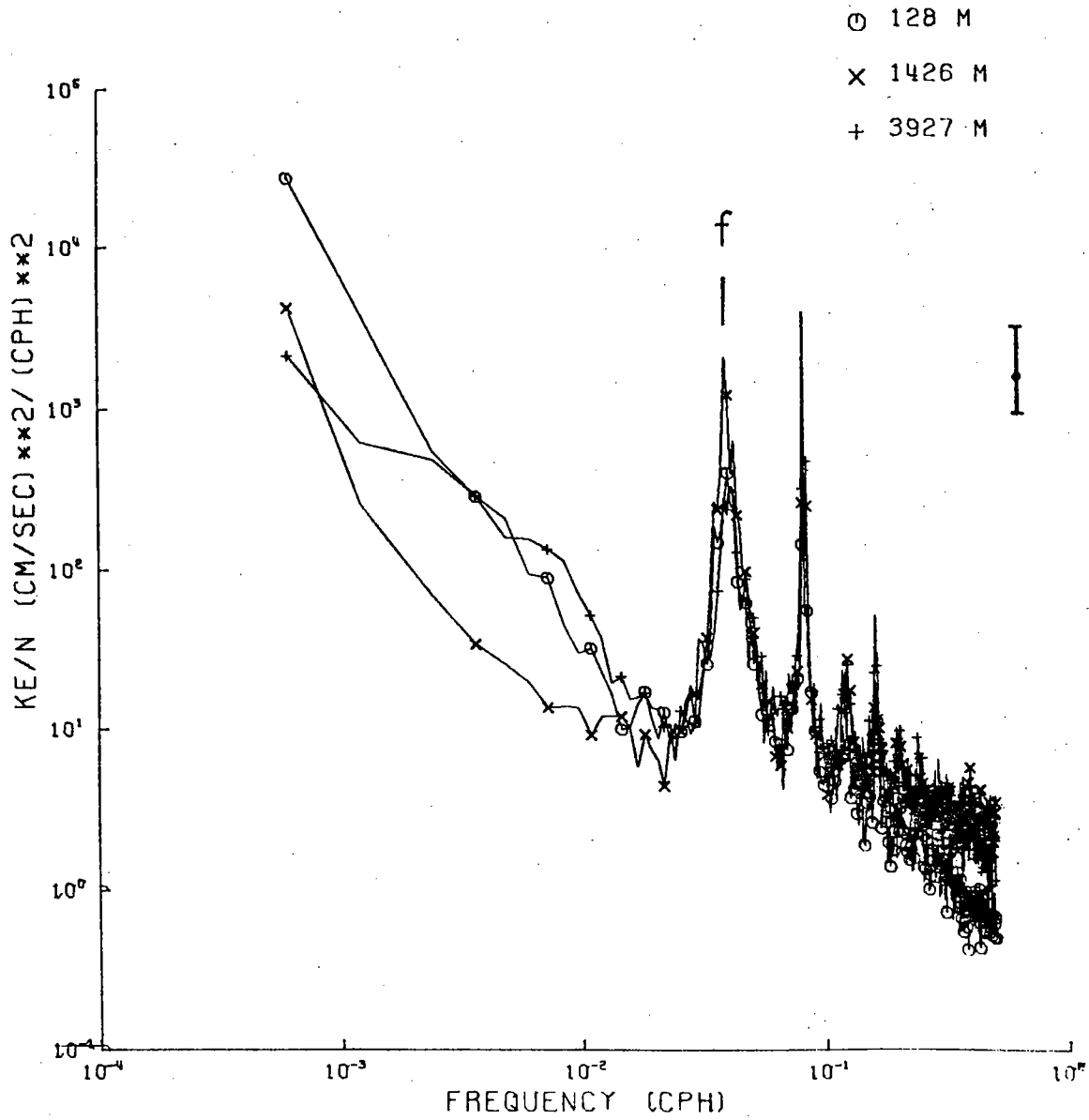


Figure 2.3c As in Fig. 2.3 except at Station 623 of the PMIII cluster B (near the Mid-Atlantic Ridge, very rough topography)

1426 m and 3927 m,  $p \approx 1$  and the normalized high frequency energy is significantly higher than that at 128 m. After further exploration, it was found that the peak height at 4000 m underneath the Gulf Stream (Stations 9, 10, 11, 12) was also about the same as in Fig. 2.3b, although the topography was smooth there. Thus, the different kinds of environment can be roughly grouped into three classes according to their corresponding peak height as follows :

class 1

nominal depth of 1500 m near the Mid-Atlantic Ridge.

average PH : 18 db

class 2

(a) depth less than 2000 m (excluding class 1);

(b) depth greater than 2000 m over rough topography ;

(c) nominal depth of 4000 m underneath the Gulf Stream.

average PH : 11.5 db

class 3

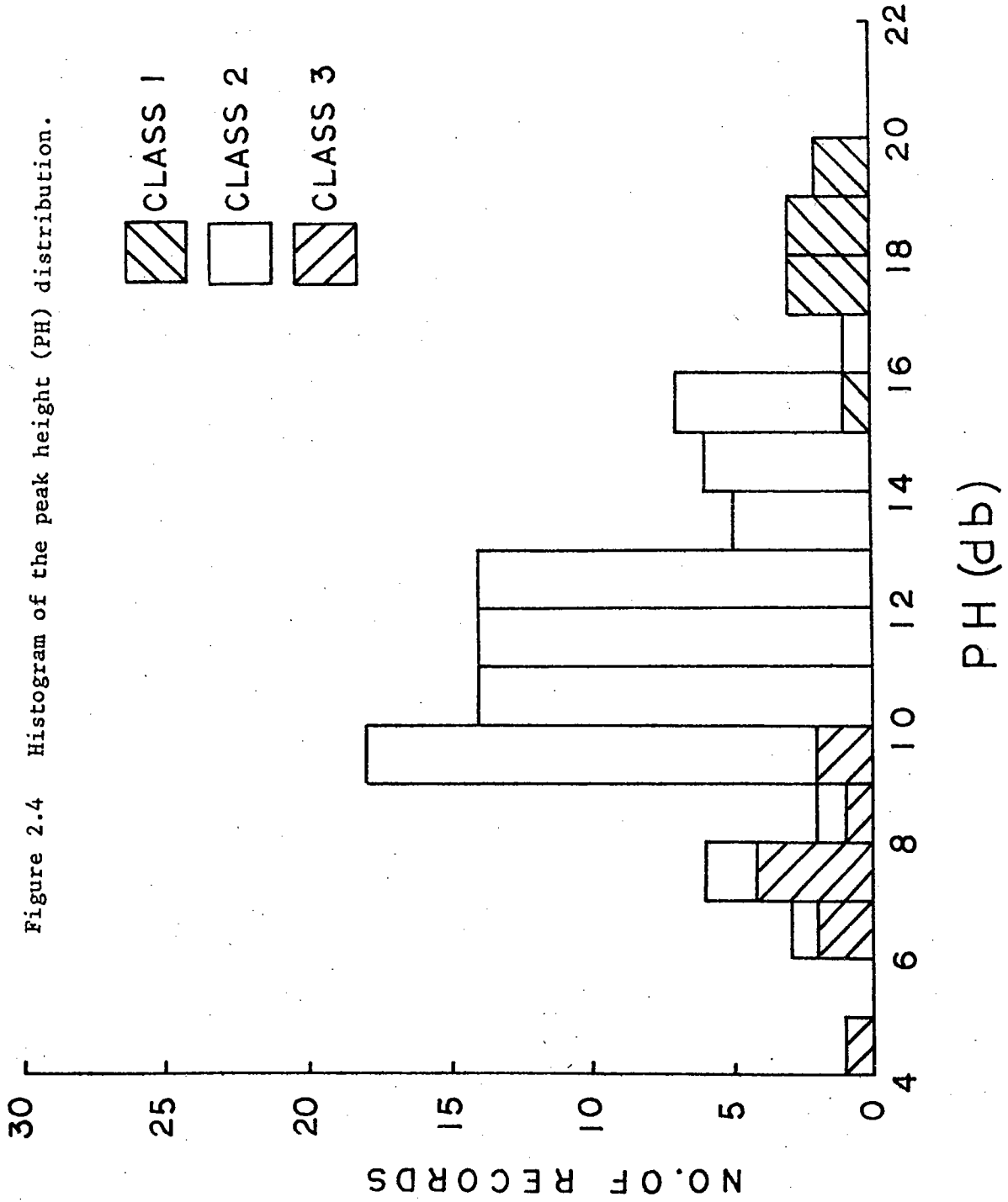
depth greater than 2000 m over smooth topography.

(excluding class 2c)

average PH : 7.5 db

The classification of each record has been noted in Tables 2.1 and 2.2. Displayed in Fig. 2.4 is the histogram of the distribution of peak height of all the records examined, with contributions from different classes properly labeled. The substantial overlap between class 1 and class 2 is basically caused by the ambiguity in identifying the class for some smooth areas which are adjacent (within about 100 km) to rough

Figure 2.4 Histogram of the peak height (PH) distribution.



areas. Due to the propagation of inertial waves, the influence of rough topography can easily spread to nearby areas. Despite some degree of looseness, this scheme of classification does provide a sensible way to describe such a great variability of spectral shape.

The lowest peak height from a class 3 environment is associated with the record at the 4000 m level of Station 6, which is in the midst of the New England Seamount Chain and is partially surrounded by seamounts (about 180° azimuth -- SE, NE, and NW). Normalized kinetic energy spectra of this record are shown in Fig. 2.5. The disappearance of a prominent inertial peak here is a unique feature in the whole data set. It is probably caused by the nearby seamounts (the nearest one is about 50 km away), of which some penetrate to less than 2000 m from the sea surface. However, the record at 3000 m of Station 520 which is only 12 km away from the Muir Seamount, shows a prominent peak of 7.5 db. Therefore the overall influence of seamounts on the spectrum of inertial waves, if any, is not particularly clear.

### 2.3b Frequency shift of the inertial peak

It is well known now that in the deep ocean the inertial peak usually occurs not right at the local  $f$ , but at a frequency slightly above it. Theory suggests that only waves with super-inertial frequencies can propagate downward from the surface layer, which presumably is the major source for deep inertial waves. But does this so-called blue shift occur universally in the deep ocean? Does it vary with depth and geographical environment and consequently with peak height?

The ratios of the peak frequency  $\omega_p$  to  $f$  for all the records are



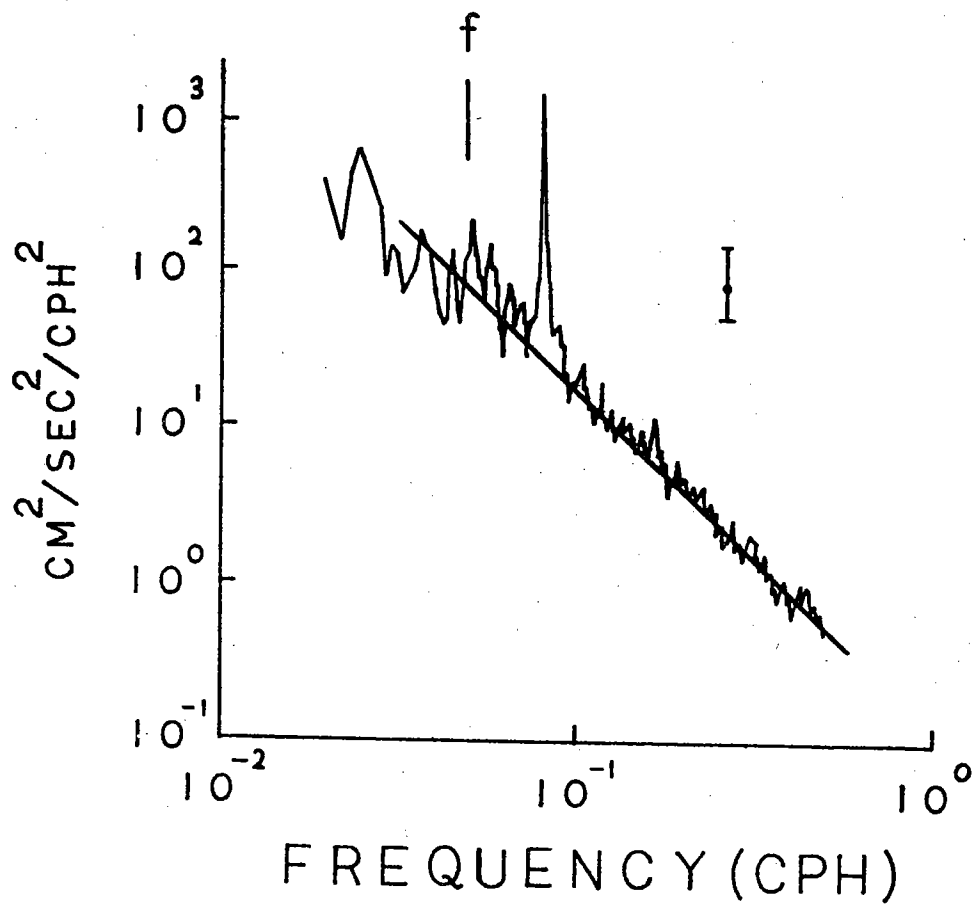


Figure 2.5 Normalized horizontal kinetic energy spectrum at 4000 m, Station 6, PMII. The straight line represents the power law fit. Error bar is 95 % confidence limit.

plotted against depth in Fig. 2.6. The dashed lines represent the limits of the frequency resolution associated with  $\omega_p/f = 1$ , i.e.,  $\omega_p/f$  is significantly different from 1 for those points outside the strip enclosed by the dashed lines. Over smooth topography, it is clear that a significant blue shift occurs at great depths except near the Gulf Stream, where the peak height is greater. The results over rough topography are mixed; a clear blue shift with depth only occurs at the PMIII cluster C, where the topography is not particularly rough and the corresponding peak height is on the lower side of the class 2 distribution (see Table 2.1). Thus there seems to be some correlation between the blue shift and peak height. In Fig. 2.7  $\omega_p/f$  is plotted against peak height for all the 4000 m records except Station 6 where there is no peak. The blue shift is apparently associated with records having lower peak height, which are primarily from the class 3 environment. This result is consistent with the notion that inertial waves in the class 3 environment are free waves coming from elsewhere, whereas those in the class 1 and class 2 are strongly influenced by local sources.

### 2.3c Bandwidth

The inverse of the bandwidth in a frequency spectrum is a measure of the persistence time scale of a quasi-periodic motion. For instance, if  $\Delta\omega/f = 0.1$ , then the persistence time scale of inertial waves is about ten inertial periods. From Tables 2.1 and 2.2  $\Delta\omega/f$  has no specific relations with PH but has some weak, if not definite, correlation with latitude. Listed in Table 2.4 is the ensemble average

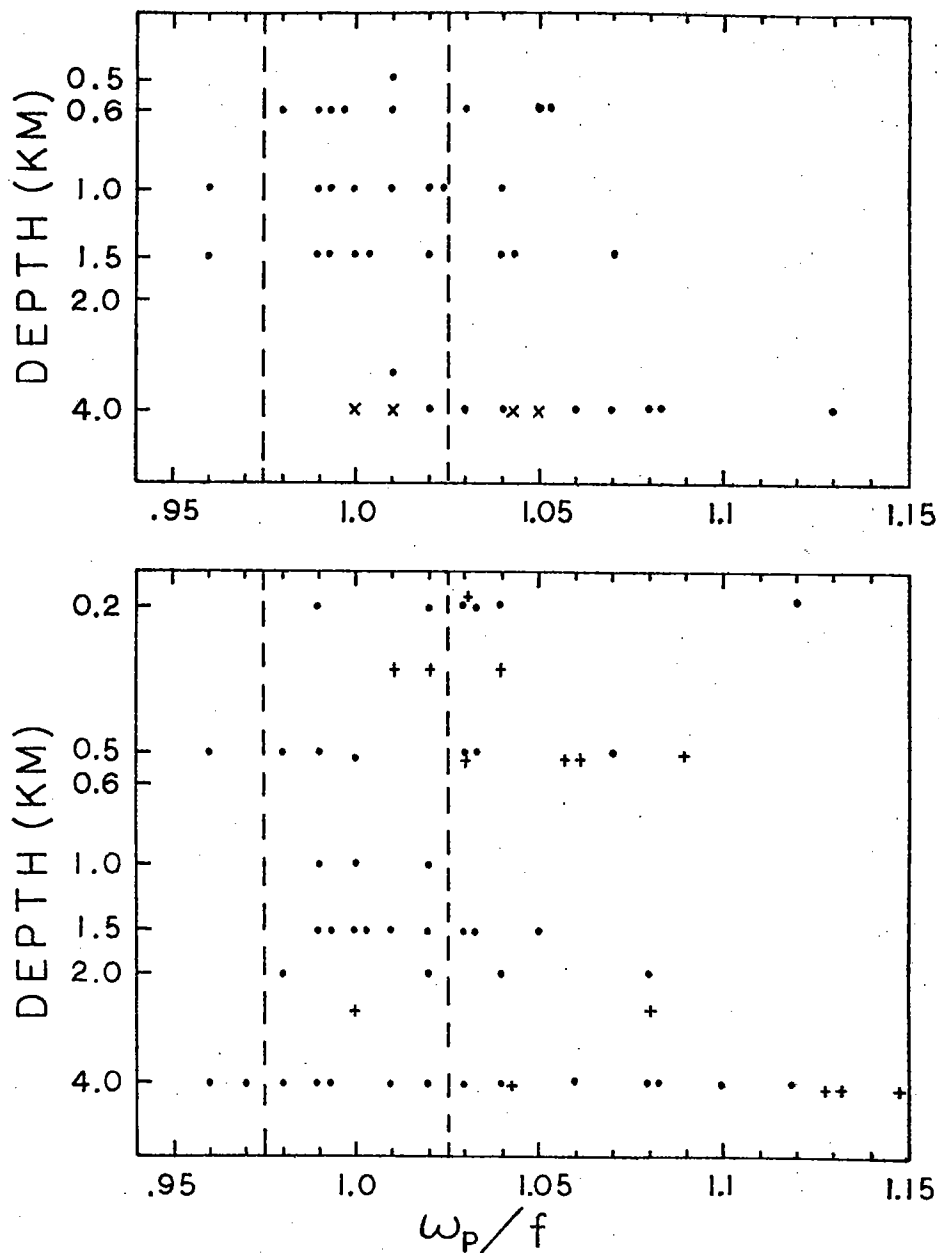


Figure 2.6 Ratio of the peak frequency  $\omega_p$  to  $f$  against instrument depth. Upper panel is for smooth topography areas; lower panel is for rough topography areas. Special symbols: x -- measurements underneath the Gulf Stream; + -- PMIII C. Dashed lines represent the frequency resolution limits associated with  $\omega_p/f = 1$ .

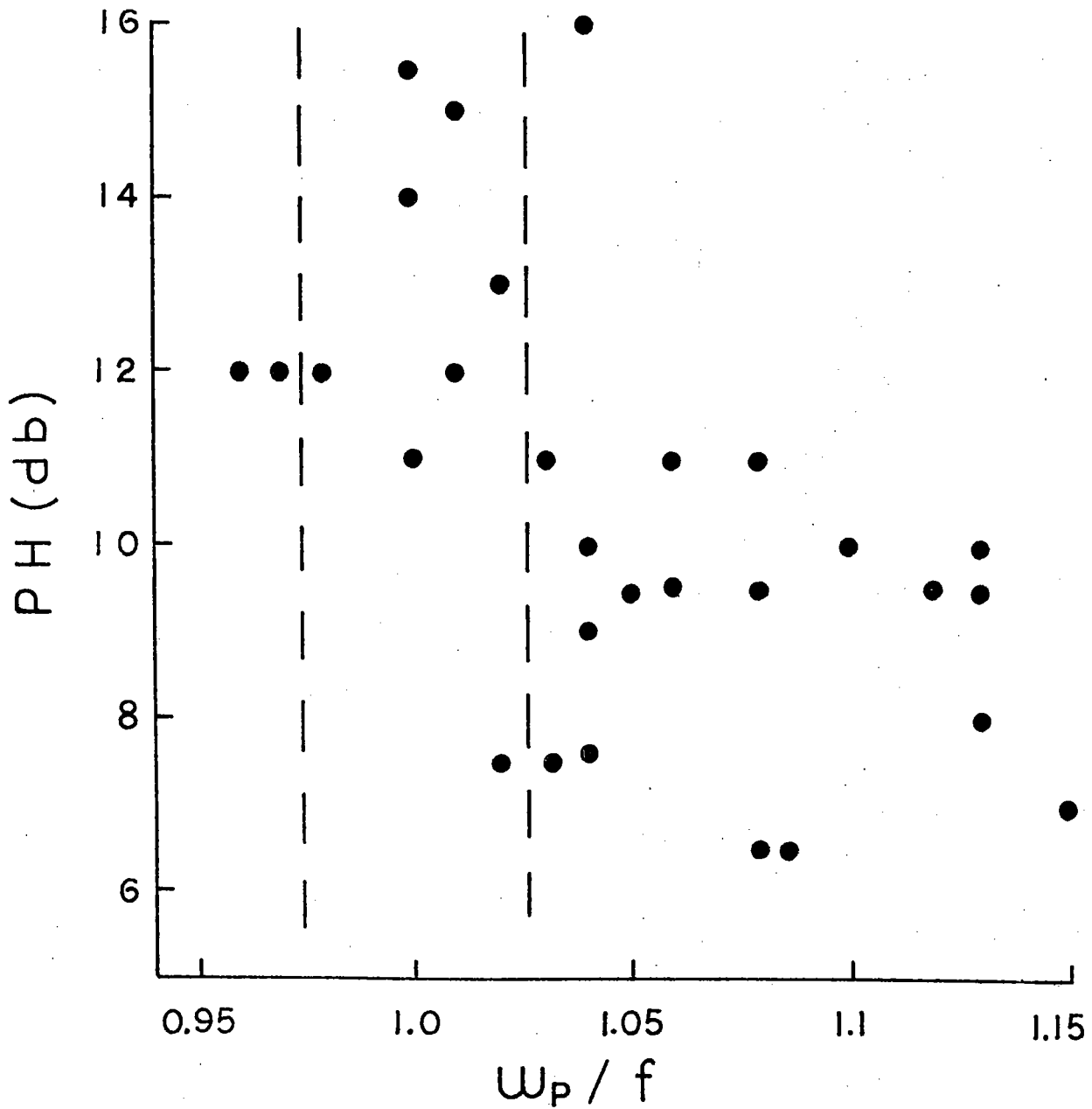


Figure 2.7  $\omega_p / f$  against peak height (PH) at 4000 m. Dashed lines are the same as in Fig. 2.6.

of  $\Delta\omega/f$  within given latitudinal belt. The value at subtropical latitudes ( $15^\circ - 20^\circ$ ) is significantly greater than those at mid-latitudes. This result is consistent with the model to be described in chapter 4.

Table 2.4

Average bandwidth (in percentage of  $f$ ) at various latitudes.

Errors are standard deviations.

<u>latitude</u>	<u>average bandwidth</u>
15°-20°	.17 ± .055
25°-30°	.1 ± .044
30°-35°	.095 ± .036
35°-42°	.097 ± .047

### 2.3d Rotary spectrum

In addition to cartesian components, horizontal kinetic energy also can be decomposed into its rotary components. These have proven useful in separating inertial wave energy from other current components (Gonella, 1972; Mooers, 1973). For the same record shown in Fig. 2.2, the spectra of the two rotary components are shown in Fig. 2.8. The rotational nature of inertial waves is clearly demonstrated by the dominance of the clockwise component spectrum  $E_-(\omega)$  over the counter-clockwise component spectrum  $E_+(\omega)$ . This dominance begins at sub-inertial frequencies, reaches its maximum near  $f$ , and continues through the whole internal wave band; on the other hand,  $E_+(\omega)$

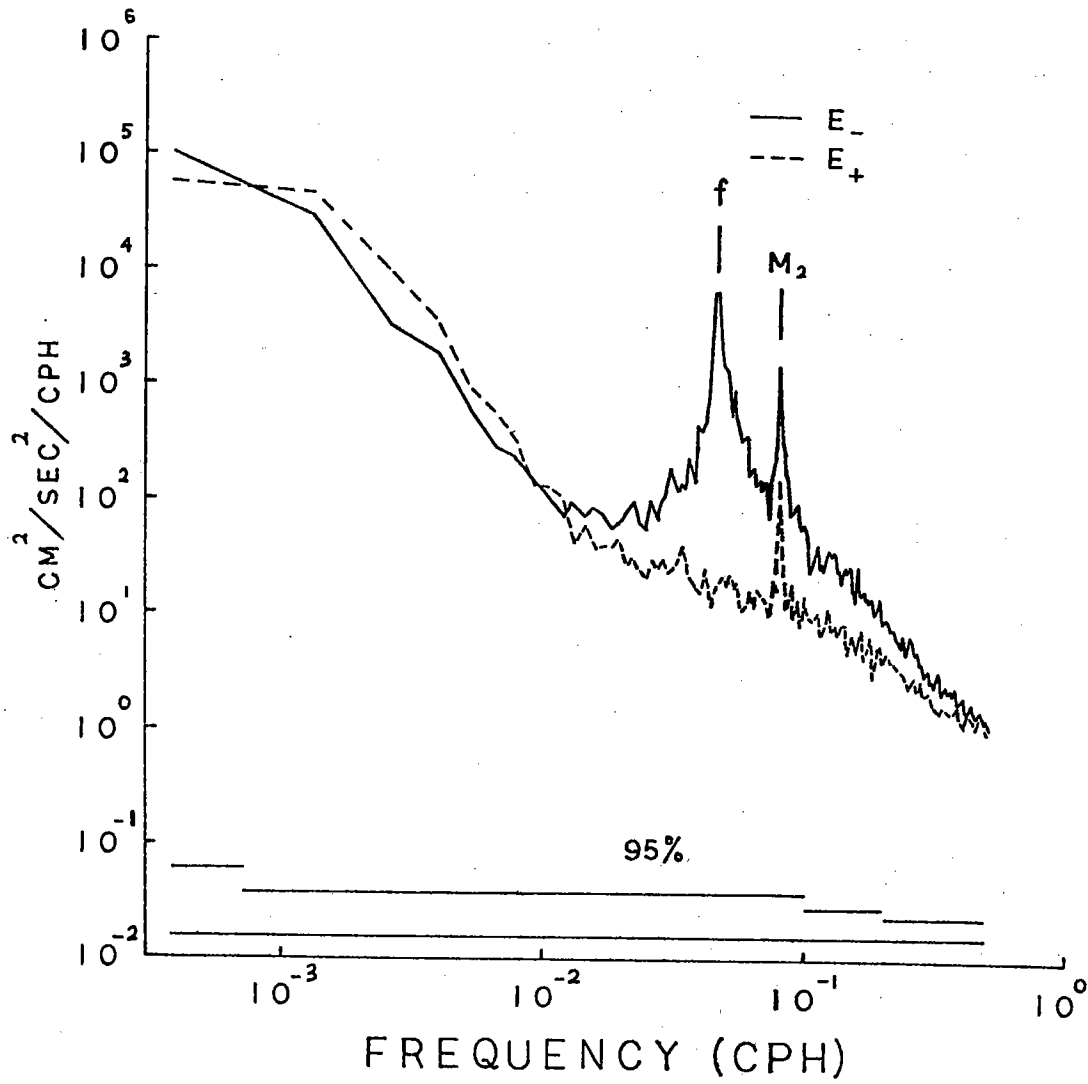


Figure 2.8 Rotary spectra of the same record as in Fig. 2.2.  
 $E_-$  — clockwise component;  $E_+$  — counter-clockwise component.

decreases monotonously and smoothly with frequency. This behavior is typical of all the records and basically consistent with the linear internal wave theory which predicts

$$\frac{E_-(\omega)}{E_+(\omega)} = \left( \frac{\omega + f}{\omega - f} \right)^2 \quad (2.3)$$

Because (2.3) was derived from an  $f$ -plane model, the infinite ratio at  $\omega = f$  is spurious (see Chapter 4). The cause of the dominance of clockwise energy at sub-inertial frequencies (as low as  $0.4 f$  in Fig. 2.8) is unclear. It may be due to nonlinear interactions between inertial waves and low frequency motions. Otherwise, spectra in this frequency regime presumably is determined by the process of geostrophic turbulence (Charney, 1971), and the coherence between  $u$  and  $v$  should be zero and hence no clockwise dominance. Because the turbulent cascading would allow certain amount of energy to be transferred from low to high frequencies, until  $f$  is reached, inertial waves would be resonantly forced by energy in the clockwise component; however, energy in the counter-clockwise component would continue cascading to higher frequencies and account for part of the observed finite amount of counter-clockwise energy and its smooth spectrum. By this mechanism, low frequency eddies could be potential local sources for inertial waves. However, a model is needed to verify this speculation.

The most important feature of the rotary spectrum near  $f$  is the large ratio of  $E_-(f)$  to  $E_+(f)$ . So it is desirable to use the logarithm of this ratio, denoted by  $\Gamma$ , as an index for the description of the rotary spectrum near  $f$ . For instance,  $\Gamma$  is 25 db in

Fig. 2.8. As  $E_+(\omega)$  decreases smoothly and monotonously with  $\omega$ , its shape does not vary much from record to record. Thus  $\Gamma$  should be roughly proportional to PH and should have the same variability. In Fig. 2.9  $\Gamma$  is plotted against PH for all the records except those of the PMIII clusters A and B, which exhibit the same behavior as the other records near  $28^\circ\text{N}$  and hence are omitted. A roughly linear correlation between  $\Gamma$  and PH is visible. The systematically low values of  $\Gamma$  near  $28^\circ\text{N}$  are probably caused by the closeness of  $f$  to the diurnal tidal frequencies; because tides are forced motions, they could have an appreciable amount of counter-clockwise energy.

#### 2.4 Coherences

The calculation of spatial coherence at a particular frequency  $\omega$  usually yields two kinds of information: from the coherence scale,  $\Delta x$ , defined as the separation distance at which the coherence drops to one half, one can estimate the wavenumber bandwidth,  $\Delta k$ , of the underlying process at  $\omega$  as  $\Delta k = 4/\Delta x$  (c.f. MP, eq.(59)); from the phase difference and separation distance, one can estimate the dominant wavenumber at  $\omega$ .

##### 2.4a Horizontal separation

There have been few convincing estimates of the horizontal coherence scale for inertial waves in the open ocean. The horizontal spacings of array measurements have usually been either too small ( $\lesssim 0(1 \text{ km})$ , e.g., Webster, 1968; Schott, 1970; Briscoe, 1975) or too large. The only conclusion which can be drawn from previous investigations is that the horizontal coherence scale is at least several kilometers. However, the



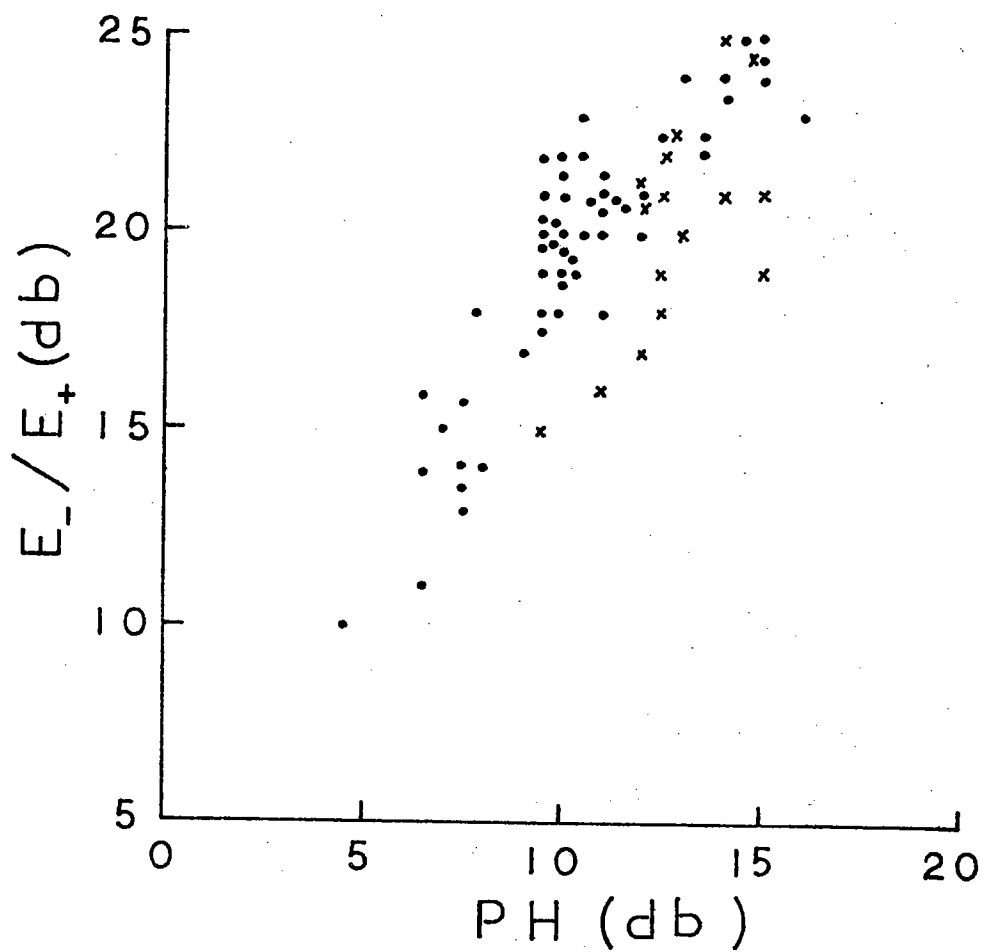


Figure 2.9  $E_-/E_+$  against peak height (PH). " x " represents the stations roughly along 28°N.

theory of MP suggests that the coherence scale is of the order of tens of kilometers. There are five clusters of moorings of this size in the Polymode arrays (see Fig. 2.2) : the central cluster of PMII ( $36^{\circ}\text{N}$ ,  $55^{\circ}\text{W}$ ), the eastern cluster of PMI ( $28^{\circ}\text{N}$ ,  $55^{\circ}\text{W}$ ), the clusters A, B, and C of PMIII. It is possible now to test the theory of MP using the coherences estimated from these clusters. Because the major concerns are inertial waves, all the coherences discussed below are between the clockwise components of horizontal velocity.

Fig. 2.10 shows the coherence and phase at 600 m between Stations 1 and 2 of the PMII; these moorings are 30 km apart in the zonal direction. Within a narrow band centered at the local  $f$ , the high coherence and small phase are quite conspicuous. For each of the five clusters mentioned above, the coherences in the inertial frequency band have been calculated between selected stations and plotted against horizontal separation in Fig. 2.11. Each point represents the highest coherence estimated in three adjacent frequencies of which the central one is the local  $f$ . The coherence is the result of averaging over eleven frequencies, so the level of no significance at 95 % confidence is about 0.51. In the upper ocean the coherence drops with increasing separation, yielding a coherence scale of approximately 60 km, which is not inconsistent with the prediction of MP. So the estimated bandwidth is  $1/15$  radians/km. In the deep ocean the coherence does not vary so systematically with separation, and the coherence scale seems to be less than that in the upper ocean (some high values with large separations are probably not significant).

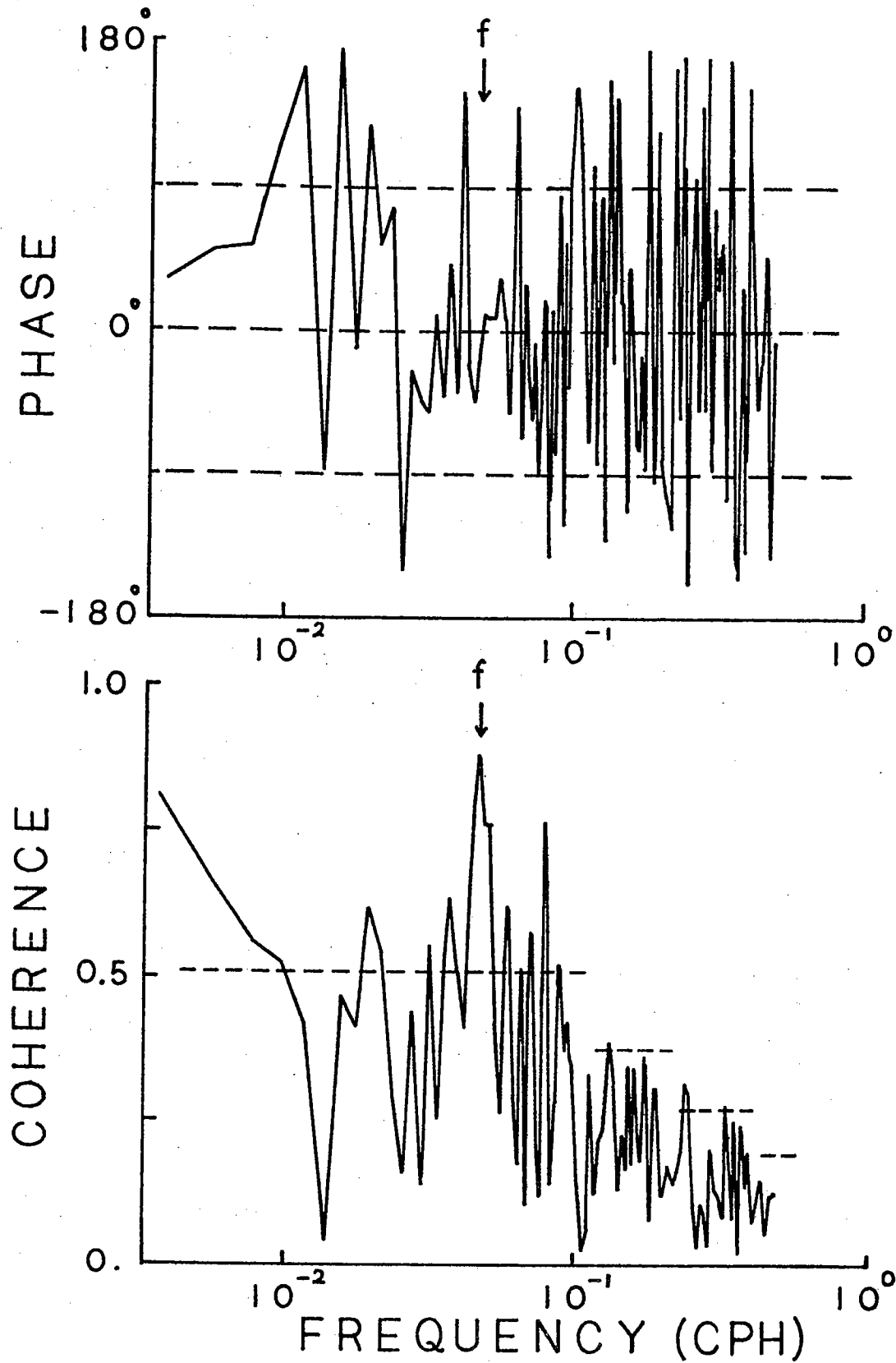


Figure 2.10 Clockwise component coherence and phase between Stations 1 and 2 of the PMII at 600 m. Arrows represent the location of  $f$ . Dashed lines in the coherence plot are the 95 % confidence levels of no significance.

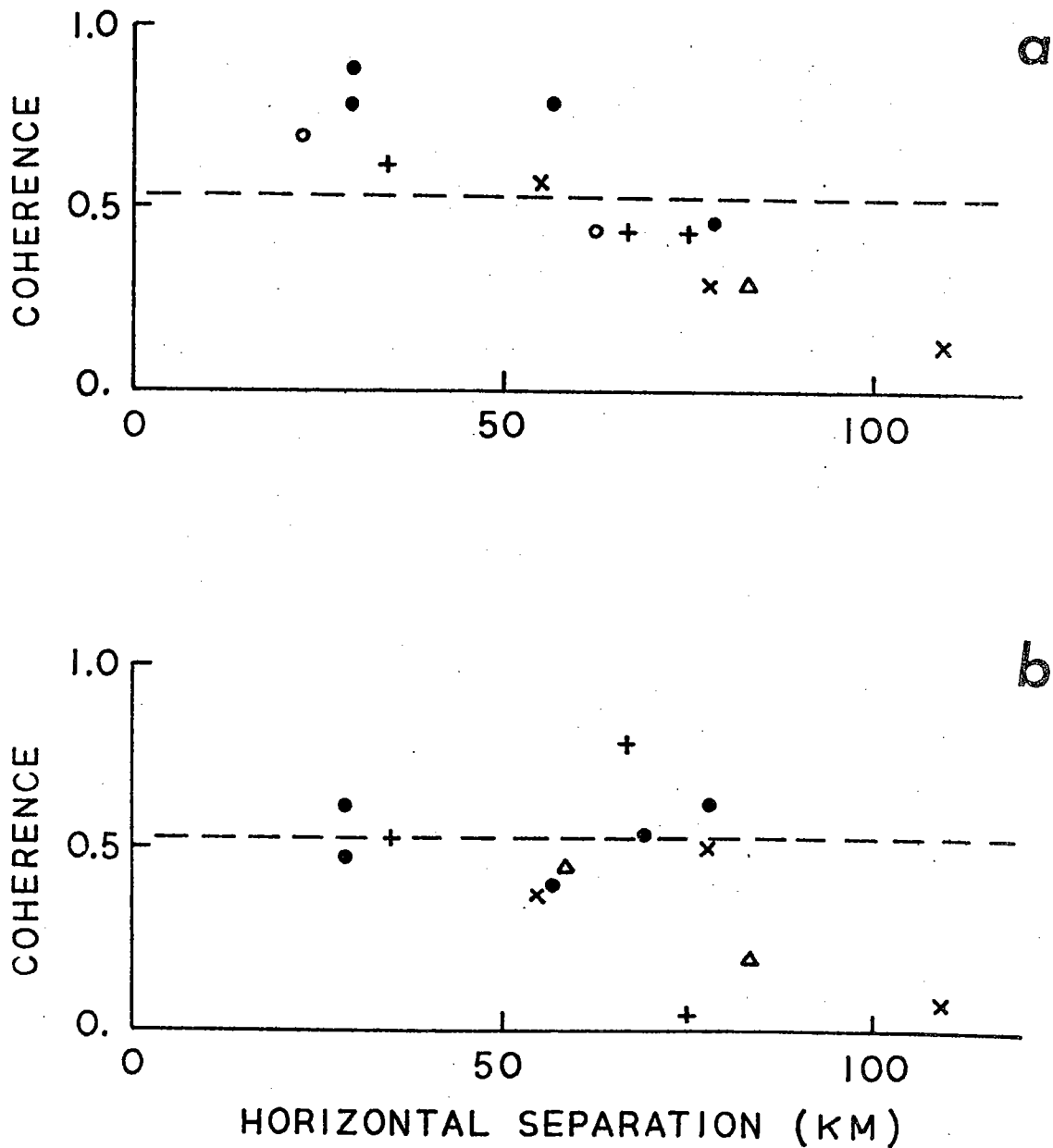


Figure 2.11 Clockwise component coherence against horizontal separation : (a) at upper levels from 200 m to 600 m; (b) at 4000 m. Special symbols : + -- PMI ; • -- PMII ; o -- PMIII A ; Δ -- PMIII B ; x -- PMIII C. Dashed lines are the 95 % confidence levels of no significance.

The estimates of coherence and phase difference at different depths for the three closest stations of the central cluster of PMII are listed in Table 2.5. Horizontal wavenumber spectra have been calculated at each frequency using these coherence and phase estimates (for the method, see Wunsch and Hendry, 1972). Due to inadequate array size, the results do not yield any dominant wavenumbers which are significantly different from zero and its aliased values. However, recent profiler observations suggest a horizontal wavelength of the order of 60 km (Sanford, 1979; personal communication).

#### 2.4b Vertical separation

There have been more reports of the vertical coherence of inertial waves than of the horizontal one. For example, Webster (1968) reported a low coherence of 0.3 over 80 meters vertical separation in the upper 100 meters at Site D; Perkins (1970) reported significant coherences even over 1500 meters separation below the mixed layer in the Mediterranean; Fomin and Savin (1973) reported that above the main thermocline in the Black Sea, the coherence decreased rapidly over a distance from 20 to 30 meters, and that below the thermocline, it decreased relatively slowly with alternating maxima and minima. However, it is generally believed that below the mixed layer in the open ocean, the vertical coherence scale of inertial waves is  $O(70-140m)$  (Müller et al, 1978). The large values found in the Mediterranean are probably caused by the atypical dominance of low modes; indeed, Perkins (1970) showed that the vertical structure of inertial waves in the Mediterranean could be well described by the third vertical mode.

Table 2.5

Tabulation of Clockwise Component Coherence Between Horizontally Separated Instruments at Three Period Bands of Which the Central One is the Inertial Period. Parenthetical Values are Phase Differences in Deg. with 95% Confidence Error Bars.

Station pair (separation in km)	Instrument Depth (m)	Coherence		
		21.51 h	20.61 h	19.78 h
1 - 2 (29)	600	.79 (-45 ± 21)	.88 (-13 ± 15)	.76 (10 ± 24)
	1500	.56 (-49 ± 44)	.88 (2 ± 15)	.76 (10 ± 24)
	4000	.16 (-46)	.62 (2 ± 36)	.48 (18 ± 58)
1 - 3 (29)	600	.51 (42 ± 52)	.6 (37 ± 38)	.78 (-3 ± 22)
	1500	.35 (49)	.72 (31 ± 27)	.39 (-18)
	4000	.44 (-86 ± 72)	.22 (-26)	.48 (-57 ± 58)
2 - 3 (57)	600	.53 (41 ± 48)	.71 (55 ± 28)	.79 (-11 ± 21)
	1500	.69 (143 ± 29)	.73 (41 ± 26)	.3 (-78)
	4000	.4 (92)	.37 (-119)	.19 (-64)

The third mooring at Station 7 (31.6°N, 55°W) was heavily instrumented below the main thermocline: three additional instruments were set at 800 m, 950 m, and 1000 m. Clockwise component coherences at three adjacent frequencies centered at  $f$  for these three instruments and the one at 1500m are listed in Table 2.6. The estimated coherence scale is of the order of 200 meters. The phase estimates differ significantly from zero and do not change much from frequency band 1 to band 2, but drop substantially in band 3; moreover, they are approximately proportional to the separation distance, suggesting a dominant upward phase propagation with "local wavelength" about 450 m in bands 1 and 2 and 1100 m in band 3. It should be noted that for the clockwise component, phase propagation is from the lagging station to the leading one. From the dispersion relation for internal waves (c.f. Phillips, 1977), upward phase propagation implies downward energy propagation. This result is consistent with the findings of Leaman and Sanford (1975).

The coherence scale,  $\Delta z_{1/2}$ , is related to the "equivalent vertical wavenumber bandwidth,"  $\beta_e$ , or its equivalent mode number,  $j_e$ , as follows (c.f. Müller et al, 1978):

$$\Delta z_{1/2} = \frac{2}{\beta_e} = \frac{2bN_0}{j_e \pi N(z)} \quad (2.3)$$

where  $b$  is the scale of the variation of buoyancy frequency and  $N_0$  the buoyancy frequency at the top of the thermocline. Using the values from IWEX profile which is not significantly different from that at Station 7, we have  $bN_0 = 5500 \text{ m.cph}$ ,  $N(900\text{m}) \approx 2.2 \text{ cph}$ . With  $\Delta z_{1/2} = 200\text{m}$ , we obtain  $j_e \approx 8$ , which is closer to  $j_e = 9$  of Cairns and Williams (1976) than  $j_e = 11$  of Garrett and Munk (1975)(c.f. Müller et al, 1978, Table 1).

Table 2.6

As Table 2.5 Except For Vertically Separated Instruments at Station 7 of the PMII.

<u>Instrument Pair</u>	<u>Coherence</u>		
	<u>24.2 h(#1)</u>	<u>23.1 h(#2)</u>	<u>22.2 h(#3)</u>
800m-950m	.68(92 ± 30)	.79(106 ± 21)	.48(57 ± 58)
950m-1000m	.7(77 ± 28)	.82(144 ± 14)	.93(13 ± 11)
800m-1000m	.64(160 ± 34)	.83(162 ± 19)	.43(62 ± 78)
1000m-1500m	.28(20)	.3(130)	.2(-174)



## 2.5 Summary

There is no universal spectrum near  $f$ , but the deep ocean environment in the Western North Atlantic can be roughly divided into three classes according to the height of the inertial peak above the power law which best fits the high frequency portion of the internal wave spectrum (from  $0.1 \text{ cph}$  to  $0.8 \text{ N}$ ): class 1 is the  $1500 \text{ m}$  level near the Mid-Atlantic Ridge, with the greatest peak height of  $18 \text{ db}$ ; class 2 includes (a) the upper ocean (depth less than  $2000 \text{ m}$ ), (b) the deep ocean (depth greater than  $2000 \text{ m}$ ) over rough topography, and (c) the deep ocean underneath the Gulf Stream, with intermediate peak height of  $11.5 \text{ db}$ ; class 3 is the deep ocean over smooth topography, with the lowest peak height of  $7.5 \text{ db}$ .

Substantial blue shift of the inertial peak is basically associated with low values of peak height at great depths. The bandwidth near  $15^\circ\text{N}$  ( $\sim 0.17 f$ ) is greater than that north of  $25^\circ$  ( $\sim 0.1 f$ ).

For horizontal separation, the coherence scale in the inertial frequency band is of the order of  $60 \text{ km}$  at depths from  $200 \text{ m}$  to  $600 \text{ m}$ , and probably less than this value at great depths. The order of magnitude is consistent with the prediction of Munk and Phillips (1968). The wavenumbers estimated from phase differences tend to be indistinguishable from zero. For vertical separation, the coherence scale is of the order of  $200 \text{ m}$  just below the main thermocline and the phase differences suggest an upward phase (downward energy) propagation. The estimated vertical wavenumber bandwidth is in close agreement with the result of Cairns and Williams (1976).

Interpretation of the results summarized above is the central theme

of later chapters, especially the answer to the following question: Can we describe the differences among the three classes of observations in terms of the proposed global and local wave models ?

Chapter 3 Theory of Low Frequency Internal Waves on a Rotating Sphere

3.1 Dynamical equations

An approximation to the dynamics of internal waves is most easily formulated using the equations of motion on an f-plane (e.g., Phillips, 1977), under the assumption that the horizontal wavelengths are so small that the variation of f will not be "felt". This is essentially the WKBJ approximation to the horizontal wave equation. From the dispersion relation

$$\alpha = \frac{m(\omega^2 - f^2)^{1/2}}{(N^2 - \omega^2)^{1/2}}, \quad (3.1)$$

where  $\alpha$  and  $m$  are the horizontal and vertical wavenumbers respectively, we can clearly see the breakdown of the WKBJ approximation when  $\omega = f$ , resulting in an infinite horizontal wavelength. To resolve this problem, we have to resort to the theory of planetary waves which takes the sphericity of the earth into account. In order to obtain a tractable set of equations of motion, the usual assumptions made about the earth's oceans and atmosphere are

- (i) small perturbations relative to a uniformly rotating spherical earth,
- (ii) a uniform gravity field,
- (iii) radial variation of the metrical coefficients is negligible,
- (iv) the depth of the atmosphere and/or ocean is constant and small when compared to the earth's radius,

(v) Boussinesq approximation for the stratification.

The validity of (i)--(iv) was discussed by Miles (1974), and that of (v) was discussed by Spiegel and Veronis (1960). Then the perturbation equations can be written as (c.f. Eckart, 1960)

$$\frac{\partial u}{\partial t} - 2\Omega \sin\phi v - 2\Omega \cos\phi w = -\frac{1}{R \cos\phi} \frac{\partial p}{\partial \lambda} \quad (3.2)$$

$$\frac{\partial v}{\partial t} + 2\Omega \sin\phi u = -\frac{1}{R} \frac{\partial p}{\partial \phi} \quad (3.3)$$

$$\frac{\partial w}{\partial t} + 2\Omega \cos\phi u = -\frac{\partial p}{\partial z^*} - g \frac{p}{\rho_0} \quad (3.4)$$

$$\frac{1}{R \cos\phi} \left[ \frac{\partial u}{\partial \lambda} + \frac{\partial}{\partial \phi} (v \cos\phi) \right] + \frac{\partial w}{\partial z^*} = 0 \quad (3.5)$$

$$\frac{\partial p}{\partial t} - \frac{\rho_0}{g} N^2(z^*) w = 0 \quad (3.6)$$

where  $u$ ,  $v$ ,  $w$ , are the zonal, meridional, and radial components of velocity;  $p$  is the pressure;  $\rho$  and  $\rho_0$  are the perturbation and mean density;  $g$  is the gravity constant;  $N(z^*)$  is the buoyancy frequency at depth  $z^*$ ;  $R$  and  $\Omega$  are the radius and rotational frequency of the earth;  $\phi$  and  $\lambda$  are the latitude and longitude.

Because the inertial frequency is usually much smaller than the buoyancy frequency in the ocean, the acceleration of vertical velocity can be neglected in (3.4) for inertial waves -- the hydrostatic approximation. For wave motions of small vertical extent, which is the case of large scale waves as a consequence of condition (iv), the vertical velocity is smaller than the horizontal ones by a factor of

order ( $H/R$ ), where  $H$  is the ocean depth. Therefore the term  $2\Omega \cos\phi w$  in (3.2) can be neglected on this ground. The term  $2\Omega \cos\phi u$  in (3.4) is almost always neglected for the convenience of maintaining a self-adjoint system (Eckart, 1960). Phillips (1966) showed that these two terms had to be neglected in Eqs. (3.2)-(3.6) in order to satisfy the conservation of angular momentum (also see Veronis, 1968). The approximation associated with the neglect of the horizontal component of the earth's rotation is usually called the "traditional approximation", which makes the solutions to (3.2) -- (3.6) separable.

### 3.2 The traditional approximation

Among the various approximations mentioned above, the traditional approximation is the most controversial one and satisfactory justification is hard to find in the literature. The neglect of the terms involving  $2\Omega \cos\phi$  is formally correct in the limit  $H/R \rightarrow 0$ . For a homogeneous fluid, the resulting equations are the famous Laplace's tidal equations (LTE hereafter; c.f. Lamb, 1932). Stewartson and Rickard (1969) carried out a formal expansion in powers of  $H/R$ , in which the first term was the Longuet-Higgins' solution of the LTE (1968). They found that, near the inertial latitudes where  $\sin\phi = \pm \frac{\omega}{2\Omega}$ , there was an unintegrable singularity in the second order terms. After developing an inner expansion around the inertial latitudes, they could not match the inner and outer solutions and described the perturbation solutions as "pathological". Moreover, the pathological solutions were not confined within the neighborhood of inertial latitudes, but spread over the whole sphere. By introducing a constant weak stratification  $N$  and making a

double expansion in  $H/R$  and  $(N/\Omega)^2(H/R)^2$ , Stewartson and Walton (1976) were able to resolve the matching problem and obtained regular solutions for  $1 \gg (N/\Omega)^2(H/R)^2 \gg (H/R)^{3/2}$ . However, these solutions are still pathological in the sense that the scale of the second order motion is order  $(N/\Omega)(H/R)$  smaller than that of the basic motion and vanishes as  $H/R \rightarrow 0$ . Miles (1974) pointed out that the fundamental problem of Stewartson and Walton's expansion was the failure of the solutions of the LTE for homogeneous fluid (the first order terms) to provide an adequate description of the characteristics of the primitive equation in the hyperbolic domain. He showed that, by retaining stratification in the basic equations, the resulting double infinity of modes (i.e., the barotropic and an infinite set of baroclinic modes) could be used as expansion functions to obtain uniformly valid second order solutions. The barotropic and baroclinic modes are coupled by the horizontal component of the earth's rotation at the second order. This coupling decreases with increasing stratification. The inhibiting effect of stratification on the influence of the horizontal component of the earth's rotation was also noted by Phillips (1968), Needler and LeBlond (1973), Kamenkovich and Kulakov (1977).

Miles (1974) showed that, for free oscillations with frequency  $\omega < 2\Omega < N$ , the partial differential equation resulting from (3.2)--(3.6) is elliptic (hyperbolic) poleward (equatorward) of the two critical latitudes satisfying

$$\sin \phi = \frac{\omega}{2\Omega} \left[ 1 + \frac{4\Omega^2}{N^2} \left( 1 - \frac{\omega^2}{4\Omega^2} \right) \right]$$

In general, the critical latitudes are greater than  $\pm \sin^{-1}(\frac{\omega}{2\Omega})$ , the inertial latitudes. For strong stratification such that  $\frac{4\Omega^2}{N^2} \ll 1$ , the critical latitudes tend to coincide with the inertial latitudes, and the traditional approximation is formally valid. In the deep ocean where  $\frac{4\Omega^2}{N^2} \lesssim .1$ , then one may find some appreciable sub-inertial energy due to this broadening of internal wave frequency band.

### 3.3 Asymptotic solutions

It is well-known that packets of internal waves in the ocean propagate along ray paths which undergo reflections at the vertical boundaries and the turning latitudes where the latitudinal wavenumber vanishes. A linear random wave field is represented by the superposition of ray paths of different frequencies and wavenumbers. However, the statistical behavior of the wave field also can be described by a set of equivalent modes as proposed by Garrett and Munk (1972). Because modal solutions are more easily obtained than ray solutions, we proceed based on periodic solutions which have modal structure in depth and are separable in each coordinate as follows:

$$\begin{bmatrix} u \cos \phi \\ v \cos \phi \\ p \end{bmatrix} = A \operatorname{Real} \left\{ F(z^*) \exp[i(k\lambda - \omega t)] \begin{bmatrix} U(\phi) \\ iV(\phi) \\ 2\Omega R P(\phi) \end{bmatrix} \right\} \quad (3.7)$$

$$\begin{bmatrix} P \\ \\ W \end{bmatrix} = A \operatorname{Real} \left\{ W(z^*) \exp[i(k\lambda - \omega t)] \begin{bmatrix} \frac{\rho_0 N^2(z^*)}{g \omega} \\ \\ -i \end{bmatrix} P(\phi) \right\} \quad (3.8)$$

where  $U$ ,  $V$ ,  $P$ ,  $F$ ,  $W$  are dimensionless functions, and  $A$  is a normalization factor with the dimension of velocity. Defining the dimensionless depth  $z = z^*/H$ , frequency  $\sigma = \omega/2\Omega$ , and buoyancy frequency  $\tilde{N}(z) = N(z^*)/N_0$ , the substitution of (3.7) and (3.8) into (3.2) — (3.6) yields

$$\sigma U + \sin\phi V = kP \quad (3.9)$$

$$\sin\phi U + \sigma V = -\cos\phi \frac{dP}{d\phi} \quad (3.10)$$

$$\frac{dF}{dz} + \frac{N_0^2 H}{4\Omega^2 R \sigma} \tilde{N}^2(z) W = 0 \quad (3.11)$$

$$\frac{1}{\sigma \cos^2\phi P} \left[ kU + \cos\phi \frac{dV}{d\phi} \right] = \frac{R}{H\sigma F} \frac{dW}{dz} = \epsilon \quad (3.12)$$

where the hydrostatic and traditional approximations have been used. Eq. (3.12) states the condition of separability, where  $\epsilon$  is the separation constant which is related to the equivalent depth  $h$  (Lindzen, 1967) by

$$\epsilon = \frac{4\Omega^2 R^2}{gh} \quad (3.13)$$



The vertical equation can be obtained from (3.11) and (3.12),

$$\frac{d^2 W}{dz^2} + \epsilon \int_{-1}^z \tilde{N}^2(z') dz' = 0, \quad (3.14)$$

where  $S = N_0 H / 2 \Omega R$ . The boundary conditions are

$$W = 0 \quad \text{at } z = 0, -1 \quad (3.15)$$

Because the specific form of  $N(z)$  is not crucial to the qualitative results, we use the same  $N(z)$  of Garrett and Munk (1972),

$$N(z) = N_0 \exp(-zH/b), \quad (3.16)$$

where  $N_0 = 3$  cph,  $b = 1.3$  km, and  $H = 4.5$  km. The solutions of the eigenvalue problem posed by (3.14) and (3.15) are readily obtained and the eigenvalues are

$$\begin{aligned} \epsilon_1 &= 1.63 \times 10^5, \\ \epsilon_2 &= 7.39 \times 10^5, \\ \epsilon_j &= 1.96 \times 10^5 \times j^2, \quad (j \geq 3) \end{aligned}$$

where the subscripts are the vertical mode numbers. For high modes, the WKBJ solutions for  $F(z)$  and  $W(z)$  are

$$\begin{aligned} W_j(z) &= \frac{-2\Omega\sigma}{N_0} \epsilon_j^{1/2} \tilde{N}^{-1/2} \exp\left[i \int_{-1}^z \epsilon_j^{1/2} S \tilde{N}(z') dz' + \frac{\pi}{2}\right] \\ F_j(z) &= \tilde{N}^{1/2} \exp\left[i \int_{-1}^z \epsilon_j^{1/2} S \tilde{N}(z') dz'\right] \end{aligned} \quad (3.17)$$

The latitudinal equation can be obtained by eliminating  $U$  from (3.10) and (3.12), yielding

$$\cos\phi \frac{dP}{d\phi} + \frac{k \sin\phi}{\sigma} P = \left( \frac{\sin^2\phi}{\sigma} - \sigma \right) V \quad (3.18)$$

$$\cos\phi \frac{dV}{d\phi} - \frac{k}{\sigma} \sin\phi V = \left( \epsilon \sigma \cos^2\phi - \frac{k^2}{\sigma} \right) P \quad (3.19)$$

Eliminating  $P$  from (3.18) and (3.19), we have the LTE in terms of  $V$ :

$$\begin{aligned} & \cos\phi \frac{d}{d\phi} \left( \cos\phi \frac{dV}{d\phi} \right) + \left[ \epsilon \cos^2\phi (\sigma^2 - \sin^2\phi) - \frac{k}{\sigma} \cos^2\phi - k^2 \right] V \\ &= \frac{2\epsilon \cos^2\phi \sin\phi \left[ \frac{k}{\sigma} \sin\phi V - \cos\phi \frac{dV}{d\phi} \right]}{\epsilon \cos^2\phi - \frac{k^2}{\sigma^2}} \end{aligned} \quad (3.20)$$

Longuet-Higgins (1965) showed that, for large  $\epsilon$ , the right-hand side of (3.20) can be neglected with an error  $O(\epsilon^{-1/2})$  of the left-hand side. As pointed out in MP, this error is not uniform in  $\phi$ , and becomes  $O(\epsilon^{-1/3})$  near the inertial latitudes ( $\sin\phi = \pm\sigma$ ).

But another more serious non-uniformity associated with the apparent singularity at  $\cos\phi = \frac{k}{\sigma\epsilon^{1/2}}$ , where the denominator in (3.20) vanishes, has not been discussed. For inertial waves,  $k \lesssim O(\epsilon^{1/3})$  (see MP); hence  $\frac{k}{\sigma\epsilon^{1/2}} \ll 1$  if  $\sigma \sim O(1)$ . The singular latitude is near the poles which is far from the turning latitudes of mid-latitude inertial waves. Because the wave amplitudes are virtually vanishing there, this singularity is of no importance. But for low-latitude inertial waves with  $\sigma \ll 1$ , this singularity would occur equatorward

of their turning latitudes and seriously affects the solutions. The lower limit in latitude for the validity of neglecting the right-hand side of (3.20) is about  $4^\circ$  for the first baroclinic mode and decreases with mode number. Thus the following discussion is restricted to latitudes greater than  $4^\circ$  and the right-hand side of (3.20) is neglected for now. It is shown in Chapter 4 that, however, the validity of one turning point solutions on which our model is based is restricted to latitudes at least greater than  $10^\circ$ .

The following derivation of the asymptotic solutions basically follows MP. Introducing the Mercator coordinate  $\mu$  which is defined as

$$\mu = \int_0^\phi \sec \phi' d\phi' \quad (3.21)$$

we can eliminate the first derivative term in (3.20) and obtain the spheroidal wave equation in the following form,

$$\frac{d^2 V}{d\mu^2} + l^2 V = 0 \quad (3.22)$$

where

$$l^2 = \epsilon \cos^2 \phi (\sigma^2 - \sin^2 \phi) - \frac{k}{\sigma} \cos^2 \phi - k^2 \quad (3.23)$$

It is clear that  $l$  is equivalent to a latitudinal wavenumber. The turning latitude  $\phi_s$  is then defined as the latitude where  $l = 0$ . From (3.23) we have

$$2 \sin^2 \phi_s = 1 + \sigma^2 - \frac{k}{\sigma \epsilon} - \left[ \left( 1 - \sigma^2 + \frac{k}{\sigma \epsilon} \right)^2 + \frac{4k^2}{\epsilon} \right]^{1/2} \quad (3.24)$$

It can be seen from (3.22) that  $\phi_s$  is the boundary between the

evanescent (poleward) and oscillatory (equatorward) domain of the solution. It is also the latitude where the wave rays reflect back to the equator (Longuet-Higgins, 1965). Hence the basic behavior of the solution is controlled by the location of  $\phi_s$ . In Fig. 3.1,  $\phi_s$  is shown as a function of  $2\pi/k$  for different vertical modes with  $\sigma = 0.5878$ . In general,  $\phi_s$  approaches the inertial latitude with increasing  $\epsilon$  and/or  $2\pi/k$ .

In terms of  $\phi_s$ , (3.23) can be written as

$$l^2 = (\sin^2 \phi_s - \sin^2 \phi) (\epsilon \cos^2 \phi + k^2 \sec^2 \phi_s) \quad (3.25)$$

With the Langer transformation in  $\phi$ ,

$$\frac{2}{3} \xi^{3/2} = \int_{\phi}^{\phi_s} (\sin^2 \phi_s - \sin^2 \phi')^{1/2} d\phi', \quad (3.26)$$

a uniformly valid asymptotic solution of (3.22) is obtained:

$$V = \left( \frac{d\xi}{d\mu} \right)^{-1/2} Ai(-\epsilon^{1/3} \xi) \left[ 1 + O(\epsilon^{-1/2}) \right], \quad (3.27)$$

where  $Ai$  is the Airy function which satisfies the boundary condition  $V = 0$  at  $\infty$ . Because we are considering a one turning point problem, the boundary conditions at the other turning latitude can be ignored, and a continuous spectrum in  $k$  is allowed. The solutions for  $U$  and  $P$  can be readily obtained by substituting (3.27) into (3.9) and (3.19). The integral of (3.26) can be evaluated in terms of elliptic functions (see Appendix B). When  $\phi \approx \phi_s$ , the Taylor expansion of (3.26) is

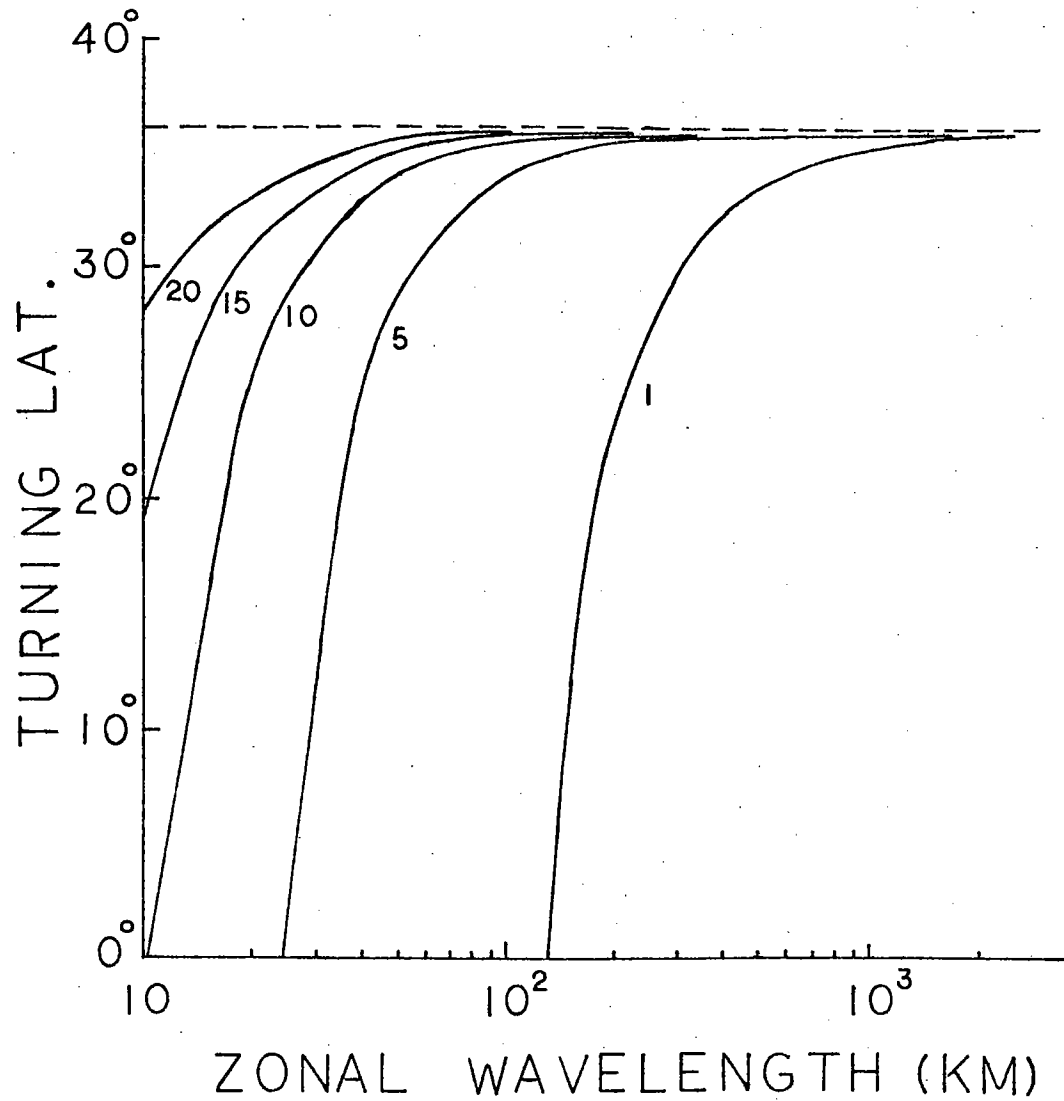


Figure 3.1 Turning latitudes of waves with  $\sigma = 0.5878$  as functions of zonal wavelength for different vertical modes. The number next to each curve is the mode number. Dashed line indicates the inertial latitude (36°).

$$\xi = (\sin 2\phi_s)^{1/3} (\phi_s - \phi) \left[ 1 - \frac{1}{5} \cot 2\phi_s (\phi_s - \phi) + \dots \right] \quad (3.28)$$

The controlling scale near  $\phi_s$  is the "Airy scale" defined as

$$L = \left( \epsilon \sin 2\phi_s \right)^{-1/3}, \quad (3.29)$$

whose values for the first and tenth vertical modes at selected latitudes are shown in Table 3.1.  $L$  is symmetrical about the latitude of  $45^\circ$ , and approaches infinity near the poles and the equator, where this scale becomes irrelevant. Fig. 3.2 shows schematically the

Table 3.1

Airy scales for the 1st and 10th vertical modes.

Parenthetical values are in km.

<u>Latitude(deg)</u>	$L_1$	$L_{10}$
5	.033 (210)	.0066 (42)
15	.023 (146)	.0046 (30)
30	.019 (121)	.0039 (25)
45	.018 (115)	.0037 (24)

variation of the solutions represented by (3.27) with respect to  $k$  and  $\epsilon$ . For latitudinally propagating waves with  $k = 0$ ,  $\phi_s$  is equal to

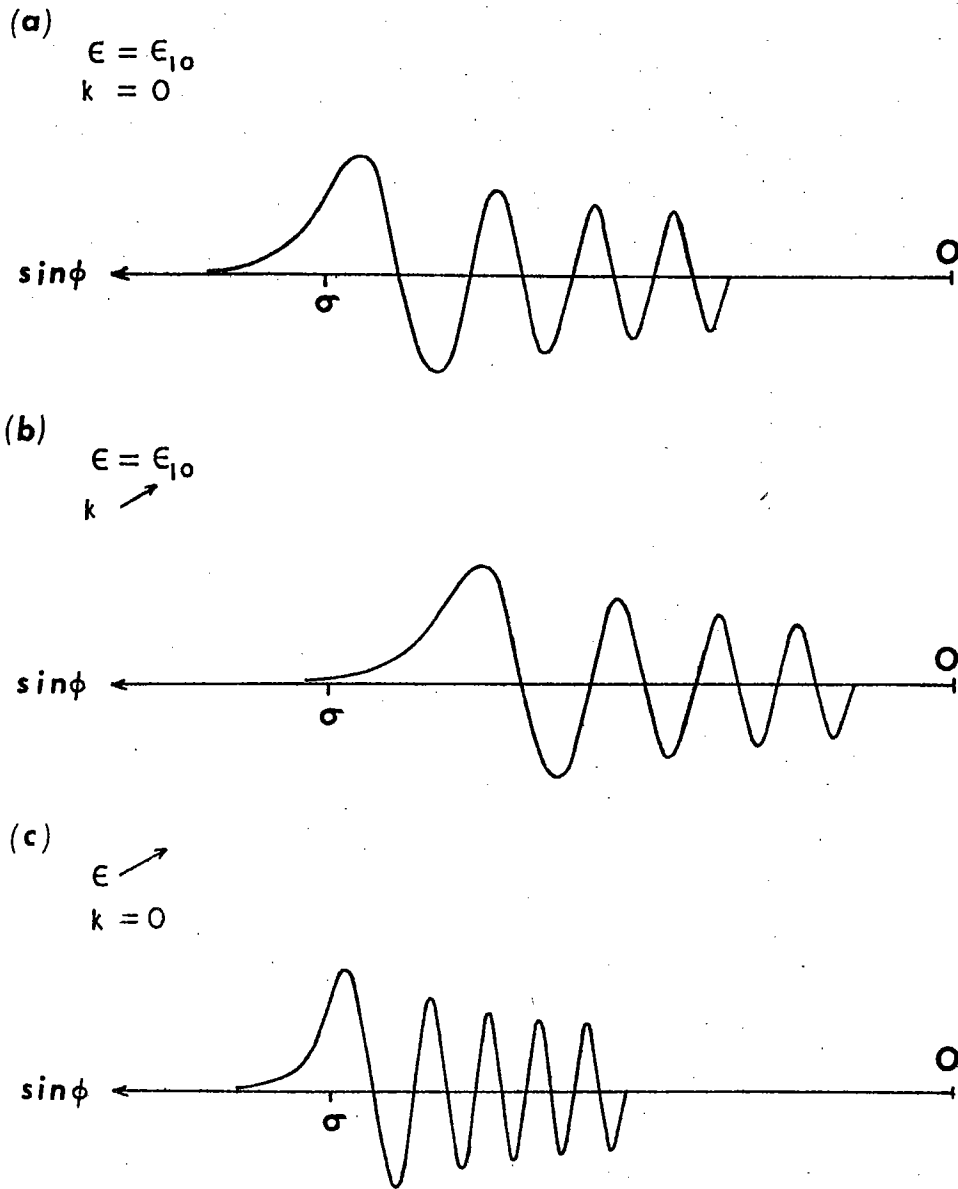


Figure 3.2 Schematic diagram showing the variation of the wave function  $V$  with respect to  $k$  and  $\epsilon$ . Horizontal axis is the sine of latitude;  $\sigma$  corresponds to the inertial latitude.  $k \nearrow$  means increasing the value of  $k$ .

$\sin^{-1}(\sigma)$ . An increase in  $k$  tends to shift  $\phi_s$  equatorward of  $\sin^{-1}(\sigma)$ ; an increase in  $\epsilon$  tends to decrease the latitudinal scale as implied in Eq. (3.29). Therefore, the observations of inertial peak only a few percent above  $f$  imply a fairly large zonal wavelength. For instance, assuming that the dominant wave has a tenth-mode vertical structure, then the observation of an inertial peak with 2.5 % blue shift at  $35^\circ$  implies that  $\phi_s$  should be  $35.3^\circ$ . From Fig. 3.1, we can infer that the zonal wavelength is, of the order of 100 km.

#### 3.4 The WKBJ approximation

For high frequency internal waves,  $\sigma \gg \sin\phi$ , we can apply the WKBJ approximation to (3.22) and obtain the zero order solutions used in the GM model. But how much greater than  $\sin\phi$  should  $\sigma$  be for the WKBJ solutions to be valid? To answer this question, we have to look into the error terms in detail. In general, the error of the WKBJ solutions, denoted by  $\delta$ , is growing when approaching turning points. For Eq. (3.22),  $\delta$  can be written as (Mathews and Walker, 1970, p.27)

$$\delta = \frac{d(l^2)}{d\mu} \frac{1}{(l^2)^{3/2}} \quad (3.30)$$

Then from (3.25), we have

$$\delta = \frac{2 \sin\phi \cos^2\phi \left[ 1 - 2\sin^2\phi + \sin^2\phi_s + \frac{k^2}{\epsilon \cos^2\phi_s} \right]}{\epsilon^{1/2} \left[ (\sin^2\phi_s - \sin^2\phi) \left( \cos^2\phi + \frac{k^2}{\epsilon \cos^2\phi_s} \right) \right]^{3/2}} \quad (3.31)$$

For given  $\phi$ ,  $\epsilon$ , and  $k$ , we can find from (3.31) a frequency  $\sigma_c$  beyond which  $\delta$  is less than some pre-specified value, say, 0.1. In general,  $\sigma_c$



is the root of a nonlinear algebraic equation. However, when  $k = 0$ ,  $\sigma_c$  can be approximated by

$$\sigma_c \approx \sin \phi (1 + 10 L \cot \phi) , \quad (3.32)$$

where  $L$  is the Airy scale at  $\phi$ . Because for given  $\phi$ ,  $\epsilon$ , and  $\sigma$ ,  $\delta$  is minimum when  $k = 0$ , the  $\sigma_c$  given by (3.32) represents a lower bound for frequency below which the WKBJ solutions are invalid for any value of  $k$ . The values of  $\sigma_c$  calculated using (3.32) for the first and tenth modes at selected latitudes are shown in Table 3.2. Since the observed vertical wavenumber spectrum (Leaman and Sanford, 1975) suggests that most of the internal wave energy is contained in low modes,  $\sigma_c$  of the tenth mode is probably the lower bound for the validity of the WKBJ approximation and the GM model.

Table 3.2

Values of the critical frequency of the 1st and 10th vertical modes.

Latitude(deg)	$\frac{\sigma_c}{\sin \phi}$ (j=1)	$\frac{\sigma_c}{\sin \phi}$ (j=10)
5	4.75	1.75
15	1.86	1.17
30	1.33	1.07
45	1.18	1.04
60	1.11	1.02

### 3.5 Discussion

At latitudes sufficiently away from the equator ( $\geq 40^\circ$ ), the asymptotic solutions to the spheroidal wave equation as obtained by MP are valid with an error no greater than  $O(\epsilon^{-1/3})$ . The WKBJ solutions used in the GM model are valid for frequencies higher than a critical value  $\sigma_c$ , which is dependent on vertical mode numbers. The value of  $\sigma_c$  corresponding to the tenth vertical mode is used as a critical frequency in the calculation of wave functions in the next chapter : for frequencies higher than  $\sigma_c$ , the WKBJ solutions will be used; for frequencies lower than  $\sigma_c$ , the spheroidal wave solutions will be used.

## Chapter 4 A Model Spectrum for the Global Inertial Wave Field

### 4.1 Introduction

In the light of the observations presented in Chapter 2, whatever mechanisms are responsible for the universality of the internal wave spectrum at high frequencies do not seem to apply near  $f$ . The spectral shape near  $f$  has a strong dependence on geographical location, suggesting a strong influence of local sources and/or sinks. Presumably the internal wave spectrum is determined by the radiation balance equation which involves generation, dissipation, propagation and nonlinear interaction (c.f. Müller and Olbers, 1975). Because low mode waves contain most of the energy, they have a dominant influence on the frequency spectrum. McComas and Bretherton (1977) reported that near  $f$  the interaction time scales for low mode waves are very long as compared to their periods. Therefore nonlinear interactions may not be important for the existence of the inertial peak. Major dissipation of these waves is probably taking place only at the ocean bottom, and it will be shown in Chapter 6 that the resulting reflection coefficient is near unity and hence the dissipation rate is small. Therefore the main cause for the observed inertial peak is likely to be a combination of the generation and propagation of internal waves in the open ocean.

Low frequency internal waves randomly generated at lower latitudes can propagate to their inertial latitude and become, by definition, inertial waves, as long as their zonal wavenumbers are small enough. The inertial wave field of this origin is defined in Chapter 1 as the global

wave field. In addition, there are several possible local forcing mechanisms for inertial waves : wind forcing, energy cascades from sub-inertial frequencies, interactions between low frequency eddies and rough topography, etc. Among these, the wind forcing is probably the best understood and also the most important source. In the mixed layer, inertial currents are forced as a direct response to local winds and could propagate along ray paths to the deep ocean nearby with possibly appreciable amplitudes (Kroll, 1975). This would result in a predominantly downward propagating wave field which is defined in Chapter 1 as the local wave field. To distinguish the local wave field from the global wave field in the observed spectra is the major task of this chapter. Determination of the spectrum of wind forced inertial waves requires detailed knowledge of the wind spectrum which is poorly known near the inertial frequency. Furthermore, boundary layer dynamics near the inertial frequency are also poorly understood. We will therefore proceed in the other direction -- first determining the global wave spectrum and then ascribe the residual to local forcing.

Because the  $f$ - $w$  spectrum of the global wave field is well described by the GM model at lower latitudes where the WKBJ approximation is valid, the frequency spectrum near  $f$  can be obtained by using the GM model and the wave functions derived in Chapter 3. Thus the difference between the global wave spectrum and the observed spectrum can be interpreted as the result of locally forced waves.

#### 4.2 The Garrett and Munk Model

Under the assumption of stationarity and homogeneity of internal

waves in the ocean, Garrett and Munk (1972) patched together a great number of observations of different origins, trying to seek a universal f-w spectrum. In their work, the following additional assumptions were made :

(1) the observed motion is interpreted as linear superposition of internal waves with random phase relations.

(2) horizontal isotropy and vertical symmetry, i.e., there is no preferred directionality.

(3) the WKBJ approximations for the wave functions in both the vertical and latitudinal variable.

Then the energy density can be written as  $E(\alpha, \omega)$ , which depends only on two variables : the frequency  $\omega$  and horizontal wavenumber  $\alpha$ .

Because the observed vertical coherences were independent of frequency, they proposed the following separable form for  $E(\alpha, \omega)$  :

$$E(\alpha, \omega) = E_c A(\lambda) B(\omega), \quad (4.1)$$

$$\text{where } \lambda = \frac{\alpha}{\alpha_*}, \quad \alpha_* = j_* \pi (\omega^2 - f^2)^{\frac{1}{2}}, \quad j_* = 20, \quad (4.2)$$

$$A(\lambda) = \frac{1}{\alpha_*} (\lambda \leq 1); \quad 0 (\lambda > 1) \quad (4.3)$$

$$B(\omega) = \frac{2}{\pi} f \omega^{2s-2} (\omega^2 - f^2)^{-s}, \quad s = \frac{1}{2} \quad (4.4)$$

The spectrum represented by (4.1)--(4.4) is usually referred as "GM72".

The wavenumber spectrum  $A(\lambda)$  is of top hat shape with cutoff mode

number  $j_*$  deduced from vertical coherence measurements. The particular

form of  $B(\omega)$  is chosen to behave like  $\omega^{-2}$  when  $\omega \gg f$  and also to have an integrable cusp at  $f$ . The  $\omega^{-2}$  behavior when  $\omega \gg f$  is supported by observations in most parts of the deep ocean. But the cusp with  $s = 1/2$  is arbitrary, and is there only to satisfy the condition of integrability which requires  $0 < s < 1$ . After admitting that observed motions with relatively high wavenumbers are indeed internal waves rather than fine structures, Garrett and Munk (1975) modified  $A(\lambda)$  so that it falls off smoothly with a high wavenumber slope,

$$A(\lambda) = (t-1)(1+\lambda)^{-t} / \alpha_* \quad , \quad (4.5)$$

where  $t = 2.5$ , and  $\alpha_*$  corresponds to  $j_* = 6$ . The model with this modification is usually referred as "GM75". Using relatively less contaminated observations from a mid-water float, Cairns and Williams (1976) showed that  $t = 2$  and  $j_* = 3$  are probably better fits.

With normalized wave functions of horizontal velocity  $X(z, \omega)$ , and vertical displacement  $Z(z, \omega)$ , the corresponding frequency spectra are

$$\int_{-\infty}^{\infty} [X^2(z, \omega), Z^2(z, \omega)] E(\alpha, \omega) d\alpha \quad (4.6)$$

As a consequence of the underlying WKBJ approximations for  $X$  and  $Z$ , the above description applies only for  $f \ll \omega \ll N(z)$ . Analytical representations of various spectral quantities based on GM75 were derived by Desaubies (1976).

### 4.3 The global inertial wave model

#### 4.3a Normalization

In order to be useful in the spectrum calculations, the wave functions derived in 3.3 have to be normalized at some low latitude where the WKBJ approximation is valid. Quite naturally and conveniently, we choose the equator for formal normalization. The observed small vertical coherence scales near the equator (Wunsch and Webb, 1979) suggest that the wavenumber bandwidth there is greater than what is given by the GM model, but this is irrelevant because the model is not applied on the equator. The normalization condition requires that

$$\int_{-1}^0 \left[ \frac{1}{2} (u^2 + v^2 + w^2) + \frac{1}{2} \frac{g^2 \rho^2}{\rho_0^2 N^2} \right] dz = 1 \quad (4.7)$$

at the equator. After substituting (3.7) and (3.8) into (4.7), we have

$$A^2 \int_{-1}^0 \left[ \frac{1}{2} \overline{F^2} (U^2 + V^2) + \frac{1}{2} \overline{W^2} \left( 1 + \frac{N^2}{w^2} \right) P^2 \right] dz = 1 \quad (4.8)$$

where  $\overline{F^2}$  and  $\overline{W^2}$  are the squares of  $F(z)$  and  $W(z)$  averaged over depth.

From (3.17), we have

$$\overline{W^2} = \frac{4\Omega^2 \sigma^2}{N_0^2} \in \tilde{N}^{-1}(z)$$

and

$$\overline{F^2} = \tilde{N}(z)$$

Using the solutions obtained in 3.3 for  $U$ ,  $V$ , and  $P$ , and their

asymptotic approximations at  $\phi = 0$ , the following results are obtained :

$$A^2 = \frac{\epsilon^{1/6} \sin \phi_s}{J \left\{ 1 + \frac{\sin^2 \phi_s (\sigma^2 + \frac{k^2}{\epsilon})}{(\sigma^2 - \frac{k^2}{\epsilon})^2} \right\}} + O(\epsilon^{-1/3}), \quad (4.9)$$

where

$$J = \frac{b(1 - e^{-H/b})}{2\pi H}$$

#### 4.3b Construction of frequency spectra

With wave functions given by (3.7), (3.8), and (4.9), the frequency spectra of  $v$  component velocity and density at latitude  $\phi$  and depth  $z$  can be written as

$$E_v(\omega, \phi, z) = \sum_{j=1}^m \int_{-\infty}^{\infty} G(k, j, \omega) |v(k, \epsilon_j, \omega, \phi, z)|^2 dk$$

$$E_p(\omega, \phi, z) = \sum_{j=1}^m \int_{-\infty}^{\infty} G(k, j, \omega) |\rho(k, \epsilon_j, \omega, \phi, z)|^2 dk, \quad (4.10)$$

where  $j$  is the vertical mode number,  $m$  is the maximum mode number, and  $\omega$  is the frequency.  $G(k, j, \omega)$  is the  $f$ - $\omega$  spectrum of the following form :

$$G(k, j, \omega) = E_0 \left(\frac{\omega}{\omega_0}\right)^{-2} C(j) D(k, j, \omega), \quad (4.11a)$$

$$\text{where } C(j) = \frac{(1 + j/j_*)^{-t}}{\sum_{j=1}^m (1 + j/j_*)^{-t}}, \quad (4.11b)$$



and  $E_0$  is the total energy per unit mass per cph averaged over depth at the equator. The frequency and vertical mode distributions have the same forms as those of GM75, but we need some arguments to choose a proper zonal wavenumber spectrum  $D(k, j, \omega)$  for given  $\omega$  and  $j$ .

For  $\omega \gg f$ , the assumption of horizontal isotropy requires that energy density be a function of total wavenumber  $\alpha$  only, which is defined as

$$\alpha = (k^2 + l^2)^{1/2},$$

where  $l$  is given by Eq.(3.23). It can be shown that for  $\omega \gg f$ ,

$$\alpha \approx \epsilon^{1/2} \cos \phi \frac{(\omega^2 - f^2)^{1/2}}{2\Omega} \sim O(\epsilon^{1/2}). \quad (4.12)$$

Because  $k = \alpha \cos \theta$

and  $D(k, j, \omega) dk = \frac{l}{2\pi} d\theta$ ,

where  $\theta$  is the azimuthal angle, we have

$$D(k, j, \omega) = \frac{l}{\pi \alpha} \left[ 1 - \left( \frac{k}{\alpha} \right)^2 \right]^{-1/2} \quad (\omega \gg f) \quad (4.13)$$

For  $\omega \approx f$ , we can no longer interpret  $l$  as a local latitudinal wavenumber, because the wave functions are no longer periodic in latitude; the direction of propagation is primarily zonal, and we do not have a clear definition of horizontal isotropy for inertial waves. The

following two models are therefore proposed for  $D(k, j, \omega)$  when  $\omega \approx f$  :

Model 1

Let us first find the range of  $k$  for given  $\omega$  and  $j$ , i.e., the cutoff wavenumbers  $-k_1$  and  $k_2$  which satisfy the following equation :

$$2 \sin^2(\phi - L_j) = 1 + \sigma^2 - \frac{k}{\sigma \epsilon_j} - \left[ \left( 1 - \sigma^2 + \frac{k}{\sigma \epsilon_j} \right)^2 + \frac{4k^2}{\epsilon_j} \right]^{1/2}, \quad (4.14)$$

which are obtained from (3.24) by setting  $\phi_s = \phi - L_j$ . Thus  $-k_1$  and  $k_2$  are the zonal wavenumbers for which the  $j$ th mode wave with frequency  $\sigma$  will turn at  $\phi - L_j$ . The reason for setting  $\phi_s = \phi - L_j$  instead of  $\phi_s = \phi$  is that, the wave amplitude is appreciable to latitudes one Airy scale north of the turning latitude (see Fig. 3.2).

The solutions of (4.14) are

$$\left. \begin{array}{l} -k_1 \\ k_2 \end{array} \right\} = \frac{-\cos \theta}{4\sigma} \mp \frac{\epsilon_j^{1/2} \cos \theta}{\sigma} \left( \sigma^4 - \sigma^2 \sin^2 \theta + \frac{\cos^2 2\theta}{16 \epsilon_j \cos^2 \theta} \right)^{1/2},$$

where  $\theta = \phi - L_j$ . For  $\omega \approx f$ , the above expression can be approximated by

$$\left. \begin{array}{l} -k_1 \\ k_2 \end{array} \right\} = \mp k_0 + O(1) \quad (4.15a)$$

$$\text{where } k_0 = \cos \phi L_j^{-3/2} \left[ \frac{\omega - f}{2\Omega \cos \phi} + L_j \right]^{1/2} \sim O(\epsilon^{1/3}) \quad (4.15b)$$

Thus the zonal wavenumber of inertial waves is restricted to  $-k_0 < k < k_0$ . If inertial waves, as in the case of global generation, are propagating from equatorward of their turning latitudes where  $D(k, j, \omega)$

is given by Eq. (4.13), we must have (when  $\omega \approx f$ )

$$D(k, j, \omega) \propto \left[ 1 - \left( \frac{k}{\alpha} \right)^2 \right]^{-1/2} \quad \text{with } |k| \leq k_0,$$

because  $k$  is conserved along ray paths. From Eqs. (4.15b) and (4.12), we have

$$\frac{k}{\alpha} \sim O(\epsilon^{-1/6})$$

and

$$D(k, j, \omega) \propto 1 + O(\epsilon^{-1/3}).$$

Hence  $D(k, j, \omega)$  can be approximated by a constant when  $|k| \leq k_0$ , and the Model 1 for  $D(k, j, \omega)$  is formally defined as

$$\begin{aligned} D(k, j, \omega) &= \frac{1}{2k_0} && \text{for } |k| \leq k_0, \\ &= 0 && \text{for } |k| > k_0. \end{aligned} \quad (4.16)$$

Eq. (4.16) therefore represents the zonal wavenumber spectrum of an inertial wave field which can be mapped onto an isotropic internal wave field at lower latitudes.

#### Model 2

Although there is no latitudinal propagation when  $\omega \approx f$ , we can still think of  $(k^2 + \ell^2)^{1/2}$ , which is equal to  $k_0$  as given by (4.15b), as a total wavenumber and define  $D(k, j, \omega)$  according to Eq. (4.13) as follows :

$$D(k, j, \omega) = \frac{1}{\pi k_0 \left[ 1 - \left( \frac{k}{k_0} \right)^2 \right]^{1/2}} \quad \text{for } |k| \leq k_0 \quad (4.17)$$

$$= 0 \quad \text{otherwise.}$$

This is actually an artificial definition of horizontal isotropy for inertial waves which can propagate only in the zonal direction. There is not any physical ground for the Model 2 except using the same form of  $D(k, j, \omega)$  at all frequencies. Fig. 4.1 shows the zonal wavenumber spectra corresponding to these two models.

With these two models for  $D(k, j, \omega)$ , the integrals in (4.10) were calculated numerically up to the critical frequency  $\sigma_c$  of the tenth vertical mode as discussed in Section 3.4, where the spectra can be matched with GM75. The accuracy of the results was assured when no significant improvements were observed by reducing the integration step.

#### 4.3c Model results and their sensitivity

Because of the nearly circular motion of inertial waves, the spectra of the two horizontal velocity components,  $E_u(\omega)$  and  $E_v(\omega)$ , are the same, and the result for  $E_v(\omega)$  can be viewed as the horizontal kinetic energy (H.K.E.) spectrum. The potential energy (P.E.) spectrum can be derived from  $E_p(\omega)$  as

$$E_{PE}(\omega) = \frac{1}{2} \frac{g^2 E_p(\omega)}{\rho_0^2 N^2} \quad (4.18)$$

Because of the WKBJ approximation in the vertical wave functions,  $E_v$  and  $E_{PE}$  are proportional to  $N(z)$ .

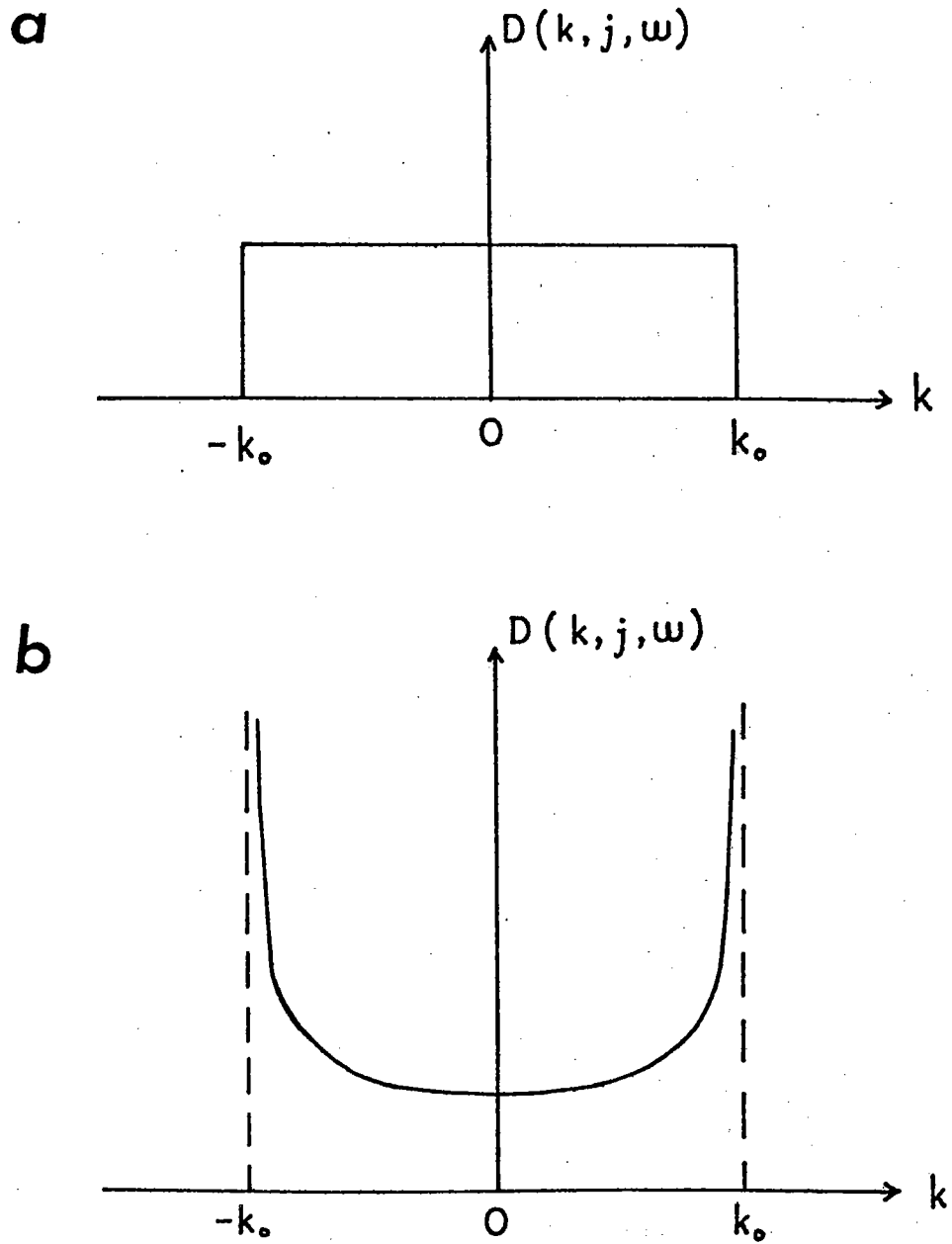


Figure 4.1 Schematic representation of the zonal wavenumber spectra of (a) Model 1 and (b) Model 2.

With  $D(k, j, \omega)$  given by Model 1,  $m = 20$ ,  $t = 2.5$ , and  $j_* = 6$ ,  $E_V(\omega)/N(z)$  and  $E_P(\omega)/N(z)$  were calculated at five selected latitudes, of which some were chosen to be where there were observations. The results are shown in Fig. 4.2, where the scale of the ordinate corresponds to  $E_0/N_0 = 0.03 \text{ cm}^2/\text{sec}^2/\text{cph}^2$ , an estimate from the comparisons with observations to be discussed later in 4.4. Using the same values for  $j_*$ ,  $t$ ,  $m$ , and  $E_0/N_0$ , the normalized energy spectra at  $32^\circ$  with  $D(k, j, \omega)$  given by Model 2 are shown in Fig. 4.3. Because the latitudinal dependence is the same as in Fig. 4.2, the spectra at other latitudes are not shown. The only difference between these two models is a slightly weaker peak in the kinetic energy spectrum of Model 2 -- 4.5 db as compared to 7 db. Because such a small difference -- a factor less than two -- is very difficult to distinguish in the observations, only Model 1 will be used from hereon.

Fig. 4.2 thus describes a mapping of the GM spectrum from the equator onto higher latitudes. The changes in spectral shape and energy level with latitude are simply due to the properties of wave functions on a rotating sphere. The most encouraging result is the presence of prominent inertial peaks in the velocity spectra, whereas there are no such peaks in the potential energy spectra. The reason for the formation of the inertial peaks in the velocity spectra is the constructive interference of velocity wave functions near their turning latitudes; however, note that each individual wave function does not have a sharp peak near its turning latitude (see Fig. 3.2). The corresponding peak height, peak frequency, and bandwidth of the velocity spectrum at each latitude are listed in Table 4.1. The blue shift and bandwidth decrease

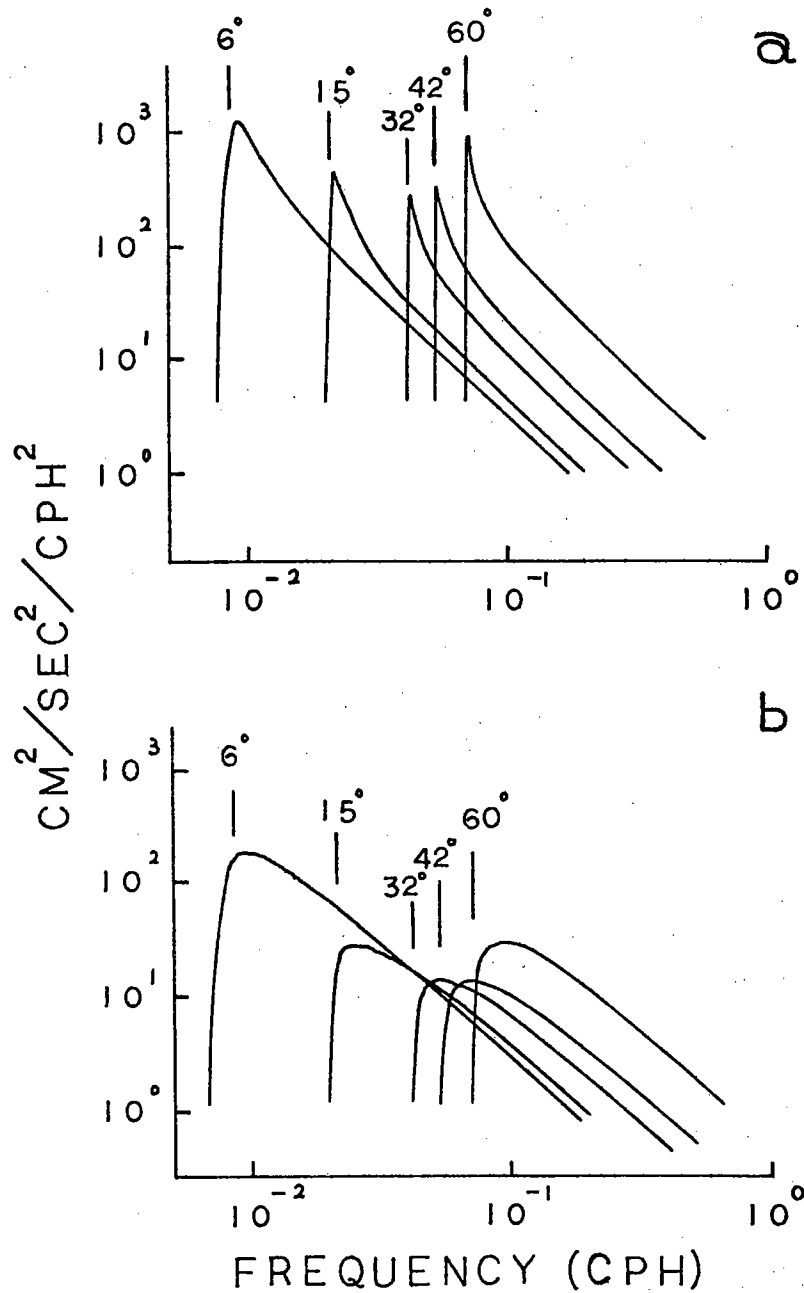


Figure 4.2 Model normalized spectra of (a) horizontal kinetic energy and (b) potential energy at five latitudes, with  $D(k, j, \omega)$  given by Model 1,  $m = 20$ ,  $j^* = 6$ ,  $t = 2.5$ , and  $E_0/N_0 = 0.03 \text{ cm}^2/\text{sec}^2/\text{cph}^2$ . The numbers are latitudes in deg.; the vertical bars indicate the locations of  $f$ .

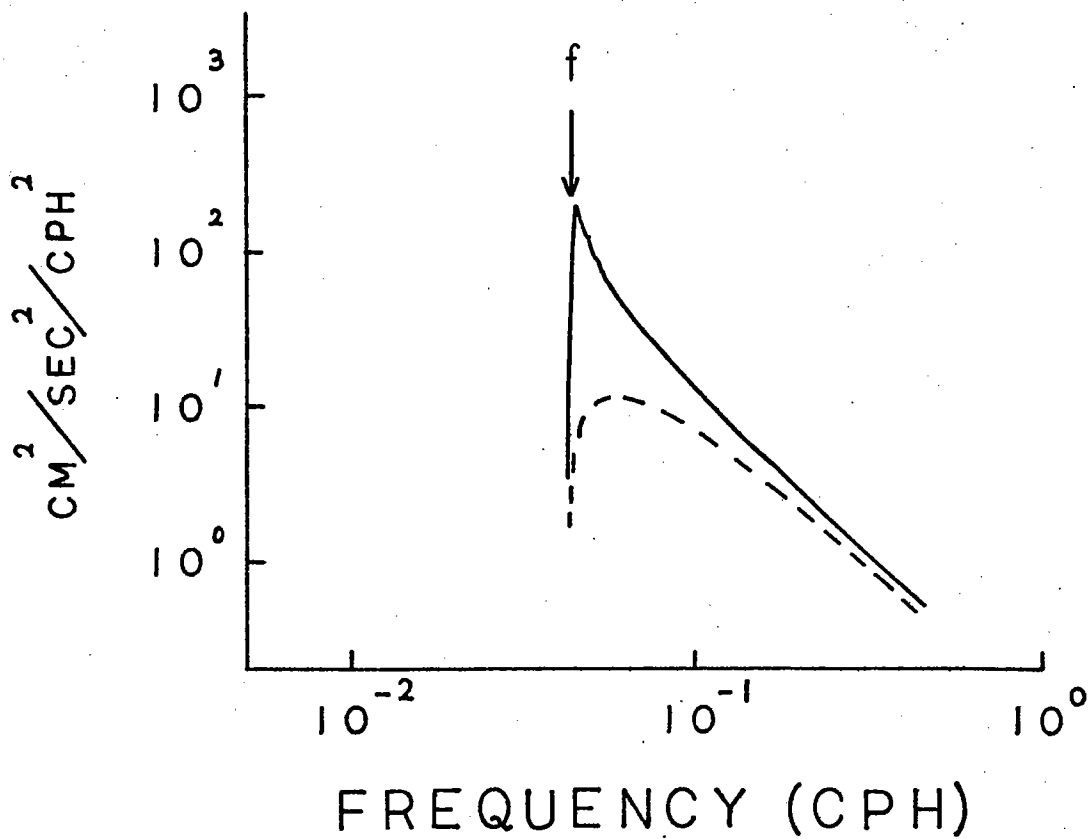


Figure 4.3 Model normalized spectra of horizontal kinetic energy (solid line) and potential energy (dashed line) at 32°, with  $D(k, j, \omega)$  given by Model 2 and the other parameters the same as in Fig. 4.2.



Table 4.1

Spectral characteristics of the model spectra shown in Fig. 4.2. Peak height is in db above the  $\omega^{-2}$  spectrum, bandwidth in percentage of f.

Latitude(deg)	$\frac{\omega_p}{f}$	Peak Height	bandwith
6	1.07	4.5	31.5 %
15	1.03	7.	14 %
31.6	1.01	7.	7 %
41.5	1.006	7.	5 %
60	1.004	6.5	3.5%

Table 4.2

Values of frequency scale  $L_\sigma$  for the 1st and 10th modes at various latitudes.

Latitude(deg)	$L_\sigma$	
	<u>j=1</u>	<u>j=10</u>
5	.376	.076
15	.086	.017
30	.033	.0067
45	.018	.0036
60	.011	.0022
75	.006	.0012

with latitude, and this can be explained as follows. As  $\phi \approx \phi_s$  and  $\sigma \approx \sin \phi$ , the argument of the Airy function in (3.27) can be approximated by (Eq.(39), MP)

$$\epsilon^{1/3} \xi = - \frac{\sigma - \sin \phi}{(\epsilon \sin 2\phi)^{-1/3} \cos \phi} + k^2 L^2 .$$

For given  $\frac{\sigma}{\sin \phi}$ , the controlling frequency scale  $L_\sigma$  is given by

$$L_\sigma = \frac{(\epsilon \sin 2\phi)^{-1/3} \cos \phi}{\sin \phi} \quad (4.19)$$

which decreases with latitude as shown in Table 4.2. After superposition of many modes,  $L_\sigma$  determines the latitudinal dependence of the blue shift and bandwidth of the resulting spectrum.

In Fig. 4.2, note that the energy level at a particular frequency increases with latitude, and this can be explained as follows: When a wave packet propagates poleward, the conservation of wave action (c.f. Bretherton and Garrett, 1969),  $A$ , defined as (wave energy)/frequency, requires that

$$\frac{\partial A}{\partial t} + \nabla \cdot (\vec{C}_g A) = 0 ,$$

or

$$\left( \frac{\partial}{\partial t} + \vec{C}_g \cdot \nabla \right) A = - A \nabla \cdot \vec{C}_g ,$$

where  $\vec{C}_g$  is the group velocity of the wave packet. Because wave rays converge with increasing latitude, from the equations above,  $A$  increases with latitude. Thus the background spectral level increases with latitude. Now we can explain why the energy level of the inertial peak

varies with latitude as shown in Fig. 4.2. Because the peak height is almost independent of latitude and the background spectrum is red, the peak energy would decrease monotonously with latitude if the background spectral level were independent of latitude. At low latitudes, the poleward increase of the background spectral level is relatively slow while the poleward increase of the inertial frequency is relatively fast, so the peak energy decreases with latitude. At high latitudes, the situation is reversed, so the peak energy begins to increase with latitude; the minimum occurs at about  $30^\circ$ .

Fig. 4.4 shows the ratio of P.E. to H.K.E. at the same five latitudes together with the curve representing

$$\frac{\text{P.E.}}{\text{H.K.E.}} = \frac{(\omega^2 - f^2)}{(\omega^2 + f^2)} \quad (4.20)$$

the result of the WKBJ approximation (Garrett and Munk, 1972). The range of the validity of the WKBJ approximation in frequency increases with latitude as described in Table 3.2. Significant deviations occur at low latitudes. The approximation is a good one down to  $1.02 f$  at mid-latitudes, where Fofonoff (1969) showed that Eq. (4.20) was consistent with observations at frequencies very close to  $f$ . The minimum ratio of P.E. to H.K.E. near  $f$  varies from 0.125 at  $6^\circ$  to 0.006 at  $60^\circ$ .

Displayed in Fig. 4.5 are the rotary spectra at  $32^\circ$ . When  $\omega \approx f$ ,  $E_+$  is finite rather than zero as would result from an  $f$ -plane model. The latitudinal dependence of  $\Gamma(\omega)$ , defined in Chapter 2 as  $\log(E_-/E_+)$ , is shown in Fig. 4.6 together with the WKBJ approximation (c.f. Eq.(2.3)). The behavior of the deviations from the WKBJ result is the same as in Fig. 4.4 as expected.

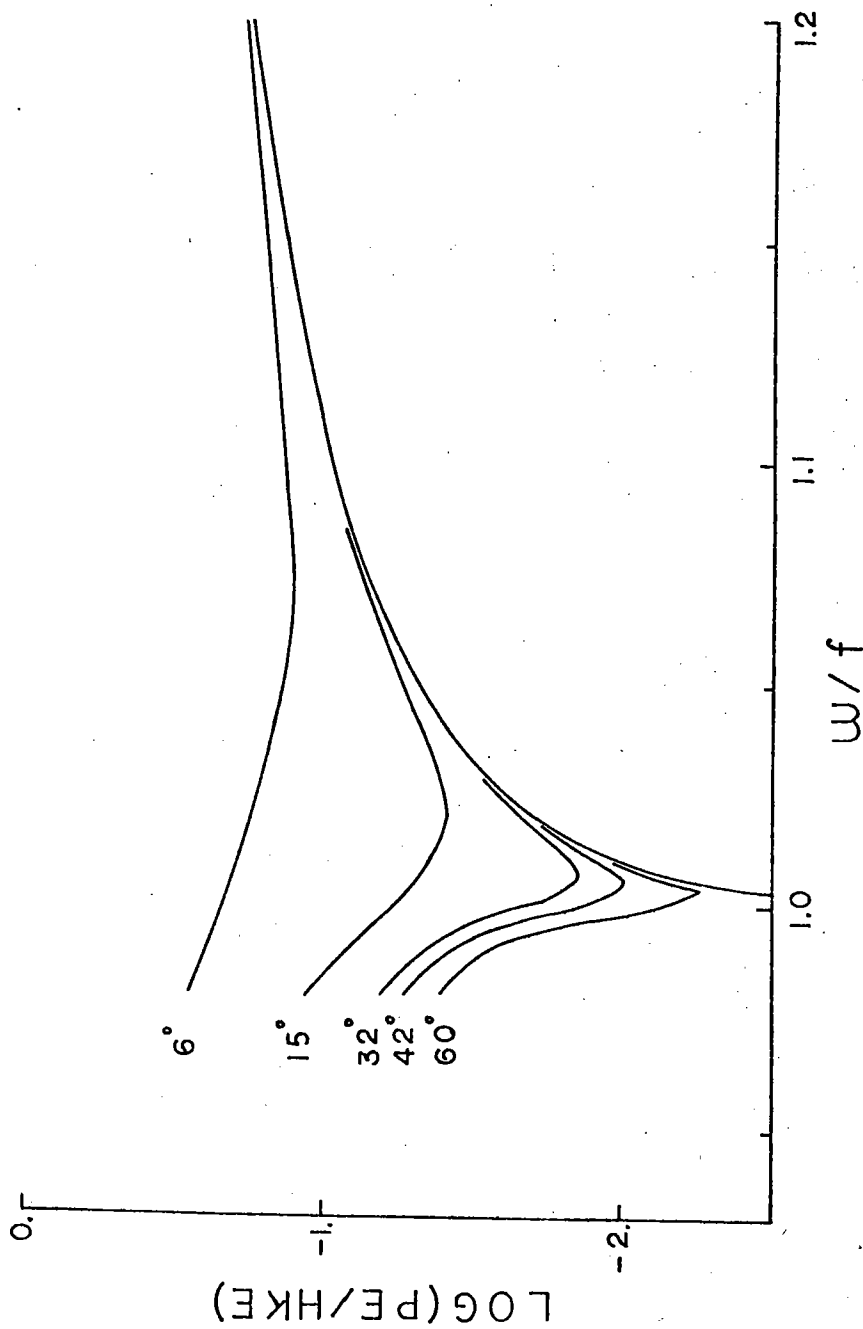


Figure 4.4 Model results of  $\text{Log}(P.E./H.K.E.)$  at the same latitudes and with the same model parameters as in Fig. 4.2. The envelope of the curves represents the WKBJ result.

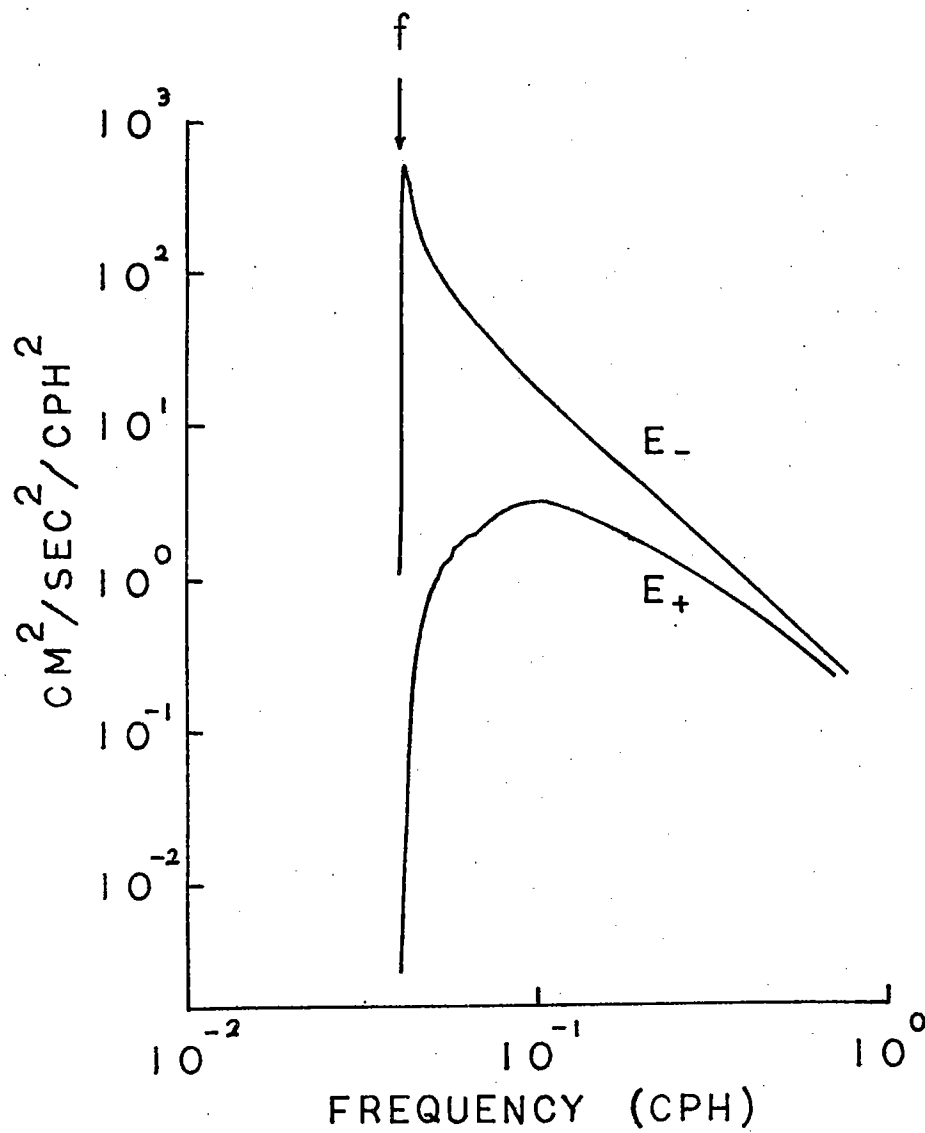
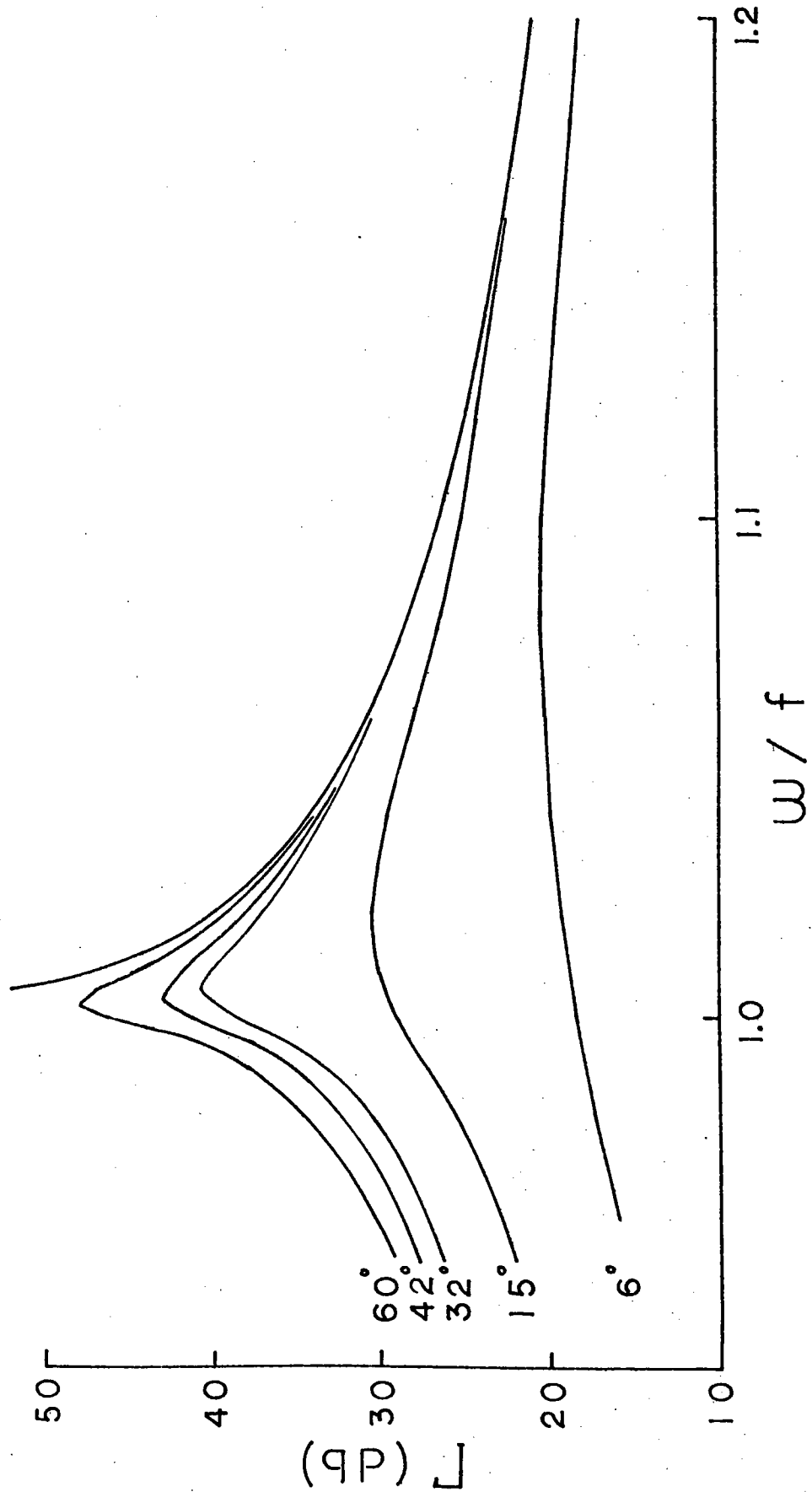


Figure 4.5 Model rotary spectra at  $32^\circ$  with the same model parameters as in Fig. 4.2

Figure 4.6 Model results of  $\log(E_-/E_+)$ , i.e.,  $\Gamma$ , at the same latitudes and with the same model parameters as in Fig. 4.2. The envelope curve is the WKBJ result.



Although the results presented above are encouraging in some respects, it remains to be seen whether they are sensitive to the parameters  $j_*$ ,  $t$ , and  $m$  in the vertical wavenumber spectrum  $A(j)$  and the special assumptions about  $D(k, j, \omega)$ .

The variation of the spectrum of H.K.E. with respect to  $j_*$ ,  $t$ , and  $m$  is shown in Figs. 4.7, 4.8, and 4.9 respectively. There are only a slight increase in peak height and a decrease in blue shift with either increasing  $j_*$  or decreasing  $t$  -- both are equivalent to increasing the "equivalent band width" as discussed by Müller et al (1978). This reflects the wavenumber dependence of the horizontal wave functions. The case with  $j_* = \infty$  corresponds to the top hat spectrum of GM72. Fig. 4.9 reveals that, for  $m > j_*$ , the results are virtually insensitive to  $m$ , the number of modes used in the calculations. Thus the results discussed in the previous section are not particularly sensitive to the model parameters.

As indicated in Fig. 3.2, the magnitude of the blue shift should be most sensitive to the zonal wavenumber content of the wave field. Because the turning latitude of a single wave decreases with increasing zonal wavenumber, one would expect an increase in the blue shift of the inertial peak if there exists a low wavenumber cutoff  $k_c$ , i.e.,  $D(k, j, \omega) = 0$  for  $|k| < k_c$ . The model spectra at  $32^\circ$  were calculated with two values of  $k_c$ : 100 (340 km wavelength) and 400 (90 km wavelength). The results are not particularly sensitive to  $k_c$  in this range. When  $k_c = 100$ , the peak frequency is essentially unchanged, i.e., 1.01 f; when  $k_c = 400$ , it increases to 1.03 f. The other characteristics of the spectra essentially remain the same.

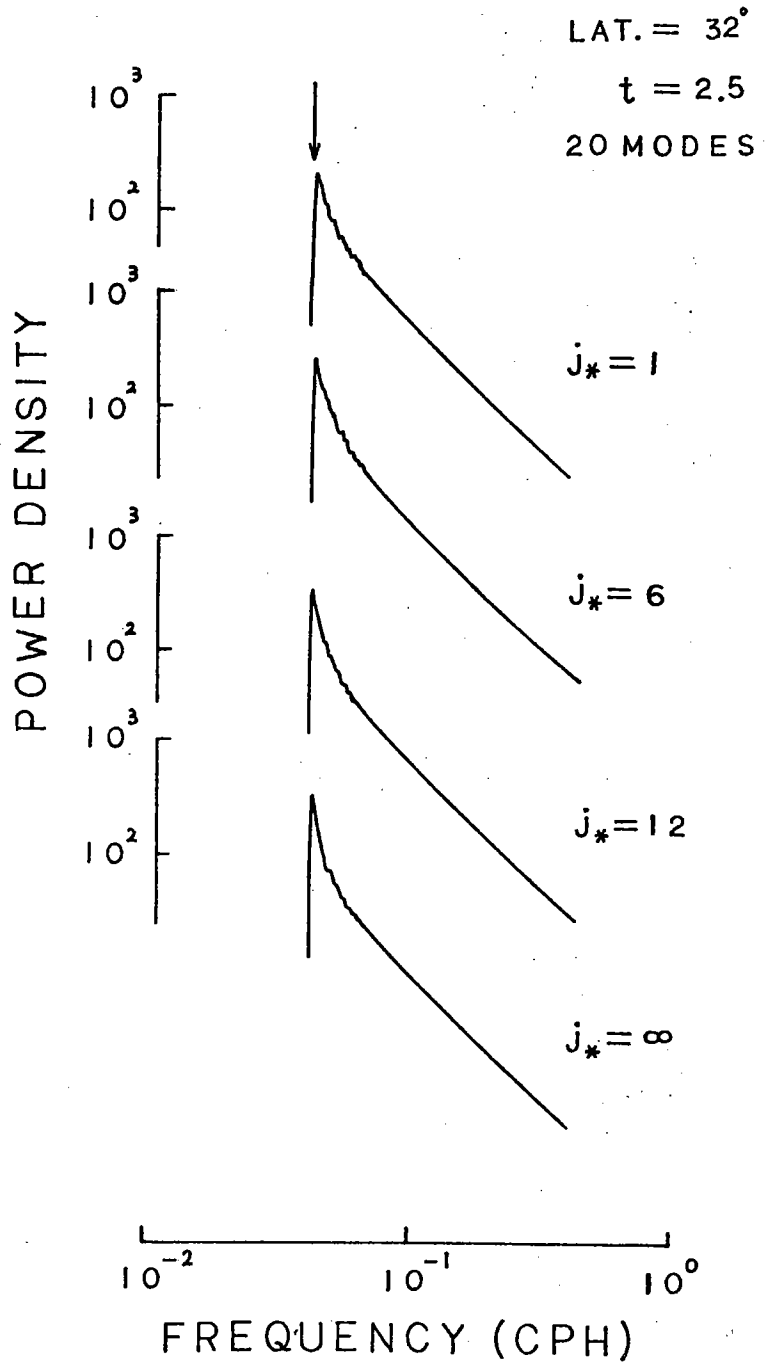


Figure 4.7 Model normalized horizontal kinetic energy spectra at  $32^\circ$  with different values of  $j_*$ . Other model parameters are the same as in Fig. 4.2. The arrow indicates the local  $f$ .



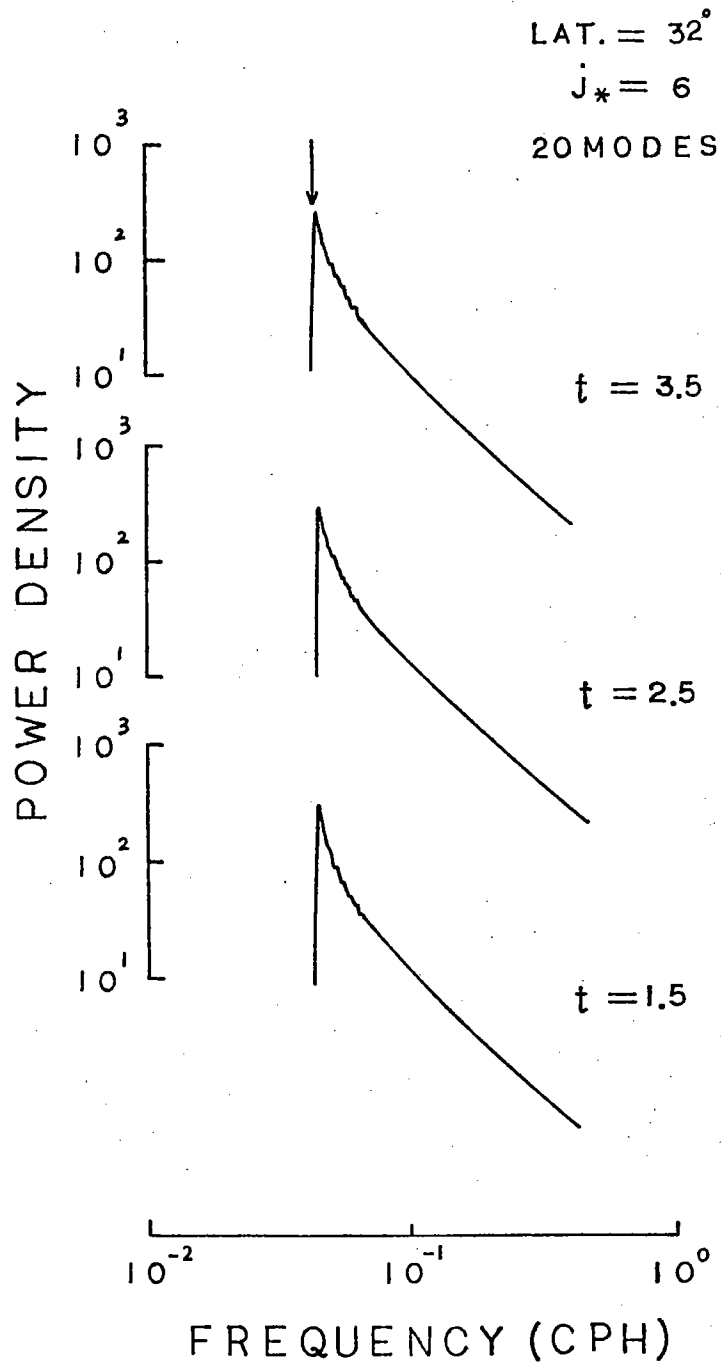


Figure 4.8 As in Fig. 4.7 except for different values of  $t$ .

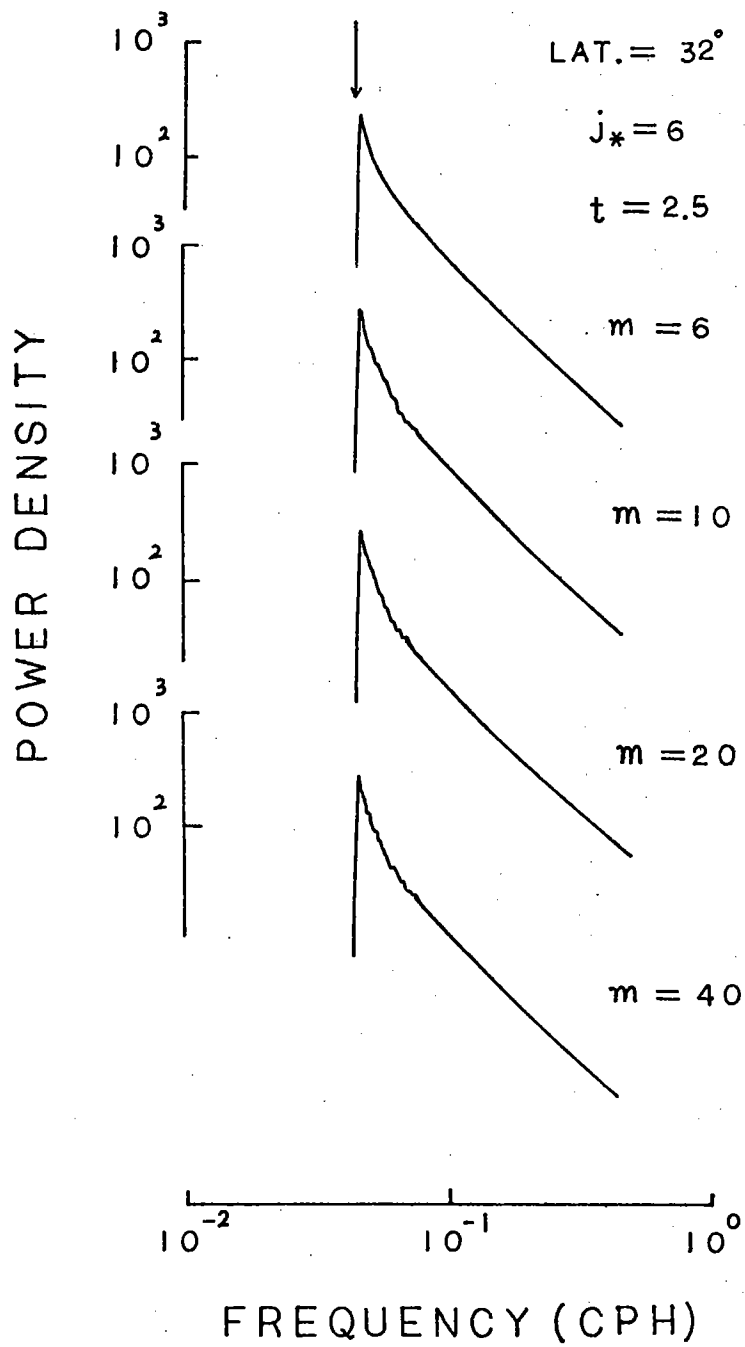


Figure 4.9 As in Fig. 4.7 except for different values of  $m$  (number of modes summed).

#### 4.4 Comparisons with observations

##### 4.4a Horizontal kinetic energy spectrum

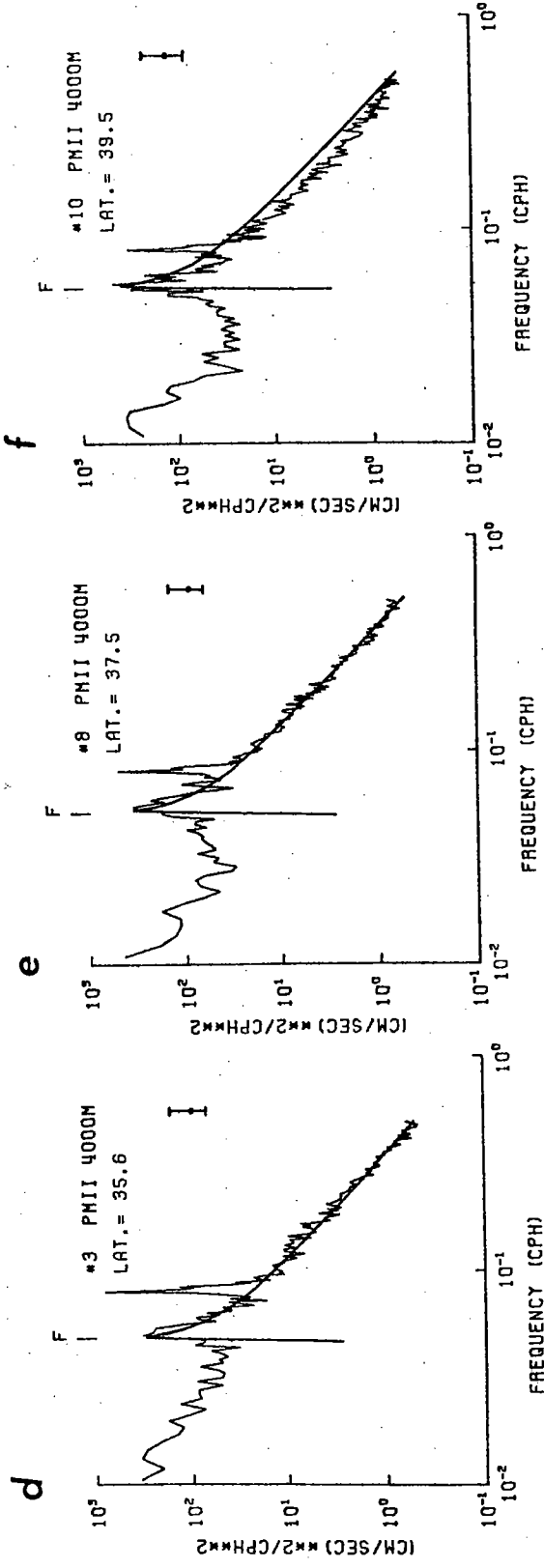
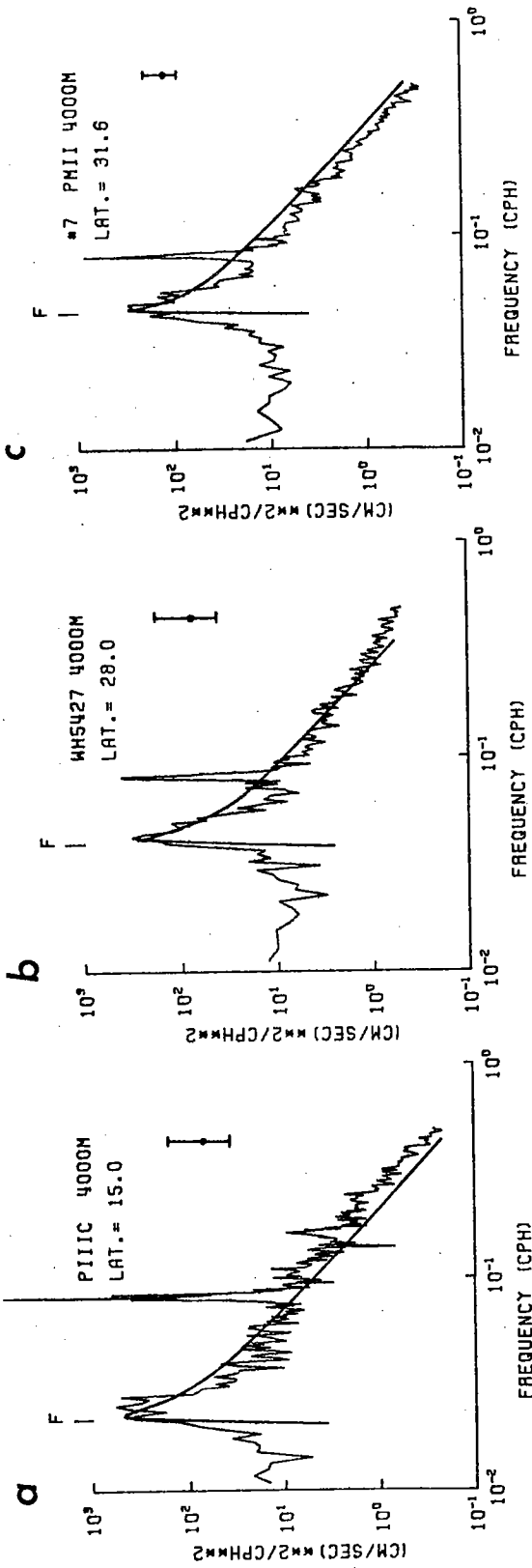
As noted in Table 4.1, the peak height of the model spectrum is of the right order to account for observations from the class 3 environment, i.e., the deep ocean over smooth topography far from strong currents, where there are no apparent local sources. With the energy level  $E_o/N_o$  as an adjustable parameter and other assumptions the same as used in Fig. 4.2, the model was fitted to the deep observations at six latitudes by requiring that the peak value of H.K.E. be equal to the observed value at each latitude. The results for  $E_o/N_o$  are listed in Table 4.3. These six records belong to class 3 except those at  $15^\circ$  and  $41.5^\circ$ , which are classified as class 2 in Chapter 2 with some ambiguity. The average of the estimates for  $E_o/N_o$  is  $0.03 \text{ cm}^2/\text{sec}^2/\text{cph}^2$  with 15 % standard deviation. Fig. 4.10 shows the

Table 4.3

Estimated values of  $E_o/N_o$  for six records at 4000 m. The latitudes and classification of the records are as indicated.

Latitude(deg)	$E_o/N_o$	Class
15	.035	2b
28	.022	3
31.6	.033	3
35.6	.0267	3
37.5	.031	3
39.5	.033	2c

Figure 4.10 Model (smooth curves) and observed normalized spectra of H.K.E. at 4000 m. Latitude, station number, and 95 % confidence error bar for each record are shown.



comparisons of the H.K.E. spectra between the model with  $E_o/N_o$  given above and the corresponding observations. The agreement is fairly good, indicating that the inertial wave field here is consistent with the global model.

The estimated value for  $E_o/N_o$  can be compared with direct equatorial observations. An "eyeball fit" of an energy spectrum of the form  $E_T \omega^{-2}$  to the observations of Eriksen (1979, Fig. 3), with the assumption of equi-partition of H.K.E. and P.E., yields  $E_T = 5.2 \times 10^{-2} \text{ cm}^2/\text{sec}^2/\text{cph}^2$ . From the relation

$$\int_{-1}^0 E_T N(z) dz = E_o$$

and the  $N(z)$  given by (3.16), we obtain

$$E_o/N_o = 0.0146 \text{ cm}^2/\text{sec}^2/\text{cph}^2,$$

which is about a factor of two less than the extrapolation from mid-latitude observations. This difference seems to be within the uncertainty of the estimation of  $N(z)$ , considering the difference in  $N(z)$  at mid-latitudes and equatorial region.

We have now obtained a reference energy level for the global wave field -- 7 db higher than the  $\omega^{-2}$  spectrum extrapolated from high frequencies, and identified the observations of class 3 with this category. The average peak height of the class 2 observations is 12 db, indicating that the energy level is about three times the value given by the model. Thus the partition of inertial wave energy of the class 2 observations is likely to be the following : one third of the total energy is due to global generation and two thirds local generation.

Assuming that all the local waves are generated at the surface and propagate downward, which is the case relevant to smooth topography areas, then the vertical wavenumber spectrum of the class 2 observations is such that 5/6 of the energy is travelling downward and 1/6 upward, because the global wave field is vertically symmetric (one half upward and one half downward) as a consequence of the underlying GM model. From a recent observation of Sanford (personal communication, 1979), about 72 % of the inertial wave energy is travelling downward, and 28 % upward; this differs from the above interpretation by about 11 % of the total energy, probably within the estimation errors.

The order of magnitude variation of energy levels with latitude at super-inertial frequencies (Fig. 4.1) seems contradictory to observations, because Wunsch and Webb (1977) reported nearly constant energy levels at 5-hour period regardless of latitude. However, Eriksen (1979) reported that near the equator, there is always a jump in energy level across the  $M_2$  tidal frequency. Thus, if the super- $M_2$  energy level is constant, the sub- $M_2$  energy level near the equator must be less than that at higher latitudes, consistent with the model. For high frequency waves, nonlinear interactions are important in determining the spectrum; for a mid-latitude model see McComas and Bretherton (1977).

As noted in Table 4.1, the blue shift predicted by the model is smaller than the observed values in the class 3 environment (generally greater than 3 % of  $f$ ). As discussed in the previous section, a low zonal wavenumber cutoff with  $k_c \gtrsim 0(400)$  is therefore required to account for the observed magnitude of the blue shift. Because the spectral shape is not affected by the value of  $k_c$ , we can freely

adjust  $k_c$  to fit the observed blue shift for each individual record. However, such a "tuning" was not attempted in Fig. 4.10.

The decrease of the bandwidth with latitude as indicated in Table 4.1 is consistent with observations (see Table 2.4). The predicted values of the bandwidth are generally less than the observed values; however, the differences are probably not significant, i.e., not substantially greater than the frequency resolution limit. On the other hand, the presence of a low frequency current can cause the broadening of the inertial peak through two mechanisms. Firstly, a uniform mean current could cause a Doppler shift of the inertial frequency (White, 1972). For example, a uniform current of 10 cm/sec would result in a Doppler shift with magnitude of 8 % of  $f$  at  $30^\circ$ , provided that the wavelength of the inertial waves is 100 km. Secondly, Fomin (1973) and Mooers (1975) have shown that a horizontal shear can cause an "effective inertial frequency" defined as

$$f_e = (f(f + \zeta))^{1/2},$$

where  $\zeta$  is the vertical component of the relative vorticity of the mean current. For a relatively strong eddy with  $\left|\frac{\zeta}{f}\right| \sim 0.05$ , we have  $|f_e - f| = 0.025f$ . This effect has been observed at Site D by Perkins (1976). The result of these two mechanisms is to broaden the observed inertial bandwidth in long-term measurements by an amount of the order of 10 % of  $f$ , which is large enough to account for the difference between observations and the model results.

In summary, by assuming a low zonal wavenumber cutoff with



$k_c \geq 400$  (1/90 cycle/km) in the Model 1 for  $D(k, j, \omega)$ , the H.K.E. of the class 3 observations can be well-described by the model in terms of both the peak height and blue shift. The slight difference between observed and calculated bandwidth can be attributed to the kinematic effects of mean flow on inertial waves.

#### 4.4b Potential energy spectrum

When multiplied by  $\frac{1}{2} \left( \frac{d\rho}{dT} \right)^2 \frac{g^2}{\rho_0^2 N^2}$ , observed temperature spectra can be converted to P.E. spectra and compared with the model. Fig. 4.11 shows the results at the same latitudes. Here the model cannot account for the observed apparent inertial peaks. As mentioned earlier, temperature signals in the inertial band are subject to contaminations (see Appendix A), and the inconsistency between the observed H.K.E. and P.E. near  $f$  is not unexpected. Using the measurements of isotherm depth from a mid-water float, Cairns and Williams (1976) reported a vertical displacement spectrum without inertial peaks similar to the model.

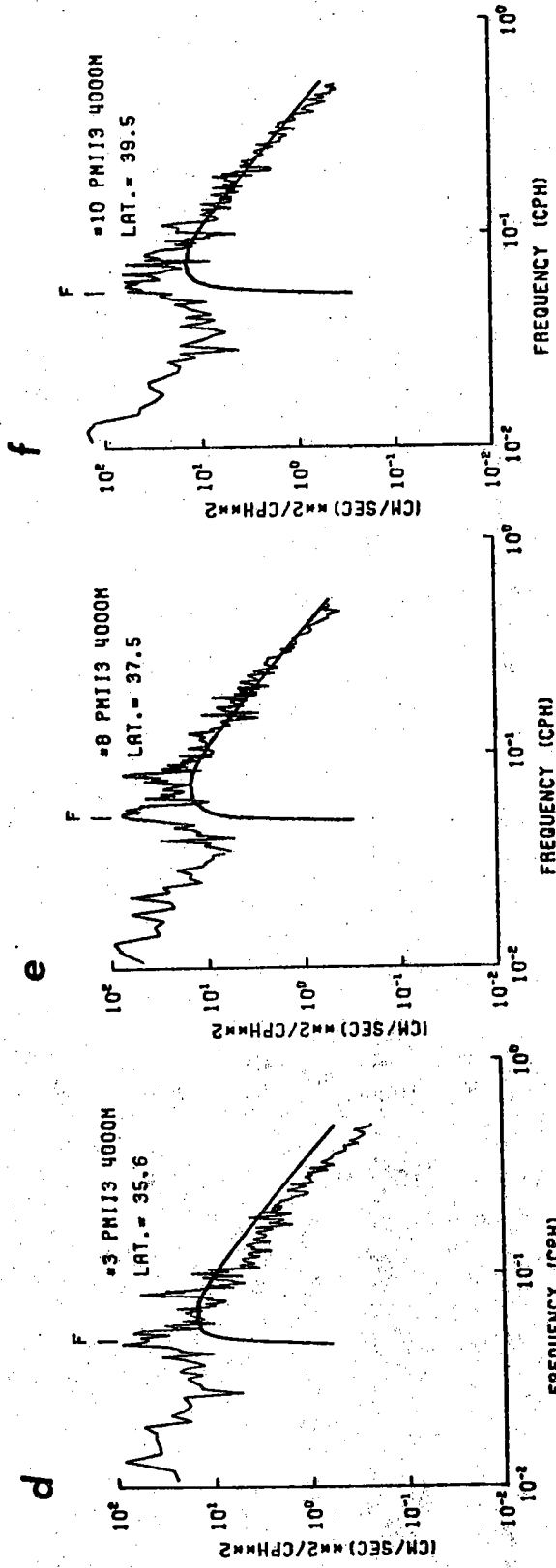
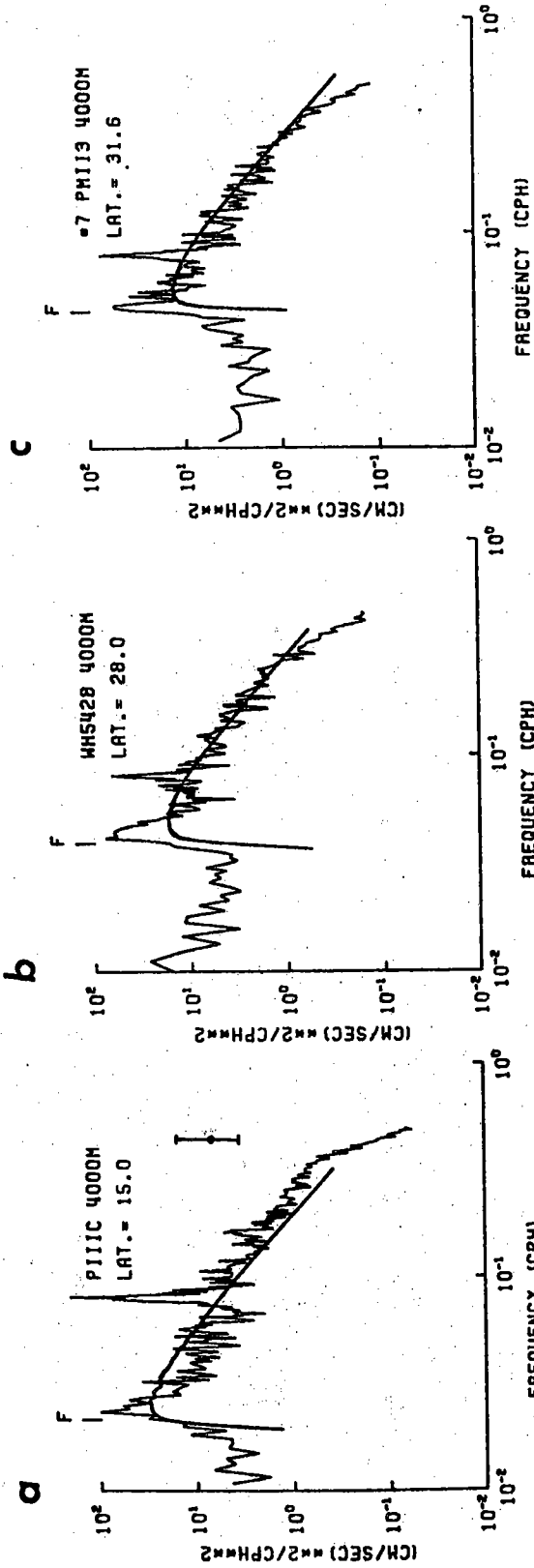
#### 4.4c Rotary spectrum

Although the counter-clockwise energy level  $E_+$  at the inertial frequency predicted by the model is finite rather than zero (see Fig. 4.5), it is still much smaller than the observed values (see Fig. 2.8). At mid-latitudes the calculated  $\Gamma(f)$  is about 40 db, as compared to 15 db in the observed class 3 spectra (c.f. Fig. 2.9). This implies that there is an excess of counter-clockwise energy which must be accounted for by other mechanisms; local energy cascade from low frequency motions is a possible candidate (see Section 2.3d).

#### 4.5 Latitudinal limits of the model

Because the poles are singular points of Eq. (3.20), a special

Figure 4.11 As in Fig. 4.10 except for potential energy. 95 % confidence error bar is the same for each record.



expansion is needed to obtain valid wave functions there. Consequently, the model discussed above breaks down when  $\phi \approx \pm 90^\circ$ . But how close to  $\pm 90^\circ$  is the model formally valid? The validity of the Airy solution represented by (3.27) depends on the implicit assumption that  $|\phi_s| < 90^\circ$ , i.e., there must be a turning latitude between  $0^\circ$  and  $90^\circ$ . For  $\sigma > 1$ , there is no turning latitude; the Airy solution is not applicable. However, at latitudes far from  $\pm 90^\circ$ , the Airy solutions can be replaced by the WKBJ solutions when  $\sigma \geq 1$  because  $\sigma_c$  there is well below unity (see 3.4); hence the model is valid at all frequencies. Thus the poleward limits of  $\phi$  for the validity of the model are the latitudes where  $\sigma_c = 1$ . From (3.32), these are approximately  $\pm 68^\circ$ .

On the other hand, when  $\phi \approx 0^\circ$ , the latitudinal equatorial modes for low frequency waves are likely to be established (Matsuno, 1966), and the continuous wavenumber spectrum underlying the model is irrelevant. The question about where the transition from the one turning point problem to the two turning point problem occurs is not easy to answer. Presumably for each vertical mode  $m$ , there exists a maximum latitudinal mode number  $n_{\max}$  such that no equatorial modes exist with mode number  $n > n_{\max}$ . Then the turning latitude of mode  $n_{\max}$  is the transition latitude in question for the particular vertical mode  $m$ . Hence the answer is dependent on the wavenumber spectrum. Because the first vertical mode is usually the most energetic one, we proceed to discuss, based on  $m = 1$ , some possible implications from equatorial wave dynamics and observations.

Near the equator, Eq. (3.23) can be approximated by

$$l^2 = \epsilon_m (\sigma^2 - \phi^2) - \frac{k}{\sigma} - k^2 \quad (4.21)$$

The condition for the establishment of equatorial modes requires (Matsuno, 1966)

$$\sigma^2 \epsilon_m - \frac{k}{\sigma} - k^2 = \epsilon_m^{1/2} (2n+1) \quad , \quad (4.22)$$

where  $n = 0, 1, 2, \dots$ . Then the turning latitude  $\phi_{sn}$  for mode  $n$  is

$$\phi_{sn} = \epsilon_m^{-1/4} (2n+1)^{1/2} \quad . \quad (4.23)$$

We do not have a theory to determine  $n_{\max}$ ; presumably it depends on the dissipation and the time  $T$  which is required to establish the mode. With the latitudinal group velocity denoted by  $c_g$ ,  $T$  can be written

$$T = 2 \int_{-\phi_{sn}}^{\phi_{sn}} \frac{d\phi}{c_g} \quad , \quad (4.24)$$

the time it takes a wave packet to make a complete excursion in the wave guide. From (4.21) and (4.22) we have

$$c_g = \frac{\partial \sigma}{\partial l} = \frac{2 [\epsilon_m^{1/2} (2n+1) - \epsilon_m \phi^2]^{1/2}}{2\sigma \epsilon_m + \frac{k}{\sigma^2}} \quad (4.25)$$

For simplicity, we assume that  $k = 0$  in (4.25) and obtain

$$\begin{aligned} C_g &= (\sigma \epsilon_m^{1/2})^{-1} \left[ \epsilon_m^{-1/2} (2n+1) - \phi^2 \right]^{1/2} \\ &= (\sigma \epsilon_m^{1/2})^{-1} (\sigma^2 - \phi^2)^{1/2} \end{aligned} \quad (4.26)$$

Substituting (4.26) into (4.24), we have

$$T = \pi \epsilon_m^{1/4} (2n+1)^{1/2} \quad (4.27)$$

The values of  $\epsilon_m$  are related to  $c_m$ , the gravity wave phase speed for vertical mode  $m$ , as follows:

$$\epsilon_m = \frac{4\Omega^2 R^2}{c_m^2}$$

With  $c_1 = 2.6$  m/sec as used by Wunsch and Gill (1976), we have  $\epsilon_1 = 1.27 \times 10^5$ . The values of  $\phi_{sn}$  and  $T$  for  $m = 1$  and some selected  $n$ 's are tabulated in Table 4.4. The increase of  $T$  with  $n$  implies that higher modes are more difficult to set up as we expected. Wunsch and Gill (1976) showed clear evidence for the existence of equatorial modes up to  $n = 4$  in the Pacific; Considering the increase of  $T$  with  $n$ , the value of  $n_{\max}$  is likely  $O(5)$  and the transition occurs at  $O(10^\circ)$ . For higher vertical modes,  $T$  increases and  $\phi_{sn}$  decreases;  $10^\circ$  is probably an upper bound for the relevance of a two turning point model.

Using discrete modal solutions on an equatorial beta plane, Eriksen (1979) developed a model spectrum for equatorially trapped waves. He found that there were no apparent inertial peaks at  $\phi \approx 0^\circ$ , and that a weak peak first showed up at about  $3^\circ$  with the blue shift equal

Table 4.4

Tabulation of  $\phi_{sn}$  and T of the 1st baroclinic mode equatorially trapped gravity waves for selected meridional mode numbers n. Parenthetical values of T are in wave periods.

n	$\phi_{sn}$ (deg.)	T(days)	
1	5.3°	103	(19)
2	6.8°	133	(31)
3	8.0°	157	(44)
4	9.1°	178	(57)
5	10.°	197	(69)
6	11.°	214	(82)
10	14.°	272	(132)

to 23 % of f. At 6° the blue shift predicted by his model is 18 % as compared to 7 % by our model; hence the amount of the blue shift is a good parameter to distinguish these two models. The observation at 7° N quoted by Eriksen (1979) showed a 10 % blue shift, which lies between the predictions of these two models, implying only part of the wave field (presumably the low vertical modes) has equatorial modal structure. This supports the speculation that 10° is an upper bound for the existence of equatorial gravity modes.

#### 4.6 Summary and discussion

A model spectrum for the global inertial waves randomly forced at

lower latitudes has been developed. The model results vary with latitude. In general, there is a peak a few percent above  $f$  in the horizontal kinetic energy spectrum, with peak height a few decibels above the extrapolation of the spectrum at high frequencies; there is no distinct peak in the corresponding potential energy spectrum whose shape is very similar to the result of the GM model. The normalized energy level at the inertial frequency has its minimum at mid-latitudes (approximately  $30^\circ$ ) with variation less than one order of magnitude; the normalized energy level at super-inertial frequencies increases with latitude monotonously, yielding a difference greater than one order of magnitude between low and high latitudes. The general model results are not particularly sensitive to the model configuration and parameters. However, the assumption of a low zonal wavenumber cutoff slightly increases the blue shift.

Except at very low latitudes (less than  $10^\circ$ ), the peak height of the H.K.E. spectra is about 7 decibels and accounts for the observations in the deep ocean over smooth topography far from strong currents (class 3). With the difference between the model results and the upper ocean observations (class 2a) attributed to a downward propagating local wave field, we have estimated an energy budget in terms of upward and downward travelling wave energy; the result is fairly consistent with recent observations. A forced model is proposed in Chapter 5 to describe this local wave field.

The model predicts a slight decrease in both the bandwidth and blue shift with latitude, which is consistent with observations. In order to produce the observed magnitude of the blue shift, a low zonal wavenumber



cutoff of 1/90 cycle/km is required, i.e., the wavelength is required to be less than 90 km. The frequency bandwidth predicted by the model is slightly less than what is observed, but this difference can be accounted for by the kinematic effects of low frequency motions.

The latitudinal range of the validity of the model is roughly from  $10^{\circ}$  to  $68^{\circ}$ .

## Chapter 5 A Forced Model for the Local Inertial Wave Field

### 5.1 Introduction

The purpose of this chapter is to study the oceanic response to a localized forcing mechanism in the inertial frequency band. As the details of the forcing spectrum near  $f$  are essentially unknown, we consider an idealized model which is as simple as possible. Our focus is on the following question : Can we show qualitatively that the observed spectral characteristics which cannot be described by the global model, are the results of local forcing ? Quantitative results in this chapter are only suggestive, not conclusive.

The forcing is imposed through boundary conditions of the vertical velocity field  $w_b$  at the base (or top) of the surface (or bottom) mixed layer. In the surface layer  $w_b$  could be produced by either the convergence and divergence of inertial currents in the mixed layer, or the advection of its large scale corrugations by mean surface currents. In the bottom layer  $w_b$  could be produced as a result of the interaction between low frequency eddies and rough topography. But the details of the boundary layer dynamics will not be pursued here.

At any particular latitude  $\phi_0$ , we consider the response only in a narrow frequency band around the local  $f$ , in which the forcing spectrum can be simply modeled as white noise. Furthermore, we assume that the corresponding spatial structure is localized and not varying with frequency. The assumption of localness does not imply that remote forcing with frequencies in this particular range does not exist, but that it has been already accounted for by the global model.

In order to describe the transition of wave functions from evanescent when  $\omega < f$  to oscillatory when  $\omega > f$ , as noted in Chapter 1, the variation of  $f$  with latitude must be taken into account in the governing equations. The simplest approximation of this kind is the equatorial beta plane approximation with  $f = \beta y$ ; however, this approximation is not strictly valid for the problem of mid-latitude inertial waves (see Lindzen, 1967). With  $f = f_0 + \beta y$  at mid-latitudes, the resulting equation is the Weber equation whose solutions are not particularly easy to handle. The recent developments in asymptotic solutions of the LTE (e.g., Kamenkovich and Tsybaneva, 1975 a, b) have provided a feasible way to deal with the LTE directly. With proper boundary conditions, the eigensolutions of the LTE form a complete set (Longuet-Higgins, 1968) which can be used to expand the latitudinal structure of the forcing function. Then the problem remaining is to solve the vertical equation for each latitudinal mode subject to specific boundary conditions. At the forced boundary, the vertical velocity is given, but the other boundary condition needs some arguments. Should we let the waves reflect from the vertical boundaries with the possibility that they form normal modes with the incident waves? The answer depends on the travel time to take a wave packet through a vertical round trip in the ocean. In Kroll's model (1975) of the ray paths of internal waves on a beta plane, it was implied that the travel time was of the order of 60 days for those rays which had encountered their turning points, and of the order of 10 days for those which had not. Because the travel time is longer than the time scale of the forcing (usually less than a week), it seems appropriate to neglect the

reflected waves. This conclusion also can be reached by considering the nearly horizontal propagation of the rays when  $\omega \approx f$ . With the mid-latitude beta plane approximation, the equation for the amplitude of the velocity  $v$ , which is proportional to  $\exp(i(k\lambda - \omega t))$  can be written as (c.f. Philander, 1978)

$$V_{yy} - (k^2 + \beta \frac{k}{\omega}) V + (f^2 - \omega^2) \frac{\partial}{\partial z} \left( \frac{1}{N^2} \frac{\partial V}{\partial z} \right) = 0 \quad (5.1)$$

where  $f = f_0 + \beta y$ ,  $\beta = \frac{df}{dy}$ , and  $y = R\phi$ . If, for simplicity, we assume  $k = 0$ , the ray paths lie in the  $y$ - $z$  plane and can be represented by

$$\pm \int_0^z N(z) dz = \frac{1}{\beta} \int_{f_0}^{f(y)} (\omega^2 - f^2)^{1/2} df \quad (5.2)$$

Then for a surface-generated wave packet reflecting back to the surface, the latitudinal distance it travels,  $d$ , can be estimated by repeated uses of (5.2). For  $H = 5$  km, and  $\phi_0 = 30^\circ$ , we obtain  $d \approx 500$  km. If the latitudinal scale of the forcing is less than 500 km, the reflected waves will be out of the forced region and can then be neglected in the local dynamics. Based on these two considerations, it seems justified in a local model to assume that the ocean is infinitely deep and that the waves never reflect; hence we should use appropriate radiation boundary conditions whenever they are relevant. So the model configuration is basically the same as that used by Wunsch (1977) in his study of the

equatorial Indian Ocean. But where does the energy go ? Presumably part of it is lost through friction and/or redistributed through nonlinear interactions; the remaining energy will eventually become, through "remote reflections," part of the internal wave field equatorward of the forced region.

In order to put this model into its proper perspective, we briefly review some previous models with emphasis on their differences from this one. The purpose of the model of Pollard (1970) was to study the oceanic response to a wind event of finite duration as an initial value problem. It was an f-plane model with vertical modal decomposition and its focus was on the amplitudes and structures of wind forced inertial waves. The model of Hendershott (1973), on the other hand, studied the response to periodic forcing with the diurnal tidal frequency; its focus was on the response at this particular frequency as a function of latitude. The procedure for obtaining a solution is similar to that used in our model, but it involved vertical modes rather than propagating waves, and the beta plane equations rather than the LTE. The model of Kroll (1975) was used to study the propagation of inertial waves from the surface mixed layer to the deep ocean based on ray theory; its focus was on the ray paths at a particular frequency near  $f$  and the variation of amplitude along them. For the ray solutions, however, it is generally difficult to obtain their Eulerian representations which can most easily be compared with field observations. Furthermore, the response at sub-inertial frequencies cannot be adequately described.

The organization of this chapter is as follows : Section 5.2 describes the formulation of the model and methods of solution; Section

5.3 presents an asymptotic expansion procedure for the LTE in the parameter regime of inertial waves; Section 5.4 presents the model results; Section 5.5 is a summary.

### 5.2 The model and methods of solution

At a particular position  $(\lambda_0, \phi_0)$ , the local forcing generally can be represented as a Fourier integral in frequency space as follows:

$$w_b(\lambda, \phi, t) = \frac{1}{\sqrt{2\pi}} \operatorname{Real} \int_{-\infty}^{\infty} \hat{w}_b(\lambda, \phi, \sigma) \exp(-i\sigma t) d\sigma, \quad (5.3)$$

$$\text{with } \hat{w}_b = \frac{s(\lambda, \phi)}{(2|\sigma_2 - \sigma_1|)^{1/2}} \quad \text{for } \sigma_2 > |\sigma| > \sigma_1 > 0 \quad (5.4)$$

$$= 0 \quad \text{otherwise,}$$

where  $\sigma_2 > \frac{f_0}{2\Omega} > \sigma_1$ , and  $f_0 = 2\Omega \sin \phi_0$ . Thus the forcing energy is evenly distributed in a narrow frequency band centered on  $\pm f_0$ , and  $|s(\lambda, \phi)|$  represents the spatial distribution of its root mean square amplitude. In particular, we consider  $s(\lambda, \phi)$  of the following form:

$$S(\lambda, \phi) = S_0 \exp \left[ i k_0 (\lambda - \lambda_0) - \frac{(\phi - \phi_0)^2 R^2}{L^2} \right], \quad (5.5a)$$

$$\text{where } k_0 = \frac{R \cos \phi_0}{L} \quad (5.5b)$$

and  $L$  is a length scale. Eqs. (5.5a) and (5.5b) represent a disturbance

of which the latitudinal dependence is a Gaussian distribution centered at  $\phi_0$  with scale  $L$ , and the zonal dependence is sinusoidal with dimensional wavenumber equal to  $1/L$ . With  $s(\lambda, \phi)$  given by (5.5a) and (5.5b), Eq. (5.3) represents a group of zonally propagating waves whose amplitudes are localized in latitude with scales comparable to their zonal wavelengths. This is the simplest model for a latitudinally localized forcing.

Now the solutions of all the field variables can be written as

$$\begin{pmatrix} u(\lambda, \phi, z, t) \\ v(\lambda, \phi, z, t) \\ w(\lambda, \phi, z, t) \\ p(\lambda, \phi, z, t) \\ \beta(\lambda, \phi, z, t) \end{pmatrix} = \frac{1}{\sqrt{2\pi}} \text{Real} \int_{-\infty}^{\infty} d\sigma \begin{pmatrix} \hat{u}(\phi, z, \sigma) \\ \hat{v}(\phi, z, \sigma) \\ \hat{w}(\phi, z, \sigma) \\ \hat{p}(\phi, z, \sigma) \\ \hat{\beta}(\phi, z, \sigma) \end{pmatrix} \exp[i(k_0 \lambda - \sigma t)] \quad (5.6)$$

with  $\hat{w}(\phi, z, \sigma) = \hat{w}_b$  at the forced boundary and proper radiation conditions at the other. Following Eq. (3.8),  $\hat{w}(\phi, z, \sigma)$  generally can be written as the sum of an infinite series of functions separable in  $z$  and  $\phi$  as follows:

$$\hat{w}(\phi, z, \sigma) = \sum_{n=1}^{\infty} -i W_{n,\sigma}(z) P_{n,\sigma}(\phi) \quad (5.7)$$

Each term in (5.7), when multiplied by  $\exp(i(k_0 \lambda - \sigma t))$ , is a solution to Eqs. (3.2)-(3.6) with terms involving  $2\Omega \cos \phi$  neglected. Similarly,  $\hat{v}(\phi, z, \sigma)$  and  $\hat{p}(\phi, z, \sigma)$  can be written

$$\hat{V}(\phi, z, \sigma) = \frac{i}{\cos \phi} \sum_{n=1}^{\infty} F_{n,\sigma}(z) V_{n,\sigma}(\phi), \quad (5.8)$$

$$\hat{P}(\phi, z, \sigma) = 2\Omega R \sum_{n=1}^{\infty} F_{n,\sigma}(z) P_{n,\sigma}(\phi). \quad (5.9)$$

### The latitudinal problem

The equation for  $P_{n,\sigma}$  can be obtained by eliminating  $V$  from (3.18) and (3.19), yielding the conventional form of the LTE in terms of pressure:

$$(1-\nu^2) \frac{d^2 P_{n,\sigma}}{d\nu^2} + 2\nu \frac{1-\sigma^2}{\sigma^2-\nu^2} \frac{dP_{n,\sigma}}{d\nu} + \left[ \epsilon_{n,\sigma}(\sigma^2-\nu^2) - \frac{k_0^2}{1-\nu^2} - \frac{k_0}{\sigma} \frac{\nu^2+\sigma^2}{\nu^2-\sigma^2} \right] P_{n,\sigma} = 0 \quad (5.10)$$

where  $\nu = \sin \phi$ . With appropriate homogeneous boundary conditions imposed at the latitudinal boundaries,  $\pm \phi_b$ ,  $\epsilon_{n,\sigma}$  is the eigenvalue for the  $n$ th eigensolution  $P_{n,\sigma}$ . Eq. (5.10) then poses a Sturm-Liouville problem. For given  $\sigma$  and  $k_0$ , we have the following orthogonality condition

$$\int_{-\phi_b}^{\phi_b} P_{n,\sigma}(\phi) P_{m,\sigma}(\phi) d\phi = \delta_{m,n} \quad (5.11)$$

Moreover,  $P_{n,\sigma}$ 's form a complete set in  $[-\phi_b, \phi_b]$  (Longuet-Higgins, 1968).

From Eq. (3.18),  $V_{n,\sigma}(\phi)$  can be obtained as

$$V_{n,\sigma} = \frac{\sigma}{\nu^2-\sigma^2} \left[ (1-\nu^2) \frac{dP_{n,\sigma}}{d\nu} + \frac{k_0\nu}{\sigma} P_{n,\sigma} \right] \quad (5.12)$$



The boundary conditions and corresponding eigensolutions of Eqs. (5.10) and (5.12) are discussed in Section 5.3.

### The vertical problem

The vertical equation for  $W_{n,\sigma}(z)$  is the same as (3.14) with  $\epsilon$  replaced by the eigenvalue  $\epsilon_{n,\sigma}$ :

$$\frac{d^2 W_{n,\sigma}(z)}{dz^2} + \epsilon_{n,\sigma} S^2 \tilde{N}(z) W_{n,\sigma}(z) = 0 \quad (5.13)$$

The boundary condition at the forced boundary can be written

$$\sum_{n=1}^{\infty} -i W_{n,\sigma}(z_b) P_{n,\sigma}(\phi) = \hat{w}_b(\phi), \quad (5.14)$$

where  $z_b = 0$  for surface forcing,  
 $z_b = -1$  for bottom forcing.

Multiplying both sides of (5.14) by  $P_{m,\sigma}(\phi)$  and integrating from  $-\phi_b$  to  $\phi_b$ , with the use of (5.11) we obtain

$$W_{n,\sigma}(z_b) = i a_{n,\sigma}, \quad (5.15)$$

where 
$$a_{n,\sigma} = \int_{-\phi_b}^{\phi_b} P_{n,\sigma}(\phi) \hat{w}_b(\phi) d\phi \quad (5.16)$$

From Eq. (3.12) we can obtain  $F_{n,\sigma}(z)$  from  $W_{n,\sigma}(z)$  as follows:

$$F_{n,\sigma}(z) = \frac{R}{\epsilon H \sigma} \frac{d W_{n,\sigma}}{dz} \quad (5.17)$$

Before proceeding to solve the vertical equations, we should choose a suitable  $N(z)$ . With surface sources, using an exponential  $N(z)$  Wunsch (1977) encountered two problems : Firstly, Wunsch (1977) has pointed out that, as  $z \rightarrow -\infty$ ,  $N(z)$  eventually becomes smaller than any given frequency  $\sigma$  and waves reflect even in an infinitely deep ocean. Secondly, D. Moore and J. McCreary (personal communication via C. Wunsch) have recently pointed out that the solutions obtained by Wunsch (1977) in terms of Hankel functions are erroneous because the argument of the Hankel functions in his problem is small in the far-field ( $z \rightarrow -\infty$ ) where the radiation condition should be applied, and the asymptotic behavior (upward phase propagation to produce downward energy propagation) invoked is not correct. Both problems can be resolved, however, by assuming the following form of  $\tilde{N}(z)$  :

$$\tilde{N}(z) = N_b/N_0 + \exp(zH/b) \quad (5.18)$$

where  $N_b$  is a constant representing a nearly uniform stratification as  $z \rightarrow -\infty$ . If the value of  $N_b$  is chosen to be at least several times greater than  $f$  (usually the case in the deep ocean), inertial waves would not reflect and the WKB solutions are valid as  $z \rightarrow -\infty$ . Hence the appropriate solutions are those with upward phase propagation, as the consequence of requiring downward energy propagation. The parameter  $H$ , defined as the ocean depth before, is an arbitrary scale for  $z$  now, because we have assumed that the ocean is infinitely deep. However, for the problem of bottom forcing, we will assume that the source is located at  $z = -1$  (or  $z^* = -H$ ), and let the ocean extend to  $z \rightarrow +\infty$ .

With  $\tilde{N}(z)$  given by (5.18) and boundary condition given by (5.15), the WKBJ solutions can be readily obtained from Eq. (3.17). Defining

$$\gamma = \frac{S'_b}{H} |\epsilon|^{1/2} \quad (5.19)$$

and

$$\theta(z) = \frac{N_b}{N_0} (z+1) S' |\epsilon|^{1/2} + \gamma (e^{zH/b} - e^{-H/b}), \quad (5.20)$$

the results for both surface and bottom forcing are written as follows :

Surface forcing

(i)  $\epsilon_{n,\sigma} > 0$

$$W_{n,\sigma}(z) = A_{n,\sigma} \tilde{N}(z)^{-1/2} \exp[i\theta(z)] \quad (5.21)$$

$$F_{n,\sigma}(z) = \frac{i N_0}{2\Omega \sigma} |\epsilon_{n,\sigma}|^{-1/2} A_{n,\sigma} \tilde{N}(z)^{1/2} \exp[i\theta(z)], \quad (5.22)$$

where

$$A_{n,\sigma} = \left\{ \tilde{N}(0)^{-1/2} \exp[i\theta(0)] \right\}^{-1} (i a_{n,\sigma}) \quad (5.23)$$

When multiplied by  $\exp(-i\sigma t)$ , Eqs. (5.21)-(5.23) represent a wave solution with upward phase (downward energy) propagation.

(ii)  $\epsilon_{n,\sigma} < 0$

$$W_{n,\sigma}(z) = B_{n,\sigma} \tilde{N}(z)^{-1/2} \exp[\theta(z)], \quad (5.24)$$

$$F_{n,\sigma}(z) = \frac{-N_0}{2\Omega \sigma} |\epsilon_{n,\sigma}|^{-1/2} B_{n,\sigma} \tilde{N}(z)^{1/2} \exp[\theta(z)] \quad (5.25)$$

where

$$B_{n,\sigma} = \left\{ [\tilde{N}(0)]^{-1/2} \exp[\theta(0)] \right\}^{-1} (i a_{n,\sigma}) \quad (5.26)$$

Eqs. (5.24)-(5.26) represent an evanescent solution trapped to the surface ( $z = 0$ ).

Bottom forcing

(i)  $\epsilon_{n,\sigma} > 0$

$$W_{n,\sigma}(z) = C_{n,\sigma} \tilde{N}(z)^{-1/2} \exp[-i\theta(z)], \quad (5.27)$$

$$F_{n,\sigma}(z) = \frac{-iN_0}{2\Omega\sigma} |\epsilon_{n,\sigma}|^{-1/2} C_{n,\sigma} \tilde{N}(z)^{1/2} \exp[-i\theta(z)], \quad (5.28)$$

where

$$C_{n,\sigma} = [\tilde{N}(-1)]^{1/2} (i a_{n,\sigma}) \quad (5.29)$$

When multiplied by  $\exp(-i\sigma t)$ , Eqs. (5.27)-(5.29) represent a wave solution with downward phase (upward energy) propagation.

(ii)  $\epsilon_{n,\sigma} < 0$

$$W_{n,\sigma}(z) = C_{n,\sigma} \tilde{N}(z)^{-1/2} \exp[-\theta(z)], \quad (5.30)$$

$$F_{n,\sigma}(z) = \frac{N_0}{2\Omega\sigma} |\epsilon_{n,\sigma}|^{-1/2} C_{n,\sigma} \tilde{N}(z)^{1/2} \exp[-\theta(z)]. \quad (5.31)$$

Eqs. (5.30)-(5.31) represent an evanescent solution trapped to the bottom ( $z = -1$ ).

To complete the solutions, we proceed to the latitudinal problem in the next section, solving for the eigenfunctions  $P_{n,\sigma}$  and  $V_{n,\sigma}$  and their eigenvalues  $\epsilon_{n,\sigma}$  for given  $k_0$ .

### 5.3 Asymptotic solutions of the Laplace's tidal equations in the parameter regime of inertial waves

#### 5.3a Introduction

General eigensolutions of the LTE, the so-called Hough functions, were investigated extensively by Flattery (1967) and Longuet-Higgins (1968), but they are global in character and inconvenient to apply in describing a localized, high wavenumber phenomenon such as oceanic inertial waves. Because the non-dimensional parameter of the LTE,  $\epsilon = \frac{4\Omega^2 R^2}{gh}$ , where  $R$  is the radius of the earth,  $h$  the equivalent depth for a particular mode,  $g$  the gravity, is very large ( $\gtrsim 10^5$ ) under oceanic conditions, asymptotic approximations in terms of  $\epsilon$  have been applied by several investigators. The spheroidal wave equation was applied by Longuet-Higgins (1965), and by Munk and Phillips (1968) to approximate the LTE for large  $\epsilon$ . Solutions obtained by the latter authors were applied in Chapter 4 to construct the global wave model; however, these solutions are invalid for  $\phi \sim \cos^{-1}\left(\frac{k}{\epsilon^{1/2}\sigma}\right)$  (see Section 3.3). For a forced model, we need uniformly valid eigensolutions to expand a given forcing function, therefore the solutions of MP cannot be applied here. Using matched asymptotic expansion methods, Kamenkovich and Tsybaneva (1975 a, b) obtained uniformly valid asymptotic solutions in two limits: (a)  $k$  is of order unity; (b)  $k$  is of order  $\epsilon^{1/2}$ . As originally pointed out by MP, the zonal wavenumber of inertial waves is of order  $\epsilon^{1/3}$  or less; in this limit, Kamenkovich et al (1977) have derived asymptotic formula for positive  $\epsilon$  but not for negative  $\epsilon$ . Miles (1977) has extensively discussed asymptotic eigensolutions of the

LTE with large  $\epsilon$  ; however, for  $\sigma < 1$ , his results are formally valid only for  $k/\sigma \lesssim 0(1)$ .

The purpose of this section is to present an asymptotic expansion procedure for the LTE with zonal wavenumber ranging from zero to order  $\epsilon^{1/3}$ , which includes case (a) of Kamenkovich and Tsybaneva (1975 a) as a limiting case. However, the geometry is different; the ocean is not assumed to cover the whole earth but to be bounded by two latitudes  $\pm \phi_b$ . The reason for this assumption is to avoid the complexity involved near the poles, which actually are separated from the major oceans. Moreover, the high modes of interest are insensitive to the details of the boundary conditions. To be remote from the mid-latitudes which are our major concern,  $\phi_b$  has been arbitrarily set to be  $60^\circ$ . For given  $k$ , approximate eigensolutions and eigenvalues have been obtained. The results for positive eigenvalues, which are not affected by boundary conditions poleward of the turning latitude, have been compared with Longuet-Higgins' numerical results (1968).

### 5.3b Solutions

Dropping all the subscripts, we rewrite (5.10) here for reference

$$(1-\nu^2) \frac{d^2 P}{d\nu^2} + 2\nu \frac{1-\sigma^2}{\sigma^2-\nu^2} \frac{dP}{d\nu} \left[ \epsilon(\sigma^2-\nu^2) - \frac{k^2}{1-\nu^2} - \frac{k}{\sigma} \frac{\nu^2+\sigma^2}{\nu^2-\sigma^2} \right] P = 0 \quad (5.32)$$

The eigenvalue  $\epsilon$  can be either positive or negative, and we call the corresponding eigensolutions "positive modes" and "negative modes" respectively.

In the parameter regime of oceanic inertial waves, i.e.,  $|\epsilon| \gg 1$ ,

$\sigma \lesssim O(1)$ , and  $k \lesssim O(\epsilon^{1/3})$ , from the dispersion diagrams of Longuet-Higgins (1968), only the type 1, type 4, and type 5 waves as classified by him are present. Type 1 waves are inertia-gravity waves with  $\epsilon > 0$ ; type 4 and type 5 waves are westward-going and eastward-going waves respectively with  $\epsilon < 0$ , which are trapped in the vertical. We shall treat first the case of positive modes.

(i) Positive modes

If we write

$$k = s \epsilon^{1/3}, \quad (s \lesssim O(1)) \quad (5.33)$$

and

$$G(\nu) = (\sigma^2 - \nu^2)(1 - \nu^2) - \epsilon^{-1/3} s^2 \quad (5.34)$$

then Eq. (5.32) becomes

$$(1 - \nu^2) \frac{d^2 P}{d\nu^2} + 2\nu \frac{1 - \sigma^2}{\sigma^2 - \nu^2} \frac{dP}{d\nu} + \left[ \epsilon \frac{G(\nu)}{1 - \nu^2} - \frac{s}{\sigma} \epsilon^{1/3} \frac{\nu^2 + \sigma^2}{\nu^2 - \sigma^2} \right] = 0 \quad (5.35)$$

there are two positive roots,  $\nu_0$  and  $\nu_1$ , of the equation  $G(\nu) = 0$ .

Assuming that  $\nu_0 < \nu_1$ , then we have

$$\nu_0 = \sigma \left[ 1 - \frac{s^2}{2} \epsilon^{-1/3} \frac{1}{\sigma^2(1 - \sigma^2)} \right] + O(\epsilon^{-2/3}) \quad (5.36)$$

$$\nu_1 = 1 + \frac{s^2}{2} \epsilon^{-1/3} \frac{1}{1 - \sigma^2} + O(\epsilon^{-2/3}) \quad (5.37)$$

The latitudes corresponding to  $\pm \nu_0$  are the "turning latitudes," where Eq.(5.35) changes from hyperbolic ( $|\nu| < \nu_0$ ) to elliptic ( $|\nu| > \nu_0$ ).

The latitudinal boundaries,  $\pm \phi_b$ , are presumably poleward of the turning latitudes; to be specific, we assume that  $|\sigma - \sin \phi_0| \gg \epsilon^{-1/3}$  in what follows. Following the method of matched asymptotic expansion (Nayfeh, 1973), we shall first derive the "turning point solution" which is valid in the vicinity of  $\nu_0$ , and the "outer solution" which is valid as  $(\nu - \nu_0) \sim O(1)$ ; then obtain a uniformly valid composite solution using the matching conditions.

Turning point solution (  $P_i$  )

In the vicinity of  $\nu_0$ , we define

$$\xi = (\nu - \nu_0) \epsilon^\beta \quad (5.38)$$

and 
$$P_i = B_0 + B_1 \epsilon^\alpha + B_2 \epsilon^{2\alpha} + \dots \quad (5.39)$$

If we substitute (5.38) and (5.39) into (5.35) and equate terms of equal power in  $\epsilon$ , then the balance among dominant terms yields  $\alpha = -1/3$ ,

$$\beta = 1/3 \text{ and}$$

$$\frac{d^2 B_0}{d\xi^2} - \frac{1}{\xi - \frac{bS}{2\nu_0}} \frac{dB_0}{d\xi} - \left[ c\xi + \frac{b}{\xi - \frac{bS}{2\nu_0}} \right] B_0 = 0 \quad (5.40)$$

where

$$c = \frac{2\nu_0(\nu_1^2 - \nu_0^2)}{(1 - \nu_0^2)^2}, \quad b = \frac{S}{1 - \nu_0^2} \quad (5.41)$$

An approximate solution to (5.40) was found to be



$$\Gamma(\xi) = r \operatorname{Ai}(c^{1/3} \xi) - c^{1/3} \operatorname{Ai}'(c^{1/3} \xi), \quad (5.42)$$

where

$$r = b \left( \frac{\nu_1^2 - \nu_0^2}{1 - \nu_0^2} \right); \quad (5.43)$$

$\operatorname{Ai}$  and  $\operatorname{Ai}'$  are the Airy function and its derivative which are bounded at  $+\infty$ .  $\Gamma(\xi)$  satisfies Eq. (5.40) with the  $b$ 's replaced by  $r$ 's. From Eqs. (5.36), (5.37), and (5.43) we have

$$r = b [1 + O(\epsilon^{-1/3})],$$

and consequently

$$\Gamma(\xi) = B_0(\xi) + O(\epsilon^{-1/3}).$$

Therefore  $\Gamma(\xi)$  is a consistent first order approximation of  $P_i$ , i.e.,

$$P_i = \Gamma(\xi) + O(\epsilon^{-1/3}) \quad (5.44)$$

#### Outer solution ( $P_0$ )

Solutions poleward of the turning latitudes are exponentially small as indicated by the Airy functions in (5.42); hence they have no effects on solutions equatorward of the turning latitudes, and we shall not derive them in detail. For  $\nu < \nu_0$ , an appropriate expansion was found to be

$$P_0(\nu) = M (A_0 + \epsilon^{-1/6} A_1 + \epsilon^{-1/3} A_2 + \epsilon^{-1/2} A_3 + \dots) \exp[\pm i \epsilon^{1/2} a(\nu)] \quad (5.45)$$

where  $M$  is a constant to be determined by the matching conditions. It is clear from (5.44) and (5.45) that we must carry the second order term

$A_1$  in (5.45), in order to obtain a uniformly valid solution.

Substituting (5.45) into (5.35) and equating terms of equal power in  $\epsilon$ , we obtain

$$a(\nu) = \int_{\nu}^{\nu_0} \frac{G^{1/2}}{1-\nu'^2} d\nu' \quad (5.46)$$

$$A_0(\nu) = \left| \frac{\nu_0^2 - \nu^2}{\nu_1^2 - \nu^2} \right|^{1/4} \quad (5.47)$$

$$A_1(\nu) = \mp \frac{iS}{2\nu_0} A_0(\nu) F(\nu) \quad (5.48)$$

where the signs correspond to those in (5.45), and

$$F(\nu) = \frac{\nu^2 + \nu_0^2}{\nu \left| (\nu_0^2 - \nu^2)(\nu_1^2 - \nu^2) \right|^{1/2}} + \int_{\nu}^{\nu_0} \left| \nu_0^2 - \nu'^2 \right|^{-1/2} \frac{d}{d\nu'} f(\nu') d\nu' \quad (5.49)$$

$$f(\nu) = \frac{\nu^2 + \nu_0^2}{\nu (\nu_1^2 - \nu^2)^{1/2}} \quad (5.50)$$

We should note here that each term on the right-hand side of Eq. (5.49) is singular when  $\nu = 0$ , but it can be shown that

$$\lim_{\nu \rightarrow 0} F(\nu) = O(1)$$

#### Composite solution

In the vicinity of  $\nu_0$ ,  $P_i$  and  $P_0$  should match each other in the

following sense,

$$\lim_{\nu \rightarrow \nu_0} P_o(\nu) = \lim_{\xi \rightarrow -\infty} P_i(\xi) \quad (5.51)$$

Using Eq.(5.44) and the asymptotic behavior of the Airy function, the right-hand side of (5.51), denoted by  $P_m$ , can be written as

$$P_m = \pi^{-1/2} C^{5/12} \epsilon^{1/2} (\nu_0 - \nu)^{1/4} \left\{ \cos \Theta + \epsilon^{-1/6} (\nu_0 - \nu)^{-1/2} \frac{S \sin \Theta}{[2\nu_0(\nu_1^2 - \nu_0^2)]^{1/2}} \right\} \quad (5.52a)$$

where

$$\Theta = \frac{2}{3} \epsilon^{1/2} C^{1/2} (\nu_0 - \nu)^{3/2} + \frac{\pi}{4} \quad (5.52b)$$

Now the constant M in (5.45) can be determined through the use of Eqs. (5.45)-(5.52), yielding the following result :

$$M = \left( \frac{\nu_1^2 - \nu_0^2}{2\nu_0} \right)^{1/4} \pi^{-1/2} \epsilon^{1/2} C^{5/12} \quad (5.53)$$

The outer solution which satisfies Eq. (5.51) can be written as

$$P_o = M A_o(\nu) \left\{ \cos \left[ \epsilon^{1/2} a(\nu) + \frac{\pi}{4} \right] + \epsilon^{-1/6} \frac{S}{2\nu_0} F(\nu) \sin \left[ \epsilon^{1/2} a(\nu) + \frac{\pi}{4} \right] \right\} + O(\epsilon^{-1/3}) \quad (5.54)$$

thus a uniformly valid composite solution can be expressed by

$$P = P_o + P_i - P_m \quad (5.55)$$

Velocity solutions can be obtained from the pressure through the use

of (5.12), which has been rewritten as

$$V = \frac{\sigma}{v^2 - \sigma^2} \left[ (1 - v^2) \frac{dP}{dv} + \epsilon^{1/3} \frac{Sv}{\sigma} P \right] \quad (5.56)$$

From Eqs. (5.44), (5.52), (5.54), (5.55), and (5.56), the following expressions are obtained,

$$V_i = -\epsilon^{2/3} v_0 A_i (c^{1/3} \xi)$$

$$V_o = M \left( \frac{1 - v_o^2}{v_i^2 - v_o^2} \right) \epsilon^{1/2} v_o \frac{A_o}{v^2 - v_o^2} \left\{ G^{1/2} \sin \left[ \epsilon^{1/2} a(v) + \frac{\pi}{4} \right] + \epsilon^{-1/6} \frac{S}{v_o} \left( v - \frac{1}{2} G^{1/2} F \right) \cos \left[ \epsilon^{1/2} a(v) + \frac{\pi}{4} \right] \right\} \quad (5.57)$$

$$V_m = -\frac{\epsilon^{1/2}}{2} (2v_o)^{3/4} (v_i^2 - v_o^2)^{1/4} (v_o - v)^{-1/4} \sin \Theta$$

$$V = V_o + V_i - V_m$$

The meanings of the subscripts are the same as before.

### Eigensolutions

Since the positive modes are either even or odd functions in the interval  $[-\phi_b, \phi_b]$ , we must have either

$$\left. \frac{dP}{dv} \right|_{v=0} = 0 \quad (\text{even}), \quad (5.58a)$$

or  $P(0) = 0 \quad (\text{odd}) \quad (5.58b)$

Substituting the asymptotic series for  $P$  (Eq. (5.54)) into (5.58a) and (5.58b), the first order approximation to the eigenvalues can be written as

$$\epsilon_n^{\pm 1/2} = \left( n \mp \frac{1}{2} \right) \frac{\pi}{2} / a(0) + O(\epsilon^{-1/6}) \quad (5.59)$$

where the upper sign corresponds to  $k > 0$  and the lower sign to  $k < 0$ ;  $n$  is the number of zeros of  $P(\nu)$  ( $V(\nu)$ ) in the interval  $[-\phi_b, \phi_b]$  if  $k > 0$  ( $k < 0$ ). Eq.(5.59) is equivalent to the result of Kamenkovich et al (1977, Eq.(4)) within  $O(\epsilon^{-1/6})$ . The reason for using the zeros of different variables to label the eigensolutions for eastward and westward waves is the following: The number of zeros of  $P(\nu)$  ( $V(\nu)$ ) is invariant with respect to  $\epsilon$  if  $k > 0$  ( $k < 0$ ) (Longuet-Higgins, 1968); thus we are able to identify the eigen-curves ( $\epsilon_n$  vs  $\sigma$  for given  $n$  and  $k$ ) calculated using (5.59) with those of Longuet-Higgins (1968) for small and moderate  $\epsilon$ . The relation between the number of zeros for  $P$  and that for  $V$  is varying with  $\epsilon_n$ , so the formula given by Odulo (1972), which is independent of  $\epsilon_n$ , is not strictly correct (e.g., compare his formula with Longuet-Higgins' Fig.11).

With the eigenvalues given by (5.59), Eqs. (5.58a) and (5.58b) are not satisfied to second order. Hence the eigensolutions represented by (5.55), (5.57), and (5.59) have error terms of order  $\epsilon^{-1/6}$ , although the proposed asymptotic series could produce solutions accurate to  $O(\epsilon^{-1/3})$  if the true eigenvalues were known. Second order calculations of  $\epsilon_n$  are straightforward, but require considerable efforts; however, they are not significant for the problem of inertial waves due to the largeness of  $\epsilon_n$ .

Since  $a(0)$  itself is dependent on  $\epsilon_n$ , Eq.(5.59) was evaluated using

an iteration method. Comparisons of the eigenvalues obtained from (5.59) with those taken from Longuet-Higgins' paper (1968) are presented in Table 5.1. Note that the first order approximations to  $\epsilon_n$  are degenerate and lie between the numerical results for positive and negative  $k$ . The error is only about 6 % even when  $\epsilon_n$  is as small as 23. The accuracy of Eq. (5.59) has also been confirmed by Kamenkovich et al (1977) using numerical results. Eigensolutions with  $k = \pm 50$ ,  $\sigma = .5878$ ,  $\epsilon_n^{1/2} = 370.2$ , and  $n = 63$  ( $k > 0$ ),  $62$  ( $k < 0$ ), are displayed in Figs. 5.1a and 5.1b. Note that  $P$  has  $n$  zeros for  $k > 0$  and  $(n-1)$  zeros for  $k < 0$ , while  $V$  has  $(n-1)$  zeros for  $k > 0$  and  $n$  zeros for  $k < 0$ .

Table 5.1

Positive eigenvalues with  $|k| = 5$  ( $\epsilon$  is from Eq. (5.59),  $\epsilon_+$  and  $\epsilon_-$  are from Longuet-Higgins' numerical calculation for  $k = 5$  and  $-5$  respectively.  $n_+$  and  $n_-$  are the numbers of zeros of  $P$  for  $k > 0$  and of  $V$  for  $k < 0$  respectively.

$\sigma$	$n_+$	$n_-$	$\epsilon_+^{1/2}$	$\epsilon_-^{1/2}$	$\epsilon$
.2303	3	2	102.7	94.3	98.6
.2886	4	3	89.3	84.2	86.8
.3408	5	4	81.	77.5	79.3
.3885	6	5	75.3	72.6	73.9
.4329	7	6	70.9	68.8	69.8
.4859	7	6	56.6	54.6	55.6
.5456	7	6	45.2	43.3	44.3
.6132	7	6	36.2	34.4	35.3
.6902	7	6	29.	27.2	28.3
.78	7	6	23.3	21.6	22.9

Figure 5.1a Eigensolutions of v-velocity (upper one) and pressure (lower one) with  $\sigma = 0.5878$ ,  $k = 50$ ,  $n = 63$ , and  $\epsilon_n^{1/2} = 370.2$ .

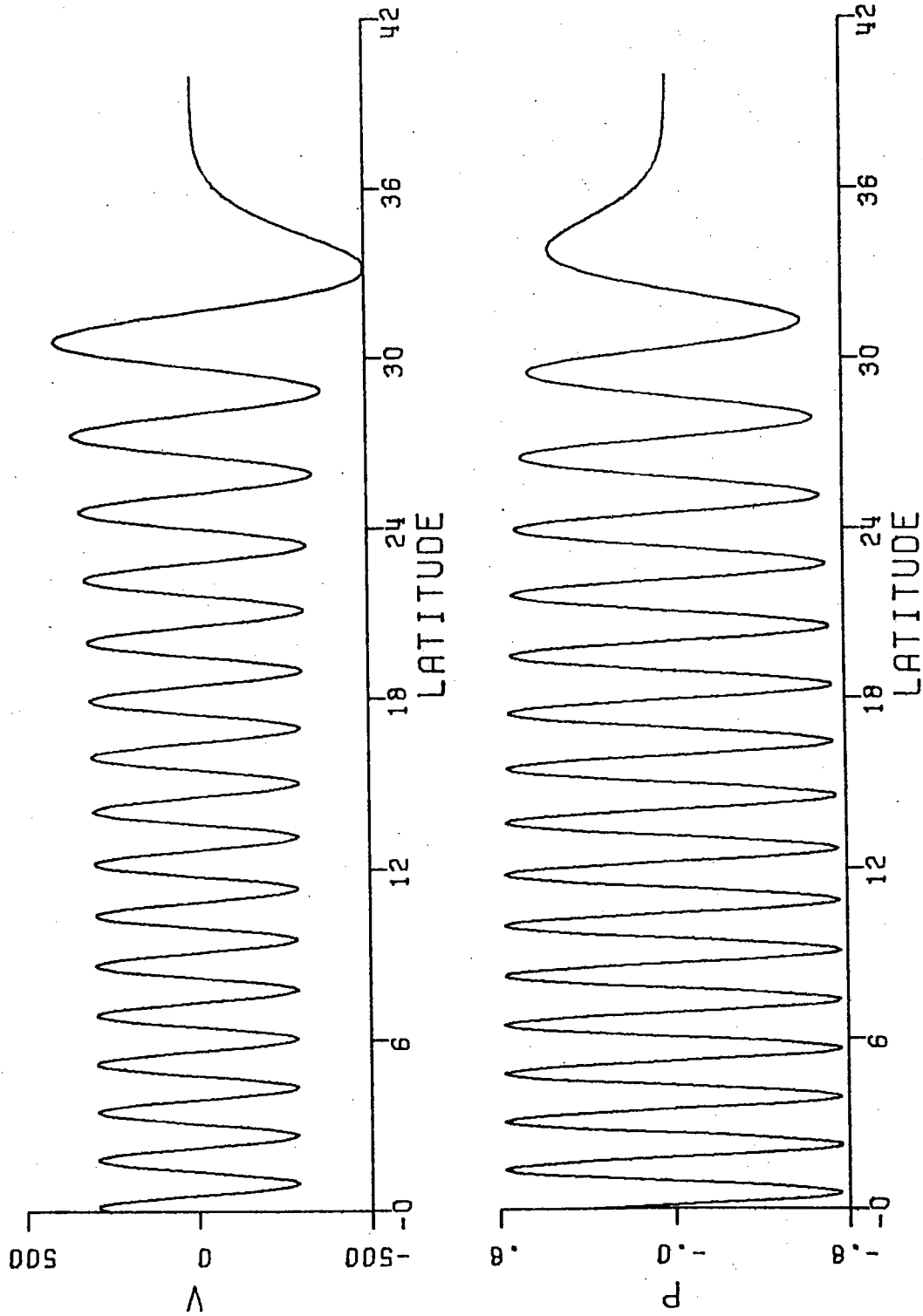
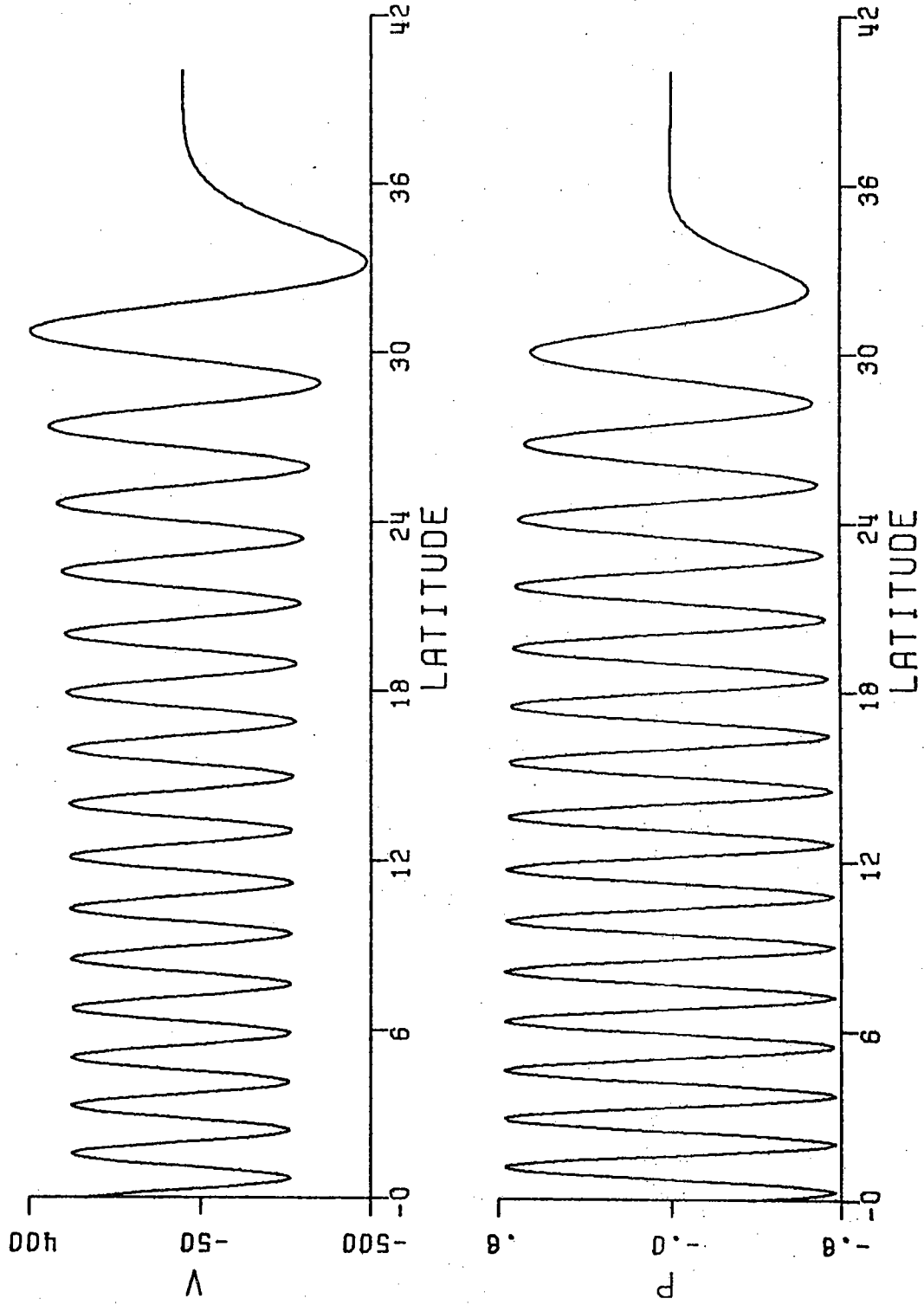


Figure 5.1b As in Fig. 5.1a except that  $k = -50$ , and  $n = 62$ .





(ii) Negative modes

If we define  $\gamma = |\epsilon|$ , then Eq. (5.32) becomes

$$(1-\nu^2) \frac{d^2 P}{d\nu^2} + 2\nu \frac{1-\sigma^2}{\sigma^2-\nu^2} \frac{dP}{d\nu} + \left[ \gamma \frac{E(\nu)}{1-\nu^2} - \frac{\gamma^{1/3} s}{\sigma} \frac{\nu^2 + \sigma^2}{\nu^2 - \sigma^2} \right] P = 0$$

where 
$$E(\nu) = (\nu^2 - \sigma^2)(1 - \nu^2) - \gamma^{-1/3} s^2$$

The two positive roots for  $E(\nu) = 0$  are

$$\nu_0 = \sigma + \frac{s^2}{2} \gamma^{-1/3} \frac{1}{\sigma(1-\sigma^2)} + O(\gamma^{-2/3})$$

and 
$$\nu_1 = 1 - \frac{s^2}{2} \gamma^{-1/3} \frac{1}{1-\sigma^2} + O(\gamma^{-2/3})$$

It is obvious that the solution now is oscillatory between the two turning points  $\nu_0$  and  $\nu_1$ , exponentially decaying equatorward of  $\nu_0$ , and having a complicated boundary layer between  $\nu_1$  and 1. The problem associated with the poles will not be pursued here; the boundaries we have chosen,  $\pm \phi_b$ , are sufficiently distant from the poles to avoid the turning point  $\nu_1$  and its boundary layer. Because the expansion procedure is exactly the same as that used in (ii), only the results are presented below.

Pressure

$$P_0 = M A_0(\nu) \left\{ \cos \left[ \gamma^{1/2} a(\nu) + \frac{\pi}{4} \right] + \gamma^{-1/6} \frac{s}{2\nu_0} F(\nu) \sin \left[ \gamma^{1/2} a(\nu) + \frac{\pi}{4} \right] \right\}$$

$$P_i = -b \text{Ai} \left[ c^{1/3} \gamma^{1/3} (\nu_0 - \nu) \right] - c^{1/3} \text{Ai}' \left[ c^{1/3} \gamma^{1/3} (\nu_0 - \nu) \right]$$

(5.60)

$$P_m = \left( \frac{2\nu_0}{\nu_1^2 - \nu_0^2} \right)^{1/4} (\nu - \nu_0)^{1/4} \left\{ \cos \Theta - \gamma^{-1/6} \frac{s \sin \Theta}{[2\nu_0(\nu_1^2 - \nu_0^2)]^{1/2}} (\nu - \nu_0)^{-1/2} \right\}$$

where  $\Theta = \frac{2}{3} \gamma^{1/2} c^{1/2} (\nu - \nu_0)^{3/2} + \frac{\pi}{4}$

and  $a(\nu) = \int_{\nu_0}^{\nu} \frac{E^{1/2}(\nu')}{1 - \nu'^2} d\nu'$

The expressions for  $M$ ,  $A_0(\nu)$ ,  $b$ ,  $c$ , and  $F(\nu)$  are the same as before.

#### Velocity

$$V_0 = -M \left( \frac{1 - \nu_0^2}{\nu_1^2 - \nu_0^2} \right) \gamma^{1/2} \nu_0 \frac{A_0(\nu)}{\nu^2 - \nu_0^2} \left\{ E(\nu)^{1/2} \sin \left[ \gamma^{1/2} a(\nu) + \frac{\pi}{4} \right] - \gamma^{-1/6} \frac{s}{\nu_0} \left[ \nu + \frac{1}{2} E(\nu)^{1/2} F(\nu) \right] \cos \left[ \gamma^{1/2} a(\nu) + \frac{\pi}{4} \right] \right\}$$

$$V_i = -\gamma^{2/3} \nu_0 \text{Ai} \left[ c^{1/3} \gamma^{1/3} (\nu_0 - \nu) \right]$$

(5.61)

$$V_m = -\frac{\gamma^{1/2}}{2} (2\nu_0)^{3/4} (\nu_1^2 - \nu_0^2)^{1/4} (\nu - \nu_0)^{-1/4} \sin \Theta$$

#### Eigenvalues

The boundary conditions at  $\pm \phi_b$  are simply  $V = 0$ ; hence the approximate eigenvalues are

$$\gamma^{1/2} = \left( n - \frac{1}{4} \right) \pi / a(\nu_m) + O(\gamma^{-1/6}),$$

where  $\nu_m = \sin \phi_b$ ;  $n$  is the number of zeros of  $V(\nu)$  in  $[0, \phi_b]$ . The eigensolutions with  $k = \pm 50$ ,  $\sigma = .5878$ ,  $\gamma_n^{1/2} = 573.1$ , and  $n = 31$ , are displayed in Figs. 5.2a and 5.2b. Now the number of zeros of  $P$  in  $[0, \phi_b]$  is  $(n-1)$  for  $k > 0$  and  $n$  for  $k < 0$ . Solutions in the Southern Hemisphere, which are not shown here, are either symmetric or anti-symmetric with their counterparts in the Northern Hemisphere; thus these two cases are degenerate.

#### 5.4 Results

Our major interests are in finding model spectra of  $v$  and  $w$  at  $\phi_o$  as functions of depth, which can be directly compared with the observations presented in Chapter 2. In other words, for each  $\sigma$  in  $[\sigma_1, \sigma_2]$ , we want to calculate  $|\hat{w}(\phi_o, z, \sigma)|^2$  and  $|\hat{v}(\phi_o, z, \sigma)|^2$ . With the knowledge of  $P_{n,\sigma}(\phi)$ ,  $V_{n,\sigma}(\phi)$ ,  $W_{n,\sigma}(z)$ , and  $F_{n,\sigma}(z)$  as derived in 5.2 and 5.3, the calculation is straightforward using Eqs. (5.7) and (5.8). To be specific, we choose  $\phi_o = 36^\circ$ ,  $\sigma_1 = .94 \sin \phi_o$ , and  $\sigma_2 = 1.26 \sin \phi_o$ . For given  $\sigma$  in  $[\sigma_1, \sigma_2]$ , we have calculated  $|\hat{w}|^2$  and  $|\hat{v}|^2$  with three different forcing scales at the following four depths: 200 m, 600 m, 1500 m, and 4000 m. Calculations have been made for both surface and bottom forcing.

For given  $\sigma$ , the first step was to calculate the  $a_{n,\sigma}$ 's from (5.16), in which the integration was evaluated numerically using the trapezoidal rule. For both positive and negative modes, the value of  $a_{n,\sigma}$  initially increases with  $n$ ; after reaching a maximum at some intermediate  $n$ , it then decreases with  $n$ . In general, the calculation was truncated at four mode numbers  $n_1, n_2, n_3$ , and  $n_4$  such that

Figure 5.2a As in Fig. 5.1a except that  $n = 31$  and  $(-\epsilon_n)^{\frac{1}{2}} = 573.1$ .

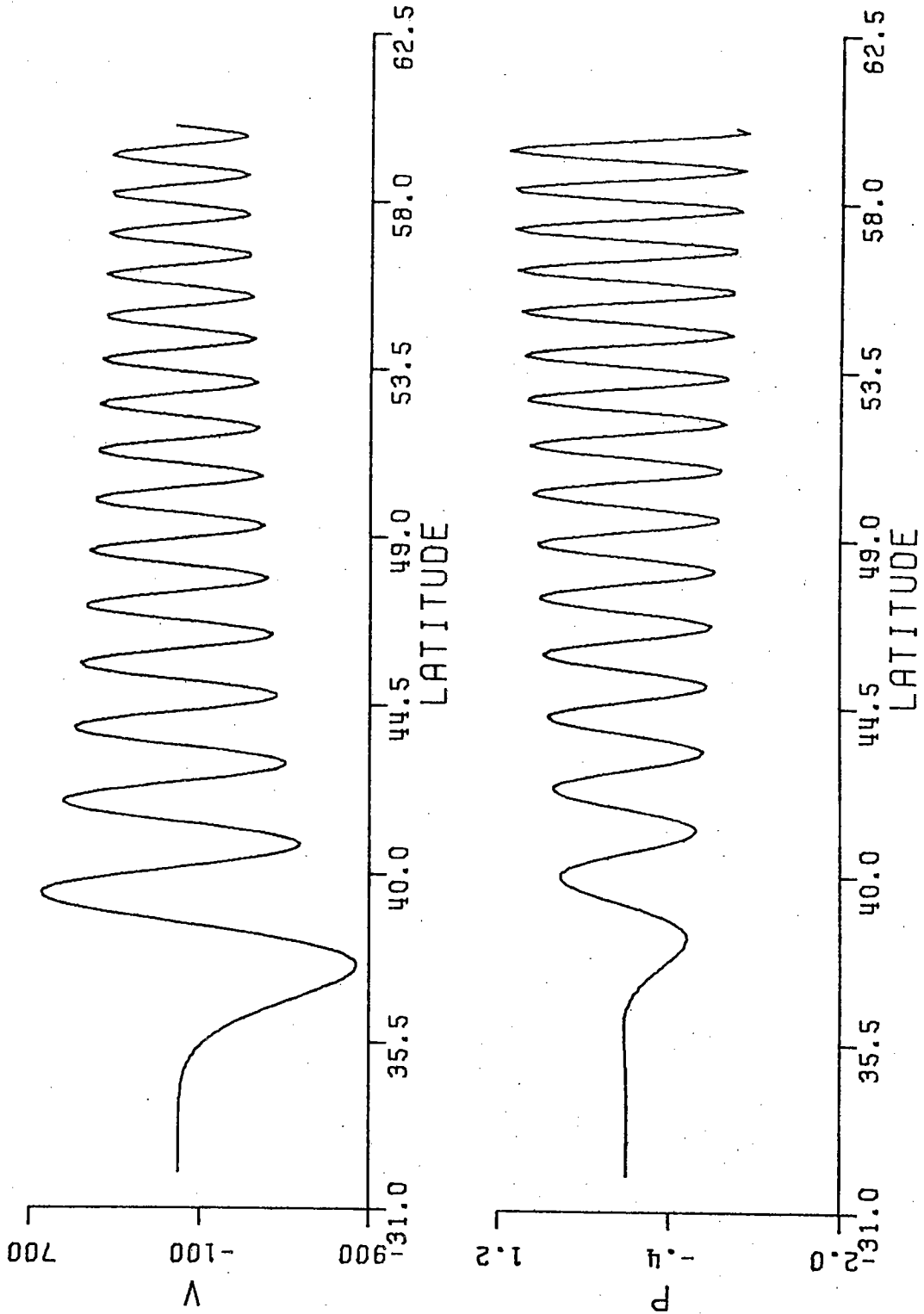
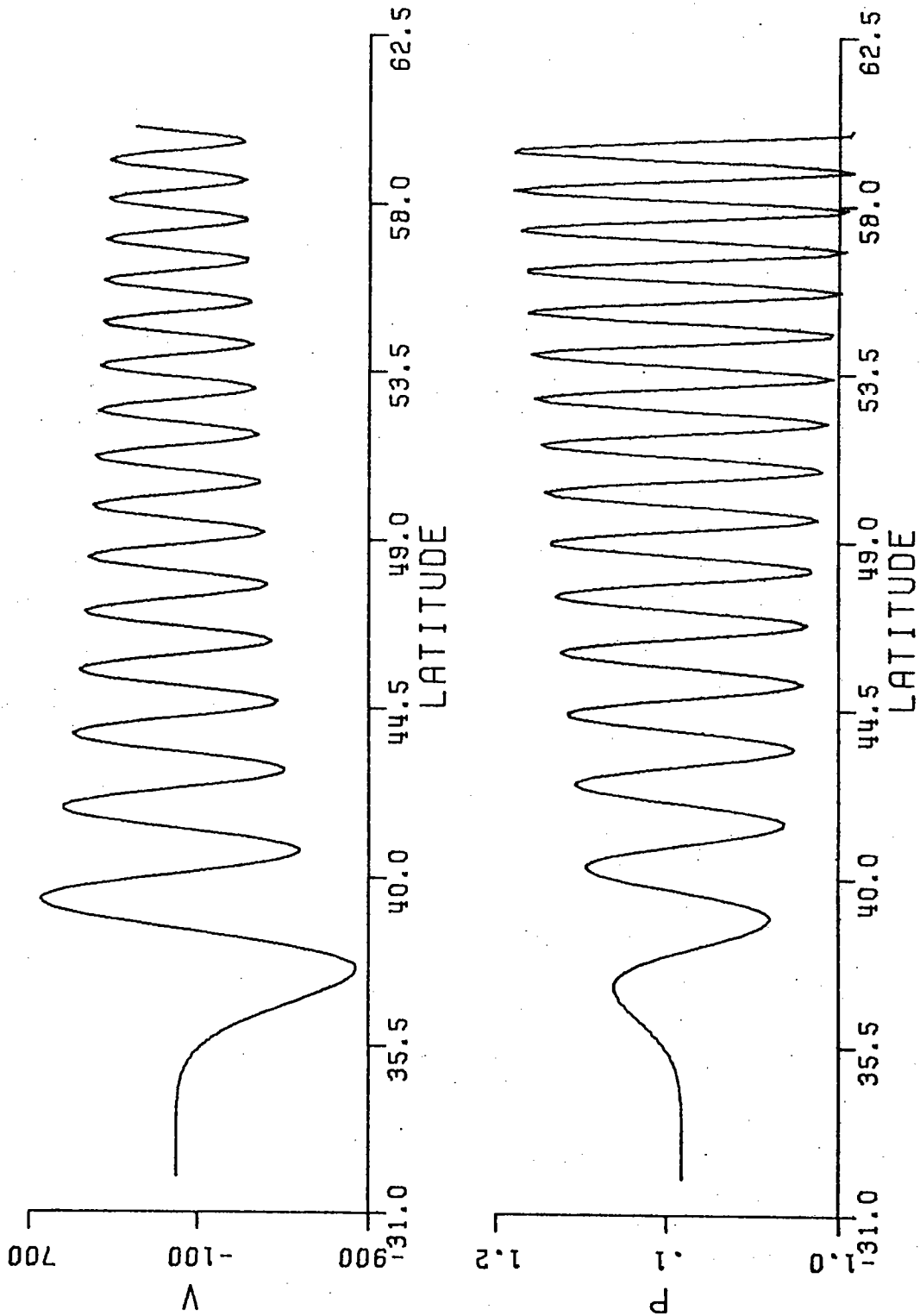


Figure 5.2b As in Fig. 5.1a except that  $n = 31$ ,  $(-\epsilon_n)^{1/2} = 573.1$ , and  $k = -50$ .



$$\underbrace{\sum_{n=n_1}^{n_2} |a_{n,\sigma}|^2 N_{n,\sigma}}_{\epsilon_{n,\sigma} < 0} + \underbrace{\sum_{m=n_3}^{n_4} |a_{m,\sigma}|^2 N_{m,\sigma}}_{\epsilon_{m,\sigma} > 0} \geq 0.9 \int_{-\phi_b}^{\phi_b} |\hat{w}_b|^2 d\phi, \quad (5.62)$$

where

$$N_{n,\sigma} = \int_{-\phi_b}^{\phi_b} P_{n,\sigma}^2(\phi) d\phi$$

Values of  $n_1$ ,  $n_2$ ,  $n_3$ , and  $n_4$  for nine selected frequencies in  $[\sigma_1, \sigma_2]$  are listed in Table 5.2 for three different forcing scales:  $L = 300$  km, 150 km, and 75 km. For frequencies sufficiently greater than  $\sin \phi_o$ , we need only positive modes to describe  $\hat{w}_b(\phi)$  because negative modes are trapped far to the north of the forced region. For frequencies close to  $\sin \phi_o$ , we need both kinds of mode and the expansion is not particularly efficient; it needs several hundred modes. It is conceivable that for frequencies much less than  $\sin \phi_o$  (not shown), only negative modes will contribute because positive modes are trapped far to the south of  $\phi_o$ . It is also expected from Fourier theory that smaller scale forcing requires more modes to describe. Note that although some mode numbers in Table 5.2 are small, their corresponding eigenvalues are at least  $O(2000)$  -- still large enough for the validity of the asymptotic expansion. For the case with  $L = 300$  km, the forcing function  $\hat{w}_b(\phi)$  and its expansion in terms of  $P_{n,\sigma}$  are displayed in Figs. 5.3a and 5.3b for  $\sigma = \sin \phi_o$  and  $\sigma = 1.12 \sin \phi_o$  respectively. Slightly wavy behavior is observed when  $\sigma = \sin \phi_o$ ; however, the localized shape is well reproduced. The results for other forcing scales are similar.

Table 5.2Values of  $n_1, n_2, n_3, n_4$ L = 300 km

$\frac{\sigma}{\sin \phi_0}$	$n_1$	$n_2$	$n_3$	$n_4$
.94	2	65	4	110
1.	4	66	2	140
1.01	11	46	2	111
1.02			3	86
1.035			3	66
1.06			6	46
1.12			6	44
1.19			6	41
1.26			5	41

L = 150 km

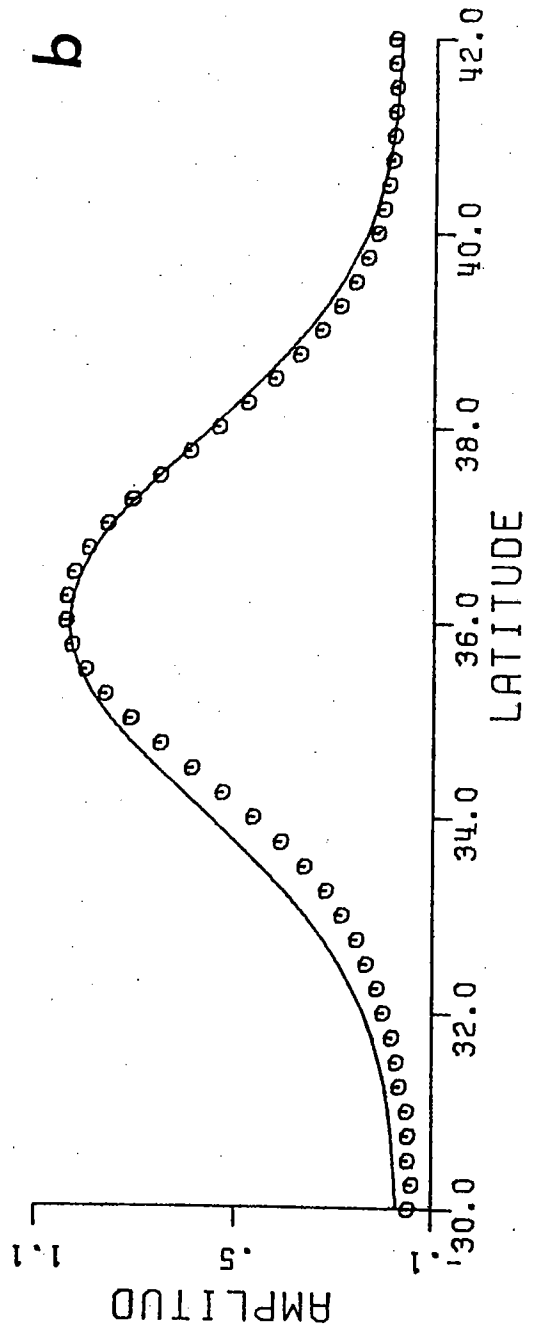
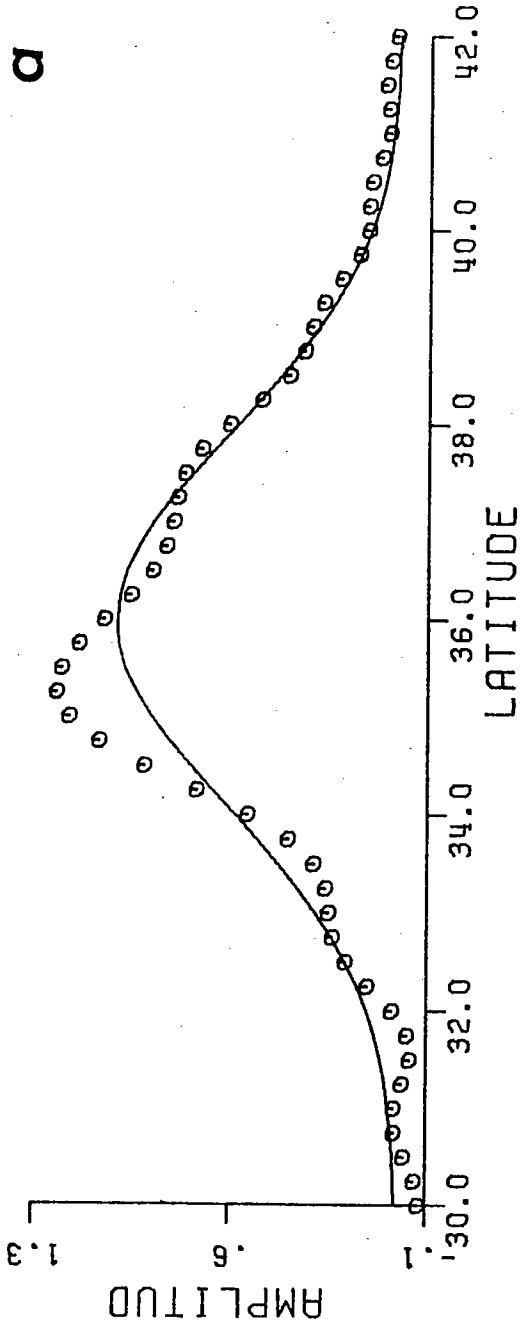
$\frac{\sigma}{\sin \phi_0}$	$n_1$	$n_2$	$n_3$	$n_4$
.94	6	80	34	81
1.	17	181	16	386
1.01	17	61	16	226
1.02			16	141
1.035			16	106
1.06			15	76
1.12			13	72
1.19			12	70
1.26			12	68

Table 5.2 (contd.)L = 75 km

$\frac{\sigma}{\sin \phi_0}$	$n_1$	$n_2$	$n_3$	$n_4$
.94	11	102		
1.	53	450	54	1010
1.01	60	102	54	440
1.02			52	261
1.035			48	170
1.06			44	158
1.12			19	140
1.19			16	130
1.26			25	125



Figure 5.3 The forcing function  $\hat{w}_b(\phi)$  (solid curve) and its expansion in terms of  $P_{n,\sigma}$  (symbols) for (a)  $\sigma = \sin \phi_0$  and (b)  $\sigma = 1.12 \sin \phi_0$ , where  $\phi_0 = 36^\circ$  and the forcing scale  $L = 300$  km.



### 5.4a Surface forcing

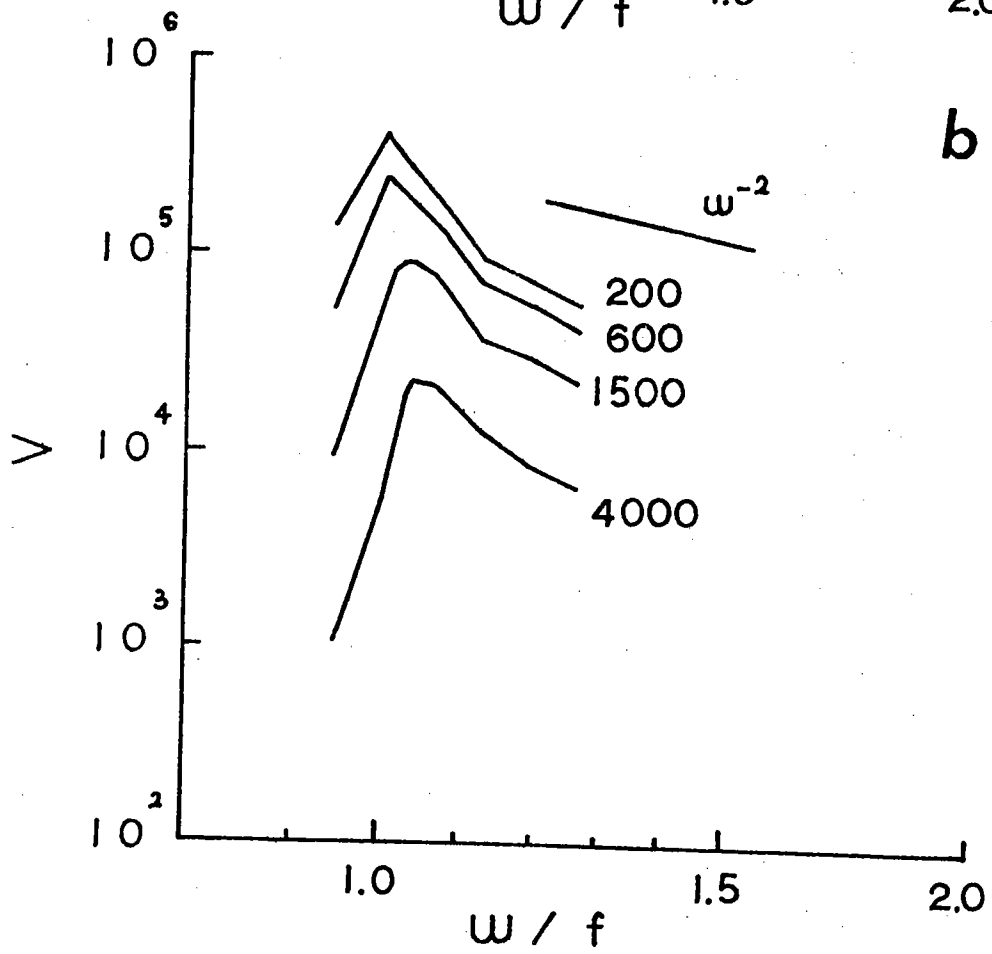
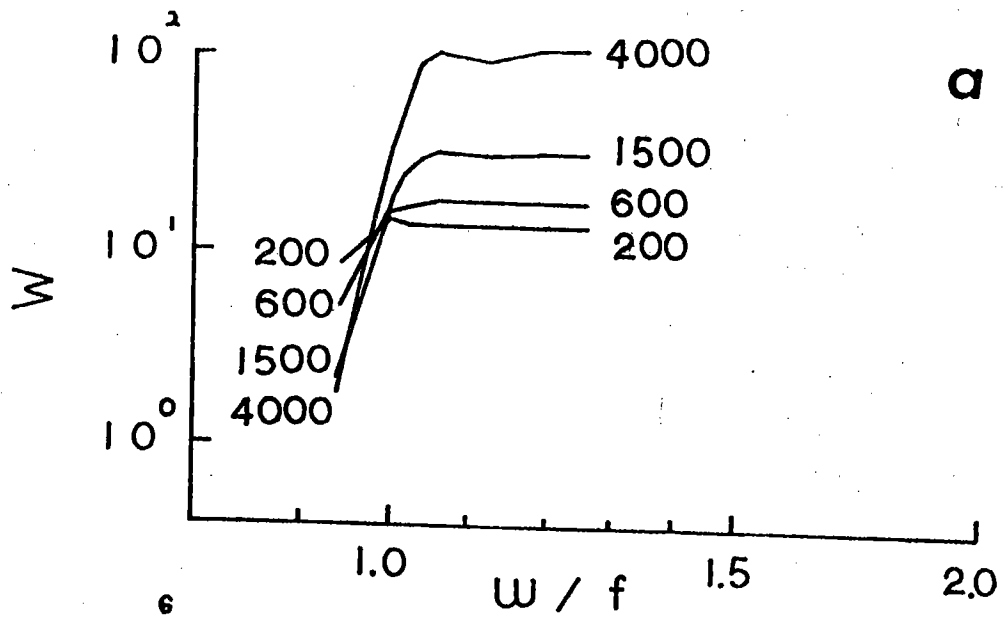
We first discuss the response spectrum for the case of surface forcing. With the arbitrary assumption that  $|\hat{W}_b|_{\phi_0}^2 = 1 \text{ cm}^2/\text{sec}^2/\text{cycle}$  per  $2\Omega$ , the spectra at different depths are shown in Figs. 5.4(a, b), 5.5(a, b), and 5.6(a, b) for  $L = 300 \text{ km}$ ,  $150 \text{ km}$ , and  $75 \text{ km}$  respectively. At sub-inertial frequencies, the response is trapped near the surface as expected. At super-inertial frequencies, the response is propagating downward with  $|\hat{V}|^2$  decreasing and  $|\hat{W}|^2$  increasing with depth. At frequencies sufficiently higher than  $f$ , the vertical variation scales in the WKBJ sense. In the velocity spectrum there is a peak slightly above  $f$  whose characteristics vary with depth and  $L$ : in general, its frequency increases and its strength (peak height) decreases with depth; its bandwidth decreases with  $L$ . For instance, at 200 m where the peak is strongest, the bandwidth and peak height (the latter is defined as the difference between the maximum power and the minimum power with  $\omega > f$ ) are listed in Table 5.3 for different values of  $L$ . The peak height is not particular dependent on  $L$  although the bandwidth is.

Table 5.3

Characteristics of the horizontal velocity spectra for different values of  $L$ .

$L$ (km)	peak height (db)	bandwidth
300	8.5	0.14
150	9.	0.09
75	9.	0.04

Figure 5.4 Response spectra of (a) w-velocity and (b) v-velocity at four different depths (numbers are in meters). The unit of the vertical axis is  $\text{cm}^2/\text{sec}^2/\text{cph}$ . The forcing is imposed at the surface ( $z_b = 0$ ) with  $L = 300$  km and  $\phi_0 = 36^\circ$ . A straight line representing the  $\omega^{-2}$  spectrum is drawn for reference.



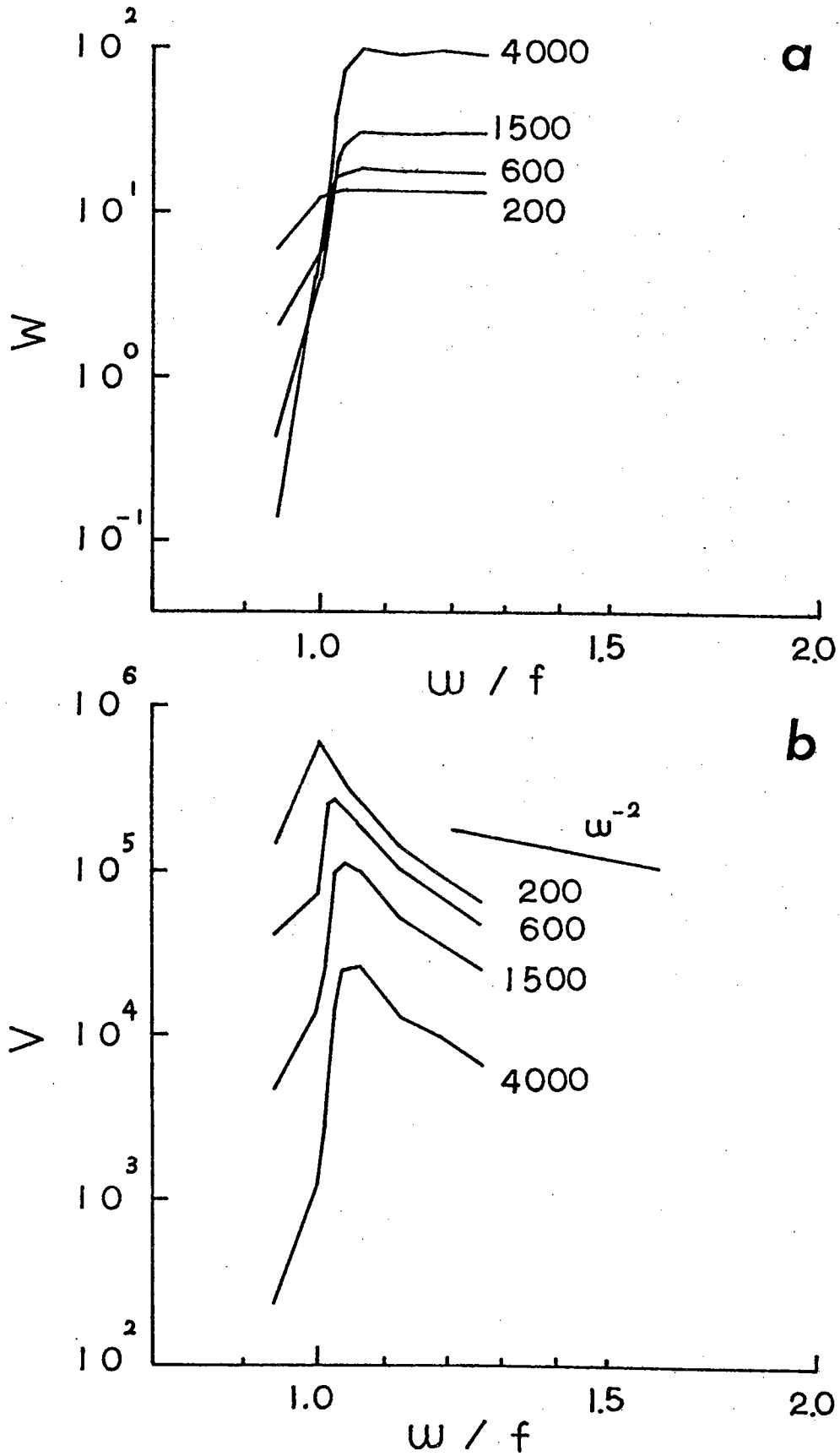


Figure 5.5 As in Fig. 5.4 except that  $L = 150$  km.

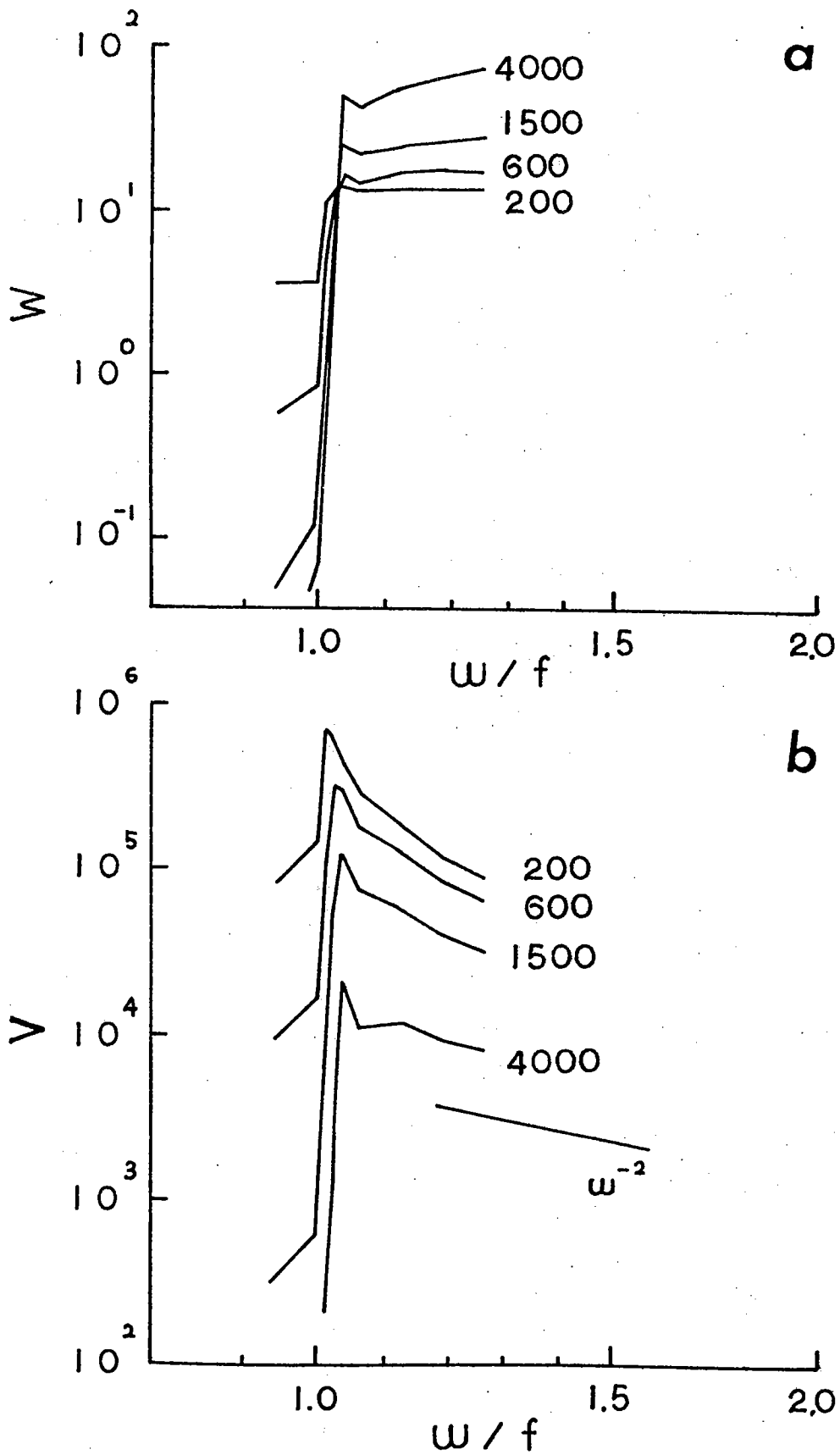


Figure 5.6 As in Fig. 5.4 except that  $L = 75$  km.

Now we can qualitatively explain why the observed spectra have stronger peaks and smaller blue shifts in the upper ocean (class 2a) than in the deep ocean over smooth topography (class 3). In the upper ocean, inertial waves are primarily locally forced as described by the model; hence the resulting peak frequency is indistinguishable from  $f$ , and the forced response is confined to the upper ocean. Together with the global wave spectrum whose shape is the same at all depths, the inertial peak is then stronger in the upper ocean. This interpretation can be illustrated by a schematic diagram, as shown in Fig. 5.7, of the ray paths of both the global and local wave field. Because of the nearly horizontal propagation of inertial waves, locally surface-generated waves will propagate away from their forced region before reaching the bottom; hence they can be measured only by instruments at shallow depths. On the other hand, globally generated waves can be measured at all depths. Therefore what the upper instrument measures is a combination of the local and global wave field, while the lower instrument only measures the global wave field. In the absence of the local wave field in the deep ocean, the significant blue shift there is accounted for by the global model (Chapter 4). [Because the upper ocean observations suggest that the bandwidth is less than  $0.1 f$ , we expect from Table 5.3 that small scale forcing is more important in producing the observed features.]

Can we interpret the dependence of the response spectrum on depth and  $L$  in terms of the properties of the excited waves? We have seen from Table 5.2 that considerably more high order negative modes are excited at near-inertial frequencies than super-inertial frequencies.



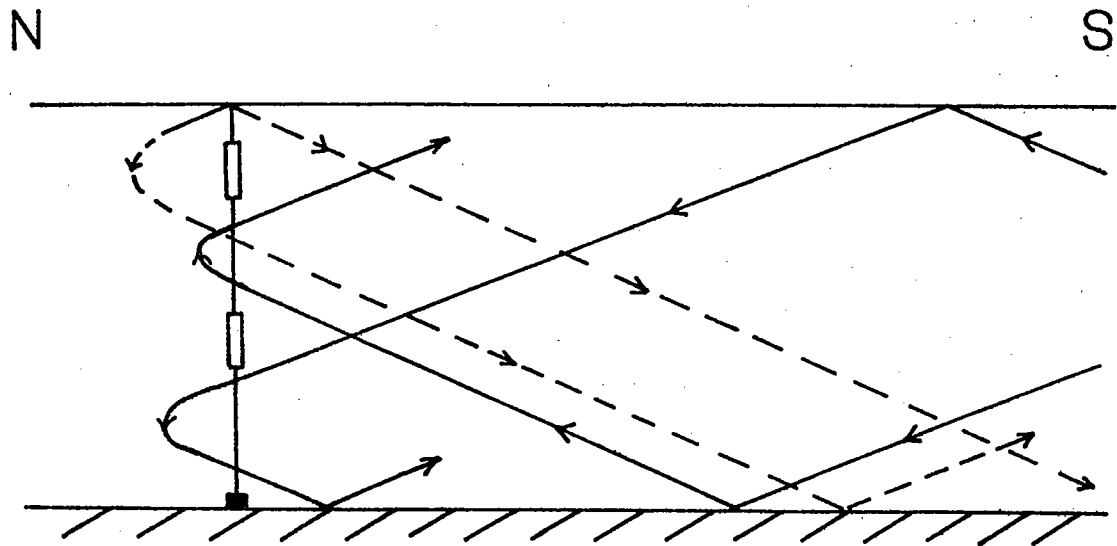


Figure 5.7 Schematic diagram showing the ray paths of the local wave field (dashed lines) and the global wave field (solid lines). A mooring with two current meters measuring the wave field is also shown.

For negative modes, the vertical structure is exponential (c.f. Eqs. (5.24), (5.25)) with trapping scale decreasing with increasing  $|\epsilon_n|$ . Therefore a substantial amount of the near-inertial wave energy is confined to small depths, but most of the super-inertial wave energy can penetrate to great depths. This is why the blue shift increases with depth. Moreover, because super-inertial waves are far from their turning latitudes, the wave amplitudes are only weakly dependent on frequency and the result of superposition has no prominent peaks. Hence with a white noise local forcing at the surface, there will be no prominent inertial peaks at great depths unless there is a global wave field.

The fact that the inertial peaks are stronger for smaller forcing scales can be explained as follows. As noted before, smaller scale forcing excites more high order modes; because high modes tend to interfere with each other more severely than low modes outside the inertial frequency band (see Chapter 4), the resulting peak will be stronger if there are more high modes involved.

Because the bandwidth of the inertial peak is controlled by the Airy frequency scale  $L_\sigma$  (c.f. Eq. (4.19)) which decreases with latitude, the latitudinal dependence of the response spectrum should be similar to that of the global wave spectrum as shown in Fig. 4.2. With  $L = 150$  km, the response spectrum was calculated at  $15^\circ$  and  $50^\circ$  to explore the latitudinal dependence. The results for the  $v$  component of velocity are shown in Figs. 5.8a and 5.8b; the results for the vertical velocity are not sensitive to latitude and are not shown here. As expected, the inertial peak is generally weaker at lower latitudes. At  $15^\circ$  the substantial response at sub-inertial frequencies results in the absence

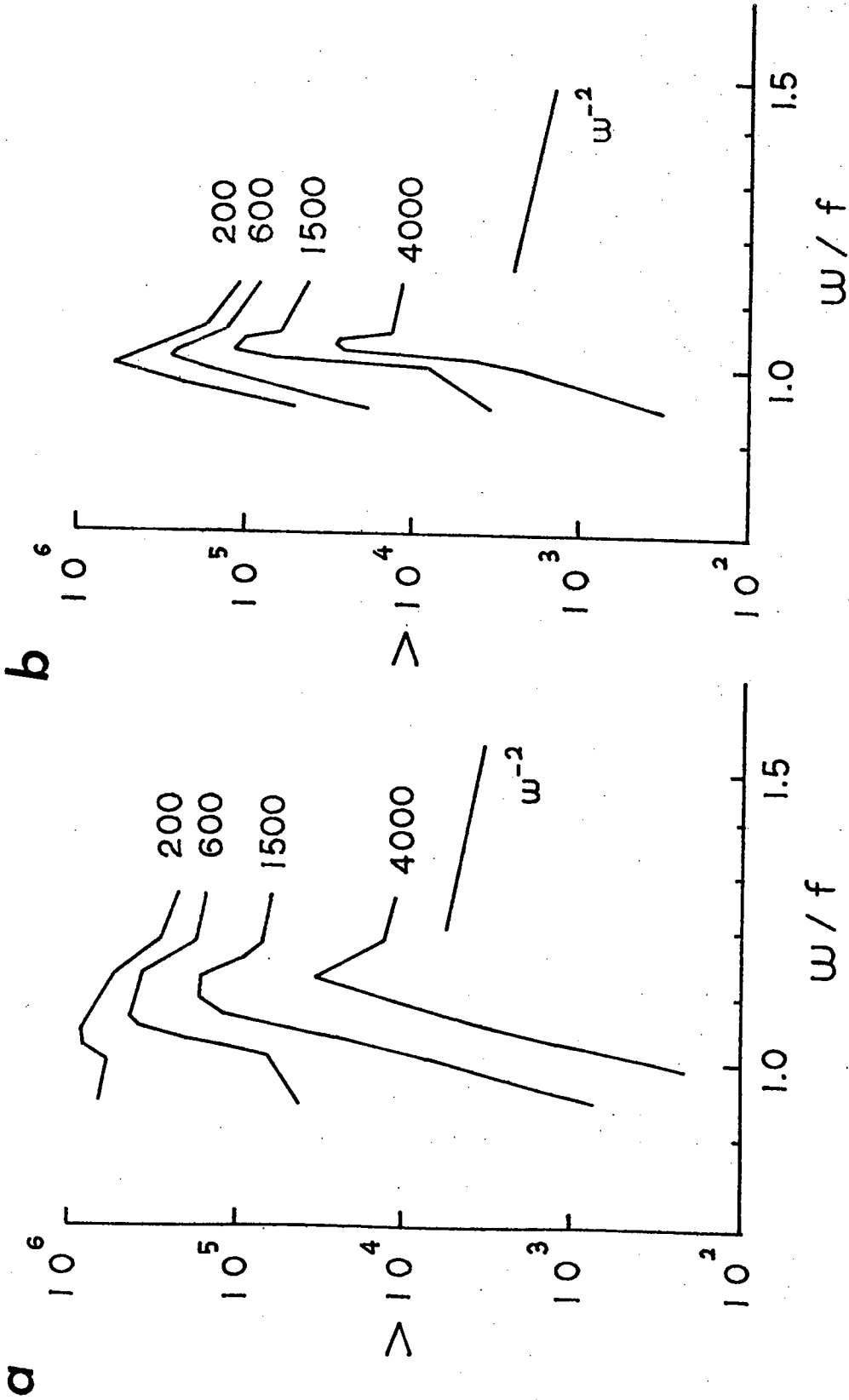


Figure 5.8 Response spectra of v-velocity at (a) 150 and (b) 500, with  $L = 150$  km.

of an inertial peak at 200 m. The large magnitudes of the blue shift reflect the character of equatorially trapped modes; recall the results of Eriksen (1979). At  $50^\circ$  the bandwidth is reduced to  $0.05f$ , and the sub-inertial energy is also greatly reduced. However, the peak energy level does not change much with latitude.

One way to estimate the possible forcing amplitude,  $|\hat{w}_b|_{\phi_0}^2$ , is to find the value of  $|\hat{v}|_{\phi_0}^2$  such that the energy level of  $|\hat{v}|^2$  near  $f$  is consistent with the upper ocean observations. For instance, by comparing the spectra at 200 m in Figs. 5.4b, 5.5b, and 5.6b with the observed spectra at 200m of the PMIII, we have  $|\hat{w}_b|_{\phi_0}^2 = 2 \times 10^{-3}$   $\text{cm}^2/\text{sec}^2/c.p.2\Omega$ , which yields a root mean square amplitude of  $w$  in  $[\sigma_1, \sigma_2]$  equal to  $2 \times 10^{-2}$  cm/sec. For a mixed layer 40 meters deep, this vertical velocity field could be produced by the convergence and divergence of surface inertial currents of amplitudes 50 cm/sec and wavelength 100 km. Another interesting quantity is the corresponding downward energy flux  $G$  which can be calculated as follows,

$$G = \int_{\sigma_1}^{\sigma_2} \frac{1}{2} \text{Real}(\hat{p} \hat{w}^*) \Big|_{z=0} d\sigma \quad (5.63)$$

With  $\hat{p}$  obtained from Eq. (5.9) we have

$$G = 9.3 \text{ erg/cm}^2\text{sec} \quad \text{for } L = 300 \text{ km,}$$

$$G = 3.2 \text{ erg/cm}^2\text{sec} \quad \text{for } L = 150 \text{ km.}$$

$$G = 1.3 \text{ erg/cm}^2\text{sec} \quad \text{for } L = 75 \text{ km}$$

The reason for the increase of  $G$  with  $L$  is that, larger scale forcing excites more low modes which have larger vertical group velocity. These numbers suggest that this forcing mechanism, if realistic, is an

important one for the internal wave field, which, with total energy  $4 \times 10^6$  erg/cm<sup>2</sup> (Garrett and Munk, 1972), can be set up in couple of weeks by this mechanism.

#### 5.4b Bottom forcing

The response spectra at 36° for bottom forcing with  $L = 150$  km are shown in Figs. 5.9(a, b). Now the sub-inertial response is trapped to the bottom, while the super-inertial response behaves the same way as in the case of surface forcing. The inertial peak is strongest at deep levels and the blue shift increases with height from the bottom (at  $z^* = -4500$  m). This explains why the observed inertial peak at deep levels over rough topography (class 2b) is as strong as that at upper levels (class 2a). In fact, what one would observe over rough topography is predominantly a local wave field with both surface and bottom sources, and the observed spectra is a superposition of the results shown in Figs. 5.9 and 5.5 with proper forcing amplitudes. By requiring that the modelled inertial wave energy levels be equal to the observed values, such a superposition is shown in Fig. 5.10. The spectral shape is basically the same at all depths, consistent with the observations over rough topography (see Fig. 2.3b). The dependence of the results on  $L$  and latitude is essentially the same as that for the case of surface forcing.

The forcing amplitude required at the bottom to produce the spectra shown in Fig. 5.10 is such that  $|\hat{w}_b|^2 = 8 \times 10^{-3}$  cm<sup>2</sup>/sec<sup>2</sup>/c.p. $2\Omega$ , corresponding to a root mean square vertical velocity of  $8 \times 10^{-2}$  cm/sec. The resulting vertical energy flux from the bottom to the interior is about 1.6 erg/cm<sup>2</sup> sec. Assuming that the energy source is

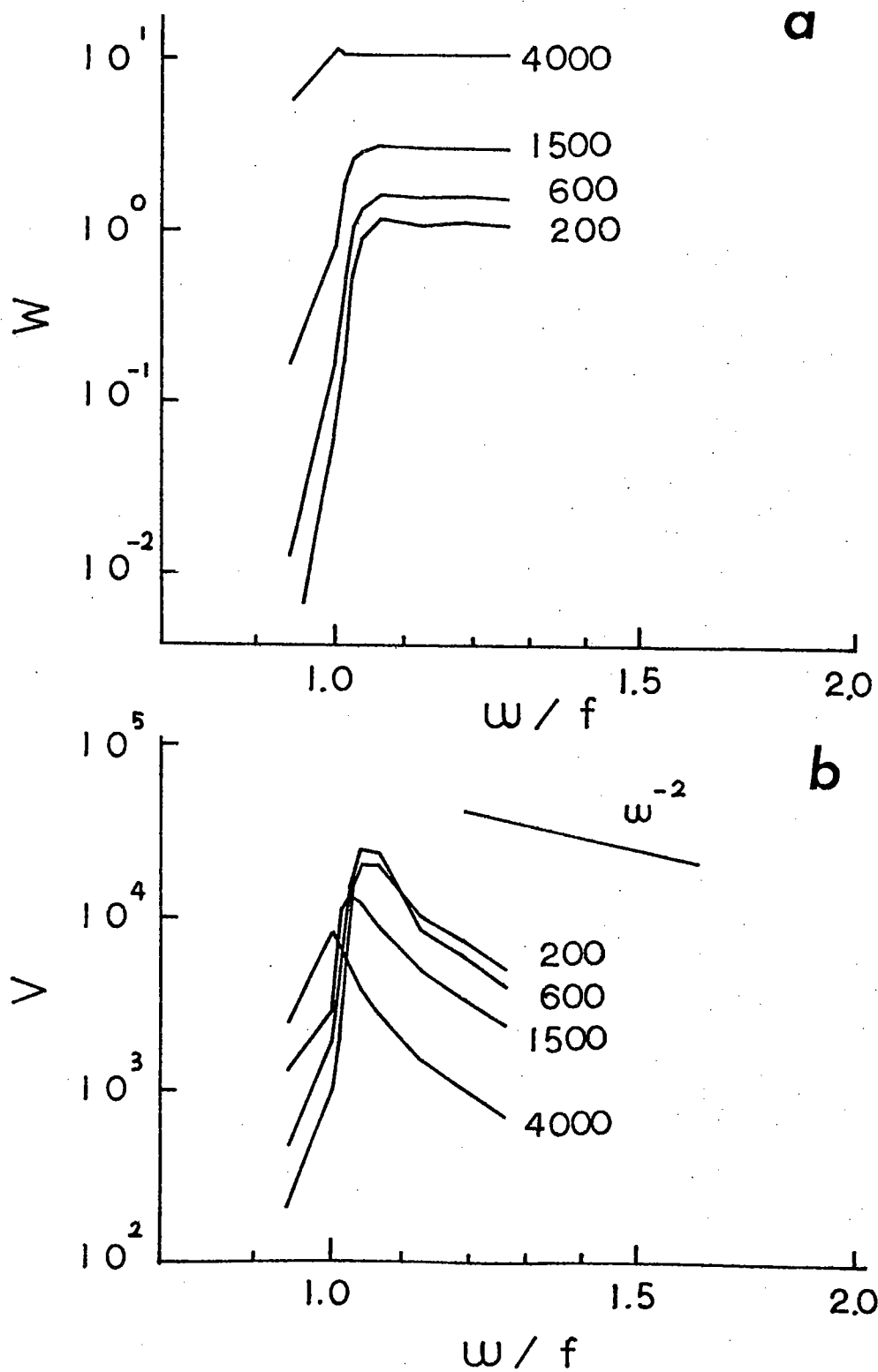


Figure 5.9 As in Fig. 5.4 except for bottom forcing ( $z_b = -1$ ) and  $L = 150$  km.

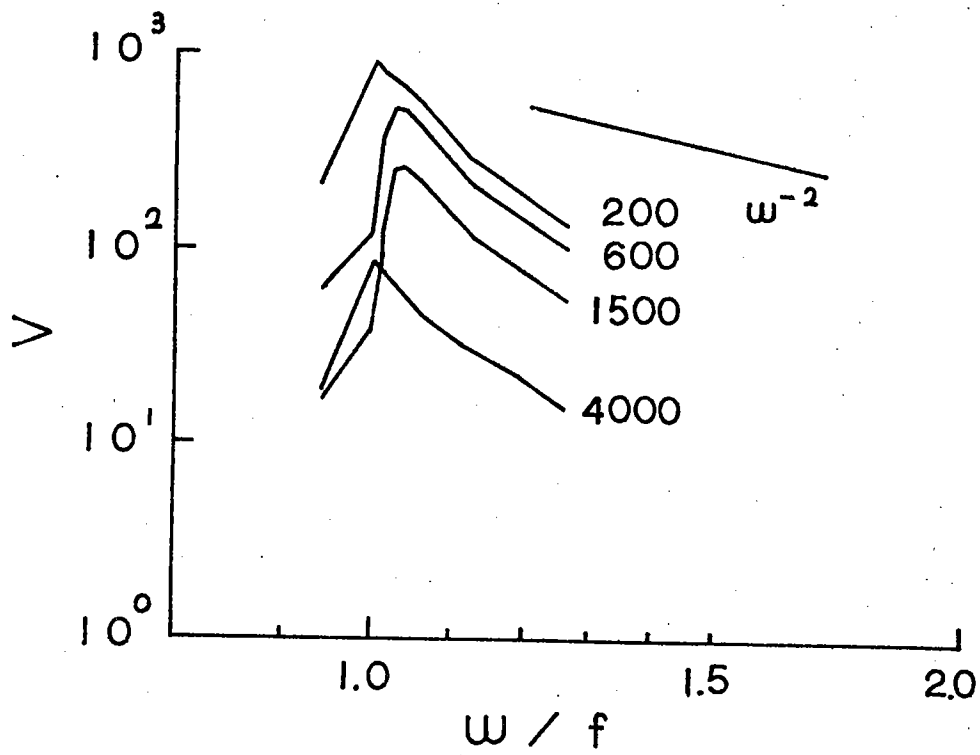


Figure 5.10 Response spectra of v-velocity with both surface forcing ( $|\hat{w}_b|^2 = 2 \times 10^{-3} \text{ cm}^2/\text{sec}^2/\text{c.p.}^2$ ) and bottom forcing ( $|\hat{w}_b|^2 = 8 \times 10^{-3} \text{ cm}^2/\text{sec}^2/\text{c.p.}^2$ ).

from the interaction between rough topography and a barotropic eddy with horizontal velocity amplitude of 5 cm/sec, it will take about 40 days to convert the eddy energy into internal wave energy. This result suggests that rough topography could be a potential sink (source) for eddy (internal wave) energy and explains why the observed eddy energy at great depths over rough topography is an order of magnitude less than that over smooth topography (Schmitz, 1978; Fu and Wunsch, 1979).

### 5.5 Summary and discussion

A forced model based on latitudinal modal decomposition is developed to study locally forced inertial waves. Asymptotic solutions of the LTE which are suitable for inertial waves are obtained and applied to the problem. The modal decomposition is cumbersome as expected of a localized function; however, it provides an accurate description of the transition of oceanic response from sub-inertial frequencies to super-inertial frequencies, a singular problem in the conventional  $f$ -plane model.

The forcing is through a specified vertical velocity field in a narrow band centered on  $f$  at the top and/or bottom boundaries. For surface forcing, the differences in the observed inertial wave spectra between upper ocean (class 2a) and the deep ocean over smooth topography (class 3) can be qualitatively described by the model. For bottom forcing, the strong inertial peaks observed in the deep ocean over rough topography (class 2b) also can be accounted for by the model.



The model results are dependent on forcing scale and latitude; the inertial peak is stronger for smaller forcing scale and/or higher latitude. In order to produce the observed energy level in the upper ocean, a downward energy flux with magnitude from 1.5 to 12  $\text{erg/cm}^2\text{sec}$  is required for forcing scale from 75 km to 300 km. Over rough topography with scale of 150 km, an upward energy flux of 1.6  $\text{erg/cm}^2 \text{ sec}$  is estimated.

## Chapter 6 The Reflection of Inertial Waves from the Benthic Boundary Layers

### 6.1 Introduction

The foregoing interpretation of the observed inertial wave energy over smooth topography as the combination of a vertically symmetric global wave field and a downward propagating local wave field is based on the crucial assumption that dissipation is negligible for the energy-containing low wavenumber components. If dissipation is substantial, then the waves are not able to propagate for great distance, and the energy balance is between local forcing at the surface and dissipation at the bottom. This is the interpretation proposed by Leaman (1976) for the observed dominance of downward energy propagation in profiler measurements. Displayed in Fig. 6.1 is a schematic diagram showing the difference between Leaman's interpretation and ours. Another assumption underlying Leaman's interpretation is that all the reflected wave energy can be measured by a local profiler. This would be the case if the wave field is horizontally homogeneous, which requires that the wave frequency be at least greater than  $1.15 f$ . However, as noted in Chapter 5, because ray paths are nearly horizontal for inertial waves (c.f. Eq. (5.2)), their reflections from the bottom occur at a great distance from their source region (see Fig. 5.7), and cannot be measured by a local instrument. Even for perfect reflections, the propagation of local inertial waves as observed by a profiler tends to be predominantly downward. Hence the reflection coefficient estimated by Leaman as the ratio of upward energy to downward energy observed in profiler measurements is likely an underestimate, and the observed appreciable amount of upward energy should be interpreted as part of the global wave field.

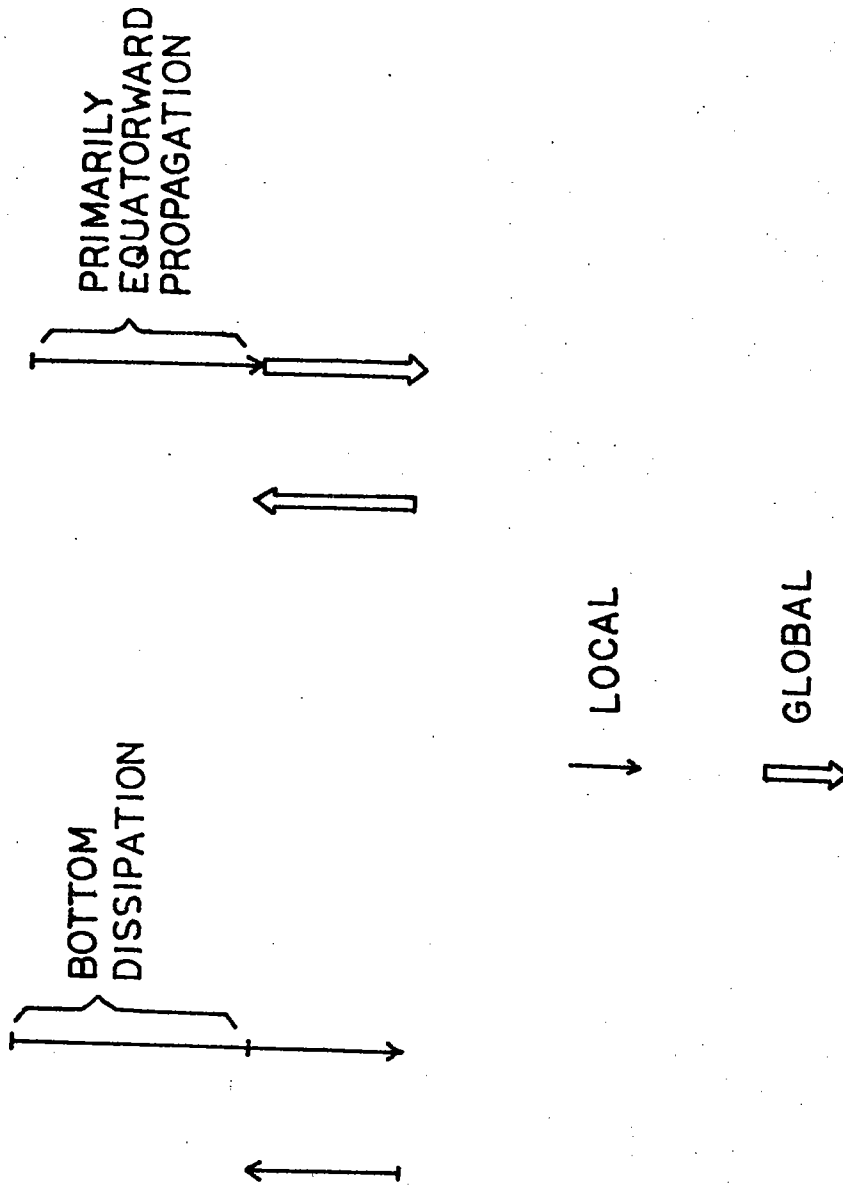


Figure 6.1 Schematic diagram showing two different interpretations of the observed dominance of downward energy propagation of inertial waves. The left figure is Leaman's (1976), and the right figure is ours. The arrow represents the direction of propagation and its length is proportional to the corresponding amount of energy.

Existing models for the reflection of inertial waves from rigid boundaries (e.g. Phillips, 1963; Leaman, 1975) usually assume a constant viscosity coefficient and solve for the Ekman boundary layer. For near-inertial frequencies, the resulting boundary layer depth is of the order of the ocean depth and the reflection coefficient is zero. However, this singular solution is not applicable to the real ocean for the following reasons: firstly, such an order-one viscous layer is not observed (e.g. large amplitudes at great depths are inconsistent with a viscous decay); secondly, the benthic mixed layer in which most dissipation occurs has been neglected. Recent observations (e.g. Armi and D'Asaro, 1979) suggest that near the bottom, a well-mixed boundary layer with depth a few tens of meters is quite common. For a review of theoretical models and earlier observations of this boundary layer see Wimbush and Munk (1970). The inclusion of this layer in the dynamics is important especially when dissipation is concerned. It is the purpose of this chapter to present a simple model for the reflection of inertial waves from the bottom in the presence of a benthic mixed layer. The major question is whether we can obtain a reflection coefficient comparable to that estimated by Leaman (1976).

## 6.2 The model

The benthic ocean is modelled as a uniformly stratified layer of infinite depth on top of a homogeneous layer of depth  $D$ . The existence of this mixed layer is assumed a priori; presumably it is maintained by turbulence produced in the shear zone near the bottom. Fig. 6.2 shows the model configuration. Wave packets come from infinity and reflect

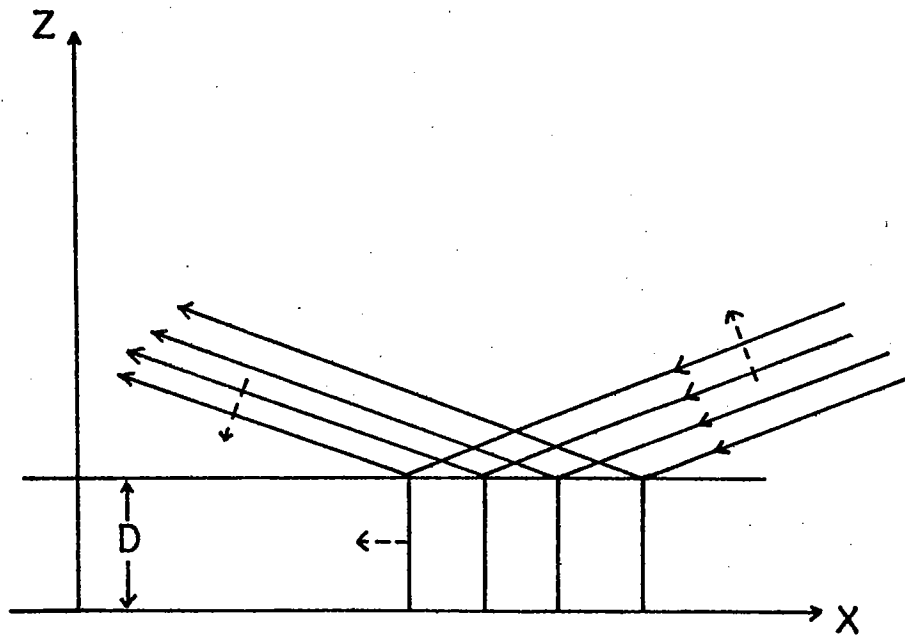


Figure 6.2 Schematic diagram of the model configuration. Solid arrows represent the ray paths and their directions of propagation; dashed arrows represent the directions of phase propagation.

back from the boundary layer. Because our major interests are the energy containing waves with low vertical wavenumbers, the viscous effects can be neglected in the interior. For instance, the wave Ekman number,  $\nu m^2/f$ , is  $O(10^{-4})$ , where  $\nu$  is the eddy viscosity ( $\sim 1 \text{ cm}^2/\text{sec}$ ),  $m$  is the vertical wavenumber ( $\sim 10^{-4} \text{ cm}^{-1}$ ), and  $f=7.27 \times 10^{-5} \text{ sec}^{-1}$ .

In the mixed layer, all the dynamic variables are nearly uniform in the vertical as the result of turbulent mixing (Armi and D'Asaro, 1979).

Hence the slab model used in the upper oceanic mixed layer (Pollard and Millard, 1970) and in the atmospheric boundary layer (Geisler and Kraus, 1969) can be applied here. The frictional drag produced at the bottom can be written as

$$\vec{\tau} = c_D |\vec{u}| \vec{u}, \quad (6.1)$$

where  $c_D$  is a drag coefficient which is hardly dependent on velocity at high Reynolds number;  $\vec{u}$  is the velocity vector, and  $|\vec{u}|$  is its magnitude. Then the effects of  $\vec{\tau}$  in the mixed layer is simply modelled as a uniform body force  $\vec{\tau}/D$ . Mean flow effects (including low frequency eddies) are not considered in this model; this is a serious restriction because the nonlinear drag law has been used to model frictional effects. However, for places in the mid-ocean where low frequency flow is weak, this model should be a zero order approximation.

The Boussinesq equations on an  $f$ -plane can be written

$$u_t - fv = -p_x \quad \} \quad (6.2)$$

$$v_t + f u = -p_y \quad (6.3)$$

$$u_x + v_y + w_z = 0 \quad \text{for } z > D, \quad (6.4)$$

$$0 = -p_z - \frac{\rho}{\rho_0} g \quad (6.5)$$

$$\rho_t - \frac{\rho_0}{g} N_b^2 w = 0 \quad (6.6)$$

and

$$u'_t - f v' = -p'_x - B u' \quad (6.7)$$

$$v'_t + f u' = -p'_y - B v' \quad (6.8)$$

$$u'_x + v'_y + w'_z = 0 \quad \text{for } D > z > 0, \quad (6.9)$$

$$0 = -p'_z \quad (6.10)$$

where

$$B = (u'^2 + v'^2)^{1/2} C_D/D, \quad (6.11)$$

$u$ ,  $v$ , and  $w$  are the east, north, and vertical velocity components,  $\rho_0$  = mean density,  $\rho$  = perturbation density,  $p$  = pressure/ $\rho_0$ ,  $N_b$  = buoyancy frequency,  $g$  = gravity; the primed variables are the corresponding ones in the mixed layer. The hydrostatic approximation is assumed in (6.5) and (6.10). At  $z = D$ , the matching conditions are

$$p = p' \quad (6.12a)$$

$$w = w' \quad (6.12b)$$

At  $z = 0$ , the boundary condition is

$$w' = 0 \quad (6.13)$$

Eqs. (6.2)-(6.13) are nonlinear because of the nonlinear dependence of  $B$  on  $u'$  and  $v'$ . However, for typical values  $C_D = 2 \times 10^{-3}$  (Wimbush and Munk, 1970),  $u' = 3 \text{ cm/sec}$  and  $D = 20 \text{ m}$  (Armi and D'Asaro, 1979), we have  $B = 3 \times 10^{-6} \text{ sec}^{-1}$ , which is only  $0.04 f$  at  $30^\circ$  latitude. Hence the linear wave solution should be a good zero order solution. Moreover, at near-inertial frequencies the horizontal particle speed,  $(u'^2 + v'^2)^{1/2}$ , of the zero order solution is independent of both time and space (properties of inertial waves). So we can simplify the equations by treating  $B$  as a constant, and seek wave solutions of the following form:

$$(u, v, \dots) = \text{Real}(\hat{u}, \hat{v}, \dots) \exp(i(kx \pm mz - \omega t)) \quad (6.14)$$

$$(u', v', \dots) = \text{Real}(\hat{u}', \hat{v}', \dots) \exp(i(kx - \omega t)) \quad (6.15)$$

where the hatted variables are complex amplitudes;  $k$  and  $m$  are the horizontal and vertical wavenumbers;  $\omega$  is the frequency. Assuming  $m > 0$ , then the upper sign in (6.14) corresponds to the incident (downward energy) waves and the lower sign to the reflected waves. Substituting (6.14) and (6.15) into Eqs. (6.2)-(6.10), we obtain

$$i\omega \hat{u} + f \hat{v} = ik \hat{p} \quad (6.16)$$

$$-i\omega \hat{v} + f \hat{u} = 0 \quad (6.17)$$



$$ik\hat{u} \pm im\hat{w} = 0 \quad \left. \vphantom{ik\hat{u} \pm im\hat{w} = 0} \right\} z > D \quad (6.18)$$

$$0 = \mp im\hat{p} - \frac{\hat{p}}{\rho_0} q \quad (6.19)$$

$$i\omega\hat{p} + \omega N_b^2 \frac{\rho_0}{q} = 0 \quad (6.20)$$

and

$$(B-i\omega)\hat{u}' - f\hat{v}' = -ik\hat{p}' \quad (6.21)$$

$$f\hat{u}' + (B-i\omega)\hat{v}' = 0 \quad \left. \vphantom{f\hat{u}' + (B-i\omega)\hat{v}' = 0} \right\} D > z > 0 \quad (6.22)$$

$$ik\hat{u}' + \hat{w}'_z = 0 \quad (6.23)$$

Differentiating (6.23) with respect to  $z$ , we have

$$\hat{w}'_{zz} = 0,$$

of which the solution satisfying (6.13) is

$$\hat{w}' = -ik\hat{u}'z \quad (6.24)$$

From (6.21) and (6.22) we obtain

$$\hat{u}' = \frac{-ik\hat{p}'(B-i\omega)}{(B-i\omega)^2 + f^2}, \quad \hat{v}' = \frac{ik\hat{p}'f}{(B-i\omega)^2 + f^2} \quad (6.25)$$

The matching conditions (6.12a) and (6.12b) become

$$\hat{p}' = \hat{p}_i e^{imD} + \hat{p}_r e^{-imD}, \quad (6.26a)$$

$$\hat{w}' = -ik\hat{u}'D = \hat{w}_i e^{imD} + \hat{w}_r e^{-imD}, \quad (6.26b)$$

where "i" and "r" represent the incident and reflected waves respectively. From (6.19) and (6.20) we have

$$\hat{P}_i = -\frac{N_b^2}{\omega m} \hat{W}_i, \quad \text{and} \quad \hat{P}_r = \frac{N_b^2}{\omega m} \hat{W}_r \quad (6.27)$$

Then from (6.26a), (6.26b), (6.25), and (6.27), the following expression is obtained:

$$Z \equiv \frac{\hat{W}_r}{\hat{W}_i} e^{-2imD} = \frac{m(\omega^2 - f^2)D(B - i\omega) - \omega[(B - i\omega)^2 + f^2]}{m(\omega^2 - f^2)D(B - i\omega) + \omega[(B - i\omega)^2 + f^2]} \quad (6.28)$$

where the dispersion relation

$$k^2 N_b^2 = m^2(\omega^2 - f^2)$$

has been used. The reflection coefficient  $r$  is defined as the ratio of the reflected energy flux to the incident energy flux, which is proportional to  $|\hat{W}_r|^2 / |\hat{W}_i|^2$ , so we have

$$r = |Z|^2$$

Because  $B$  is still unknown, another equation is needed to solve for  $Z$  in terms of the parameters of incident waves. From Eqs. (6.25)-(6.27) we obtain

$$\hat{u}' = \frac{-ik \hat{P}_i e^{imD} (B - i\omega)(1 - Z)}{(B - i\omega)^2 + f^2} ; \quad (6.29)$$

with the use of Eqs. (6.16) and (6.17) which yields

$$\hat{P}_i = \frac{\omega^2 - f^2}{\omega k} \hat{u}_i,$$

the following relation between  $\hat{u}'$  and  $\hat{u}_i$  is obtained:

$$\hat{u}' = \frac{-i(\omega^2 - f^2)(B - i\omega)e^{imD}(1-Z)}{\omega[(B - i\omega)^2 + f^2]} \hat{u}_i \quad (6.30)$$

In order to be consistent with the requirement that B be a constant, we must have

$$\frac{\hat{u}'}{\hat{v}'} = -i \quad (6.31)$$

As a consistency check of the solutions, we should test the validity of (6.31). From (6.25) we have

$$\frac{\hat{u}'}{\hat{v}'} = \frac{-B}{f} + i \frac{\omega}{f} \quad (6.32)$$

For  $B \ll f$  and  $\omega \approx -f$ , our solutions are self consistent. Therefore a consistent approximation for B can be written

$$B = \frac{C_D}{D} |\hat{u}'| \quad (6.33)$$

For given  $\hat{u}_i$ , Eqs. (6.28) and (6.30) then form a closed set of nonlinear algebraic equations with unknowns Z and  $\hat{u}'$ , which can be solved numerically using an iteration method.

### 6.3 Results

The model results are presented by showing r and d ( $\equiv |\hat{u}'|/|\hat{u}_i|$ ), the reflection coefficient and the ratio of the horizontal velocity in

the mixed layer to that of the incident wave, as functions of frequency with the other five model parameters --  $m$ ,  $D$ ,  $C_D$ ,  $N_b$ , and  $|\hat{u}_i|$  -- varying in their typical ranges. Instead of the vertical wavenumber  $m$ , we use its equivalent mode number  $j$  defined as

$$m = j \pi \hat{M} N_b / N_0 \quad (6.34)$$

where  $N_0 = 3$  cph,  $\hat{M} = 0.122 \times 10^{-3}$  cycle/meter. Eq. (6.34) expresses the relation between  $j$  and  $m$  above the mixed layer where we have assumed constant buoyancy frequency  $N_b$ , according to the  $N(z)$  used by Garrett and Munk (1972).

There are five cases to be discussed; in each case we vary only one parameter with the others fixed at the following reference parameters:  $j = 3$ ,  $D = 20$  m,  $C_D = 0.002$ ,  $N_b = 0.2$  cph,  $|\hat{u}_i| = 3$  cm/sec. The value for  $j$  is the mode number scale, i.e.,  $j_*$ , proposed by Cairns and Williams (1976) for the vertical wavenumber spectrum, corresponding to a 870 m wavelength in the thermocline. The values for  $N_b$  and  $|\hat{u}_i|$  are typical of the benthic ocean (D'Asaro, 1979; personal communication).

Fig 6.3 shows  $r$  and  $d$  as functions of  $\omega$  with different  $j$ . For  $\omega$ ,  $1.2 f$  is probably the upper bound for the validity of the solutions. First of all,  $r$  is greater than 0.9 for  $j \lesssim 20$ , where lies most of the energy of the vertical structure of inertial waves. Thus the estimate of Leaman (Fig. 13, 1976) --  $r \approx 0.6$  for 75 % of the energy -- cannot be accounted for by the model. When  $\omega = f$ , the vertical velocity of the incident waves vanishes in an  $f$ -plane model, so the mixed layer is

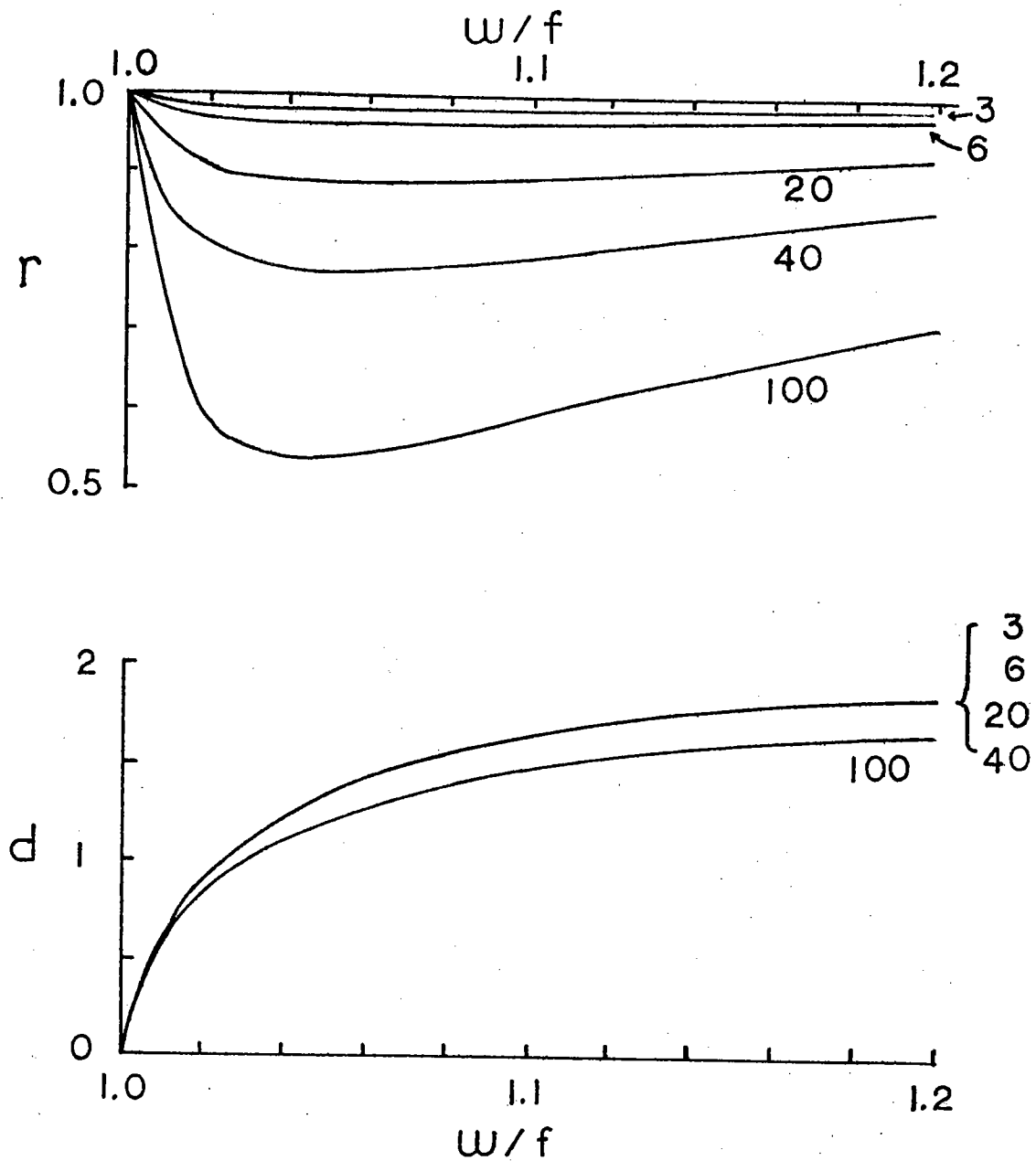


Figure 6.3  $r$  and  $d$  as functions of frequency for different values of vertical wavelength (labelling numbers are equivalent mode numbers).

decoupled from the interior, yielding  $|\hat{u}'| = 0$  and  $r = 1$ . When  $(\omega - f)$  increases,  $B$  becomes increasingly negligible in the denominator in (6.30); hence  $|\hat{u}'|$  increases toward its inviscid limit  $2 |\hat{u}_i|$  for  $mD \ll 1$ . For  $\omega \gtrsim 1.04 f$ , both  $d$  ( $\equiv |\hat{u}'| / |\hat{u}_i|$ ) and the dissipation rate,  $C_D |\hat{u}'|^3$ , increase very slowly; the slight increase of  $r$  with  $\omega$  can then be explained by the rapid increase with  $\omega$  of the vertical group velocity, yielding a rapid increase of the dissipation rate for fixed  $r$ , therefore  $r$  has to increase with  $\omega$  at a rate which makes the dissipation rate change slowly as shown in Fig. 6.3. Similarly the decrease of  $r$  with increasing  $m$  also can be explained by the decrease of the vertical group velocity with increasing  $m$  and the insensitivity of  $d$  (hence the dissipation) to  $m$ . Recall that the vertical group velocity can be written

$$\frac{\partial \omega}{\partial m} = \frac{-(\omega^2 - f^2)}{\omega m} = \pm \frac{(\omega^2 - f^2)^{3/2}}{\omega k N} \quad (6.35)$$

Is the result of nearly perfect reflection at small  $j$  sensitive to the particular model parameters used? Fig 6.4 shows the sensitivity of the model results to the mixed layer depth  $D$ . Note that the scale for the  $r$ -axis has been changed -- from 0.5-1. in Fig. 6.3 to 0.9-1. For typical range of  $D$  observed in the ocean -- from 5 m to 60 m (Armi and D'Asaro, 1979),  $r$  varies only in a narrow range from 0.94 to 1. Because  $B$  (frictional effects) decreases with increasing  $D$ ,  $d$  is closer to the inviscid limit for larger  $D$ , resulting in smaller  $r$ .

Fig 6.5 shows the sensitivity to  $N_b$ , the buoyancy frequency above the mixed layer. For a rather unlikely large value,  $N_b = 0.8$  cph, the

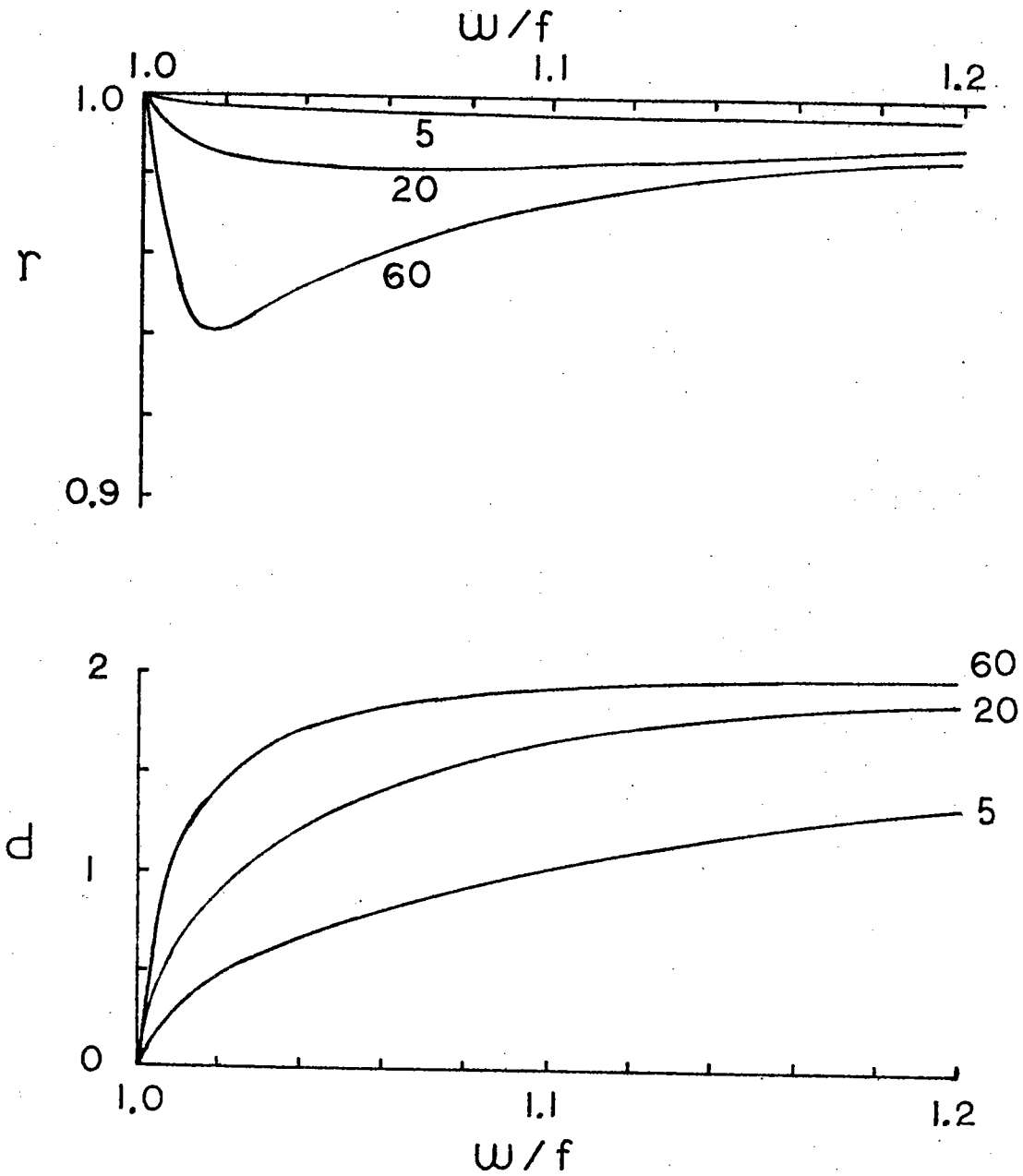


Figure 6.4 As in Fig. 6.3 except for different values of the mixed layer depth  $D$  (numbers are in meters).

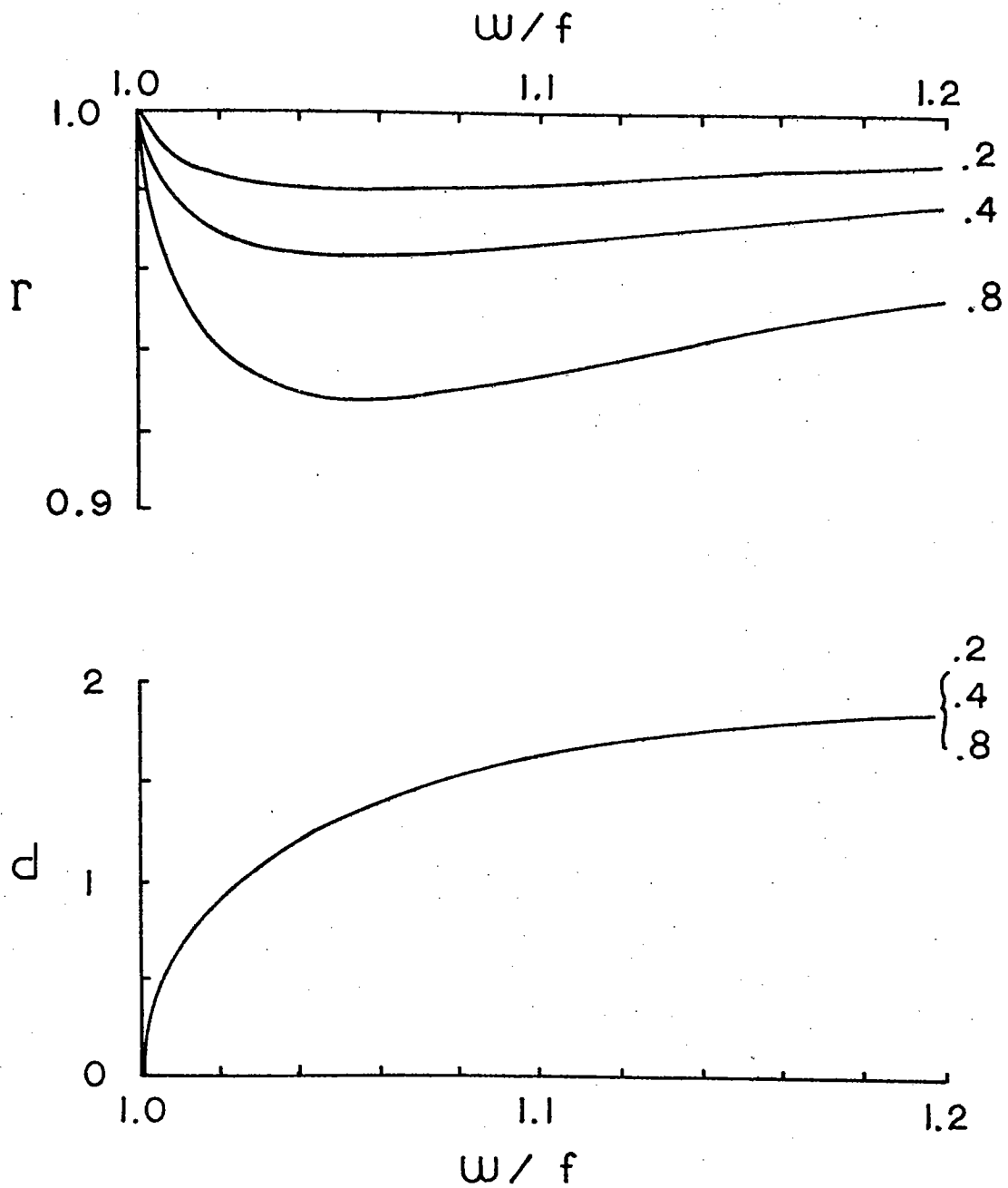


Figure 6.5 As in Fig. 6.3 except for different values of the buoyancy frequency  $N_b$  (in cph) on top of the mixed layer.



lowest value of  $r$  is about 0.93. The behavior of  $d$  does not change with  $N_b$  at all -- the same as in Fig. 6.4 with  $D = 20$  m. The decrease of  $r$  with increasing  $N_b$  is caused by the increase of vertical group velocity with  $N_b$  (c.f. Eq. (6.35)).

Fig. 6.6 shows that  $r \gtrsim 0.99$  is essentially insensitive to the drag coefficient  $C_D$  in the range 0.002- 0.01; the typical range of  $C_D$  in the benthic ocean is from 0.002 (smooth bottom) to 0.005 (rough bottom) (Wimbush and Munk, 1970). As expected,  $d$  decreases with increasing  $C_D$ . The crossings of the  $r$  curves at intermediate frequencies can be explained by the following relation:

$$(1 - r) \propto C_D d^3 |\hat{u}_i| \quad (6.36)$$

For different values of  $C_D$ , the behavior of the corresponding  $r$  could be different from that of  $d$ .

The behavior of  $r$  for different values of the incident wave velocity  $|\hat{u}_i|$  (Fig. 6.7) is pretty much the same as that shown in Fig. 6.6, because  $|\hat{u}_i|$  plays the same role as  $C_D$  in Eq. (6.36). Smaller  $|\hat{u}_i|$  induces smaller  $|\hat{u}'|$  and hence smaller frictional effects, so  $d$  is larger for smaller  $|\hat{u}_i|$  as shown.

#### 6.4 Summary and discussion

A simple model has been developed to calculate the reflection coefficient of inertial waves in the presence of a well mixed bottom boundary layer. The interior dynamics is assumed to be inviscid. The mixed layer is modelled as a slab and the frictional drag at the bottom

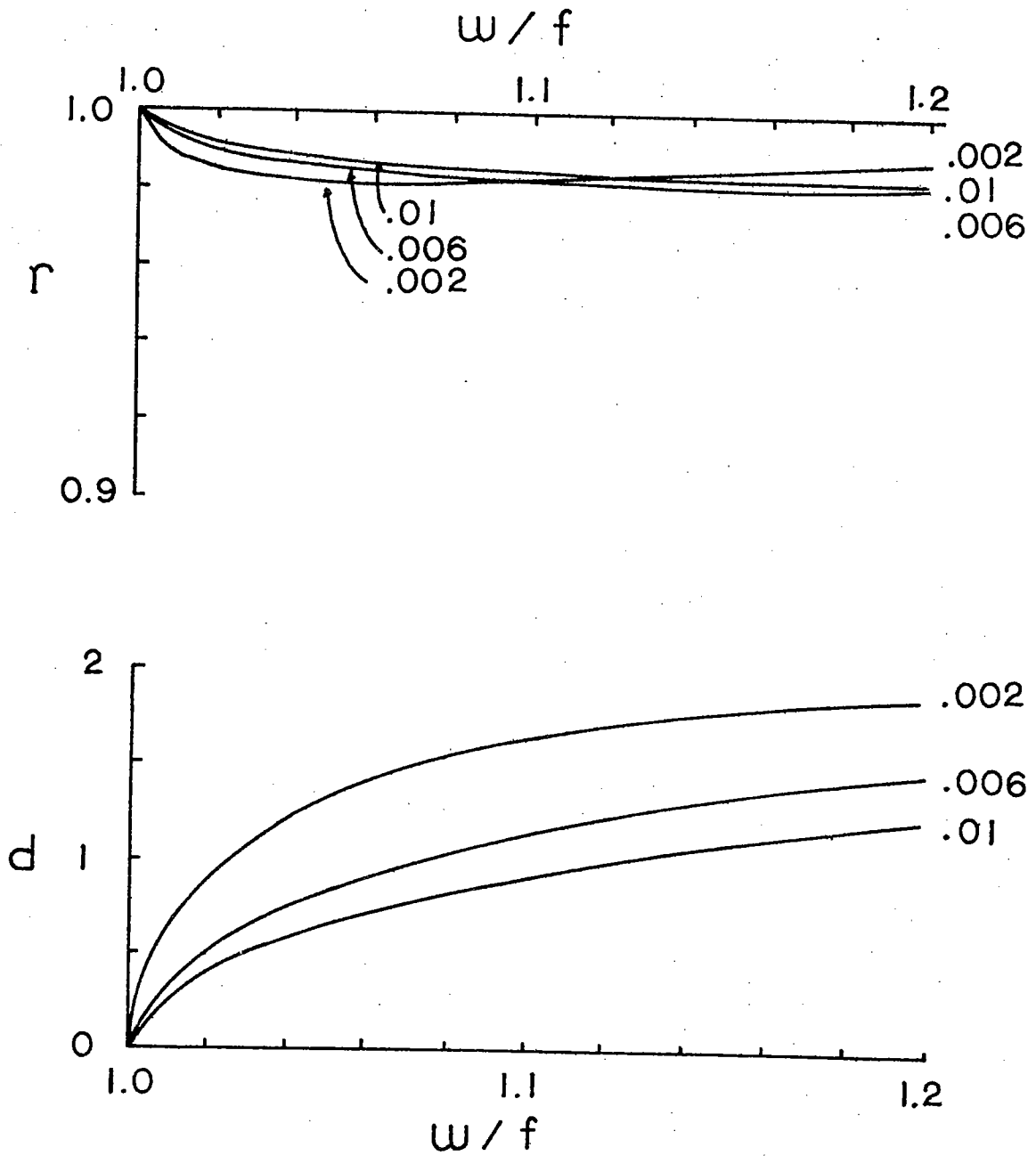


Figure 6.6 As in Fig. 6.3 except for different values of the drag coefficient  $C_D$ .

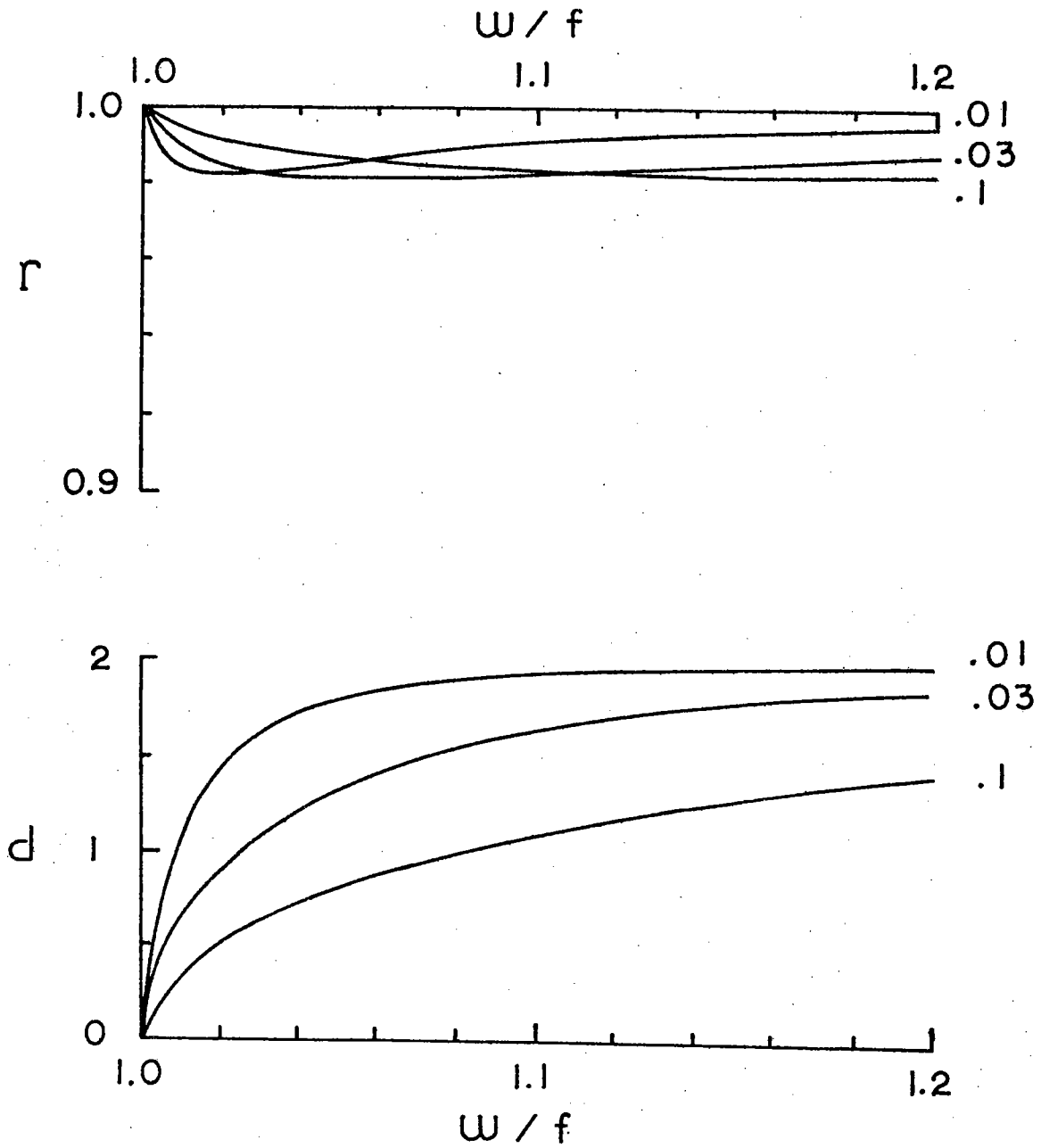


Figure 6.7 As in Fig. 6.3 except for different values of the incident wave amplitude  $|\hat{u}_i|$  (in m/sec).

is quadratic in the horizontal wave speed. An approximate wave solution has been obtained with error of order  $\max. \left( \frac{C_D}{D} \frac{|\hat{u}'|}{f}, \frac{(\omega-f)}{f} \right)$ , where  $C_D$  = drag coefficient,  $D$  = boundary layer depth,  $|\hat{u}'|$  = wave amplitude in the boundary layer. For typical conditions in the benthic ocean, the resulting reflection coefficient is generally greater than 0.9 for waves with equivalent mode number less than 20, and the results are not sensitive to model parameters. The relatively low values estimated by Leaman (1976) cannot be accounted for by the model.

Because of the nonlinearity introduced by the friction law, we cannot superpose wave solutions. However, the observed vertical wavenumber spectrum is dominated by low wavenumber components; our results for low wavenumber waves should be fairly representative. The existence of inertial waves in the benthic boundary layer and its high coherence with those above (Armi and D'Asaro, 1979) suggest that the effects of low frequency flow on inertial waves through nonlinear frictional effects are probably not important. The model results are then a valid zero order description; however, a numerical model including a mean flow would be necessary to verify this speculation. That the reflection coefficient is near unity is consistent with the existence of a global inertial wave field as described in Chapter 4.

## Chapter 7 Conclusions

Our work can be summarized as a spectral description of inertial waves observed in the Western North Atlantic from subtropical to temperate latitudes, and an attempt to interpret it in terms of the proposed models of the global and local wave field.

The observations presented in Chapter 2 suggest that a universal frequency spectrum does not exist near the inertial frequency  $f$ , where the spectral shape is very sensitive to the local environment. In most of the data, there is a prominent inertial peak slightly above  $f$  in the horizontal velocity spectrum as previously described; however, the peak height above the background continuum varies with instrument depth and geographical environment. According to the peak height, three classes of environment and their corresponding spectra emerge: class 1 is the 1500 m level near the Mid-Atlantic Ridge, with the greatest peak height of 18 db; class 2 includes (a) the upper ocean (depth less than 2000 m), (b) the deep ocean (depth greater than 2000 m) over rough topography, and (c) the deep ocean underneath the Gulf Stream, with intermediate peak height of 11.5 db; class 3 is the deep ocean over smooth topography, with the lowest peak height of 7.5 db. In the inertial frequency band, the estimated horizontal coherence scale is  $O(60 \text{ km})$  at depths from 200 m to 600 m, and probably less than this value at great depths. The order of magnitude is consistent with the theory of Munk and Phillips (1968). The estimated vertical coherence scale is  $O(200 \text{ m})$  just below the main thermocline, resulting in a wavenumber band in close agreement with the result of Cairns and Williams (1976).

A model spectrum for the global wave field is developed in Chapter 4

based on the wave functions obtained by Munk and Phillips (1968) and the assumption that the frequency-wavenumber spectrum is given by the GM model at lower latitudes. The most significant result of our work perhaps is the success of the global wave model in describing the observations of class 3. Both the energy level and the height of the observed inertial peak are well-described by the model. The amount of the blue shift of the inertial peak predicted by the model is dependent on the zonal wavenumber band. To be consistent with the observed blue shifts, zonal wavelengths are required to be less than  $O(90 \text{ km})$ . The observed frequency bandwidths of the inertial peak are slightly larger than the model results due to the kinematic effects of low frequency motions; however, their latitudinal dependence is consistent with the model. The latitudinal limits of the validity of the model is roughly from  $10^\circ$  to  $68^\circ$ .

For the observed spectra of class 1 and class 2, the excess inertial wave energy above what the global model predicts is interpreted as the result of local forcing. In the upper ocean, the most likely local forcing is from the mixed layer and the forced waves transfer energy downward. With this assumption, we have estimated a budget for downward and upward travelling energy which is in close agreement (10 % difference) with a recent estimate of Sanford. To make the idea of local forcing more concrete, a forced model is developed in Chapter 5 based on the latitudinal modal decomposition of a localized forcing function using the asymptotic eigensolutions of the Laplace's tidal equation. The forcing is through a vertical velocity field specified at the top and/or bottom boundaries. For surface forcing, major characteristics of the

class 2a spectra can be qualitatively described by the model. For bottom forcing, the resulting spectra show prominent inertial peaks at deep levels, consistent with observations over rough topography (class 2b). The estimated vertical energy flux from local sources to the interior suggests that both the surface and bottom sources are fairly efficient to generate inertial waves; the total internal wave energy could be set up in couple of weeks. If the bottom source is from typical mid-ocean eddies, the resulting "spin-down" time scale for the eddies is about a month.

In order that energetic low mode waves can propagate over great distance to form the global wave field, dissipation rates must be very small for these waves. A model is proposed in Chapter 6 to study the reflection of inertial waves from the benthic boundary layer, which is turbulent and homogeneous and hence can be modelled as a slab. Frictional effects are confined to this boundary layer and modelled by a quadratic drag law. For given incident waves, reflection coefficients are calculated. For waves with equivalent mode number less than 20, which contain most of the energy, the reflection coefficient is greater than 0.9 and increases with decreasing mode number. This is inconsistent with Leaman's estimate ( $\approx 0.6$ ; 1976) from the difference between downward and upward travelling energy as measured by velocity profilers. From the geometry of the ray paths of locally surface-forced waves, it can be shown that most of the reflected waves cannot be measured by a local profiler. Hence the interpretation that the excess downward travelling energy measured by profilers is primarily dissipated in the bottom boundary layer is misleading.

In summary, among the different classes of observations, we have successfully interpreted class 3, class 2a, and class 2b. In order to explain the observations of class 1, interactions between the Mid-Atlantic Ridge and low frequency motions which is the only apparent energy source available at intermediate and deep levels, must be adequately modelled. Time dependent models like Bell's (1975) are possible approaches. In addition to the huge inertial peaks, other features of the class 1 spectrum are also interesting: huge  $M_2$  tidal peak, prominent super- $M_2$  tidal peaks, small spectral slope and excess high frequency energy. Are these caused by the topographic effects of the Mid Atlantic Ridge ? When the moorings of the PMIII were deployed, a discontinuity in water mass was found in the cluster B area (Joyce, 1977). Is this frontal feature dynamically important ? Some theoretical work is needed here.

Concerning the strong inertial peaks found underneath the Gulf Stream (class 2c), observations at upper levels are important to determine the nature of the forcing. But the maintenance of moorings within the core of the Gulf Stream is still beyond the current capability of mooring technology. Theoretical work on the interactions between inertial waves and strong time dependent current would be illuminating.



Appendix A Temperature Spectra in the Inertial Frequency Band

The occurrence of apparent inertial peaks in observed temperature spectra as shown in Fig. 4.11 is not universal in the data examined. For instance, Fig. A.1 shows the temperature spectra at Stations 1 (3500 m) and 7 (600 m) of the PMII, where no prominent peaks show up near  $f$ ; however, prominent inertial peaks were observed at the 4000 m depth of Station 7 and at the same depth of Station 3 (see Fig. 4.11) which was only 30 km north of Station 1. We have not found any correlation between the occurrence of the temperature inertial peaks and their physical environment except that, there is always a strong temperature inertial peak at all depths of those stations roughly along  $28^{\circ}\text{N}$ . Because the diurnal tidal frequencies are so close to the local inertial frequency there, the observed temperature peaks are probably due to tidal motions. Elsewhere, the occurrence of temperature peaks is essentially unpredictable. We hereby investigate two possible mechanisms to account for their occasional occurrence.

As shown in Fig. 4.11, the observed inertial peaks in the temperature spectra are not consistent with the global wave model which, on the other hand, is consistent with the corresponding observed velocity spectra. For frequencies near  $f$ , the motion of free linear waves is nearly horizontal, and there should be no appreciable temperature fluctuations if the temperature gradient is essentially vertical. However, in the presence of meso-scale eddies, appreciable horizontal temperature gradient could exist in the mid-ocean occasionally; when advected by large horizontal inertial currents, it

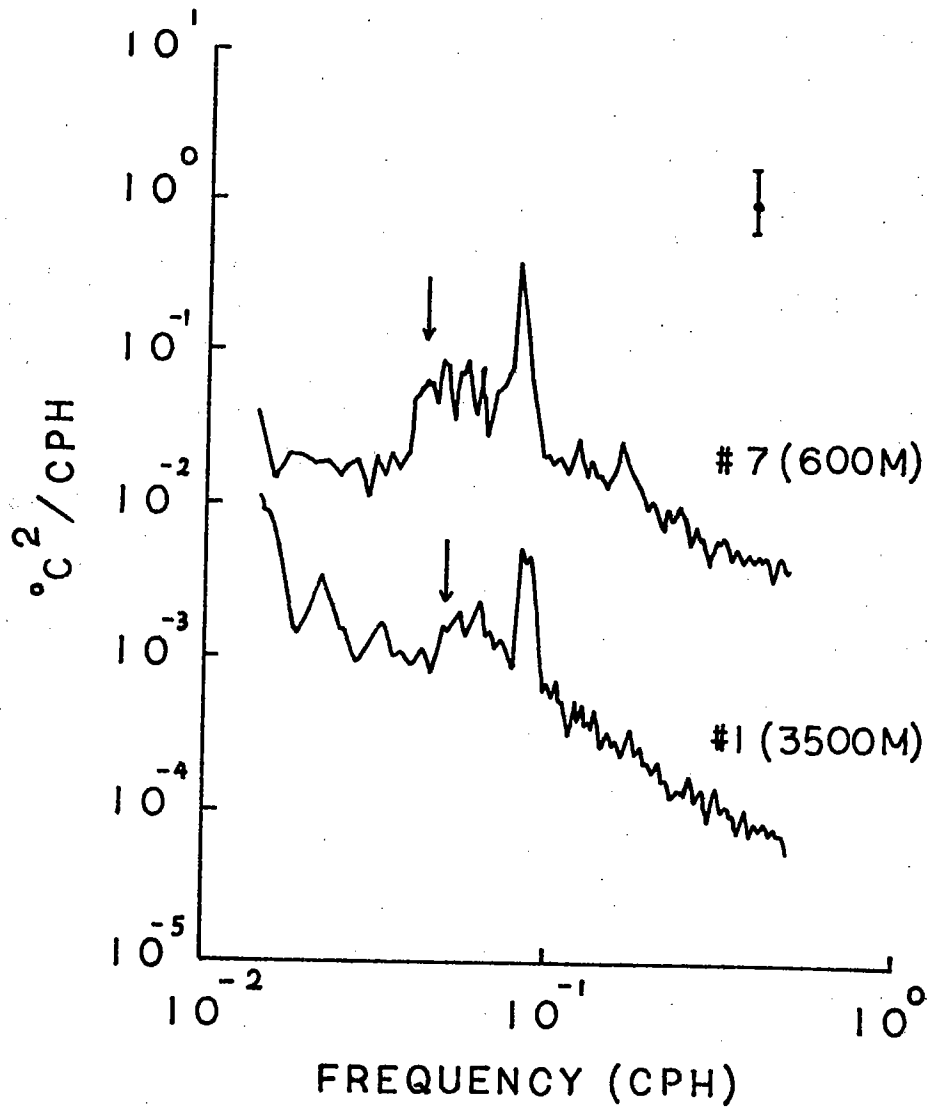


Figure A.1 Temperature spectra at 600 m at Station 1 ( $36^{\circ}\text{N}$ ,  $55^{\circ}\text{W}$ ), and at 3500 m at Station 7 ( $31.6^{\circ}\text{N}$ ,  $55^{\circ}\text{W}$ ) of the PMII. Arrows showing the location of the local  $f$ ; error bar showing the 95 % confidence interval.

could produce appreciable temperature signals with near inertial frequencies. The possibility that this mechanism accounts for the observed temperature peaks is discussed in Section A.1.

It is well-known that moored temperature measurements are subject to contamination caused by vertical mooring motion. Pressure spectra measured by TP recorders (Wunsch and Dahlen, 1974) show fairly strong inertial peaks, indicating strong vertical mooring motion in the inertial frequency band. A typical pressure spectrum is shown in Fig. A.2. Possible effects of this mechanism on observed temperature spectra are discussed in Section A.2.

#### A.1 Advection of horizontal temperature gradient by inertial waves

The propagation of internal waves in the presence of a baroclinic mean flow was investigated by Mooers (1975). For low frequency waves, he showed that the combined effect of mean shear and its resulting horizontal density gradient was to extend the free wave frequency band to an anomalous low frequency limit. It can be shown that this low frequency limit is at most a few percent lower than the local  $f$  for typical mid-ocean conditions, and that the characteristics of velocity solutions are only slightly modified by the mean flow. However, the density (or temperature) solutions are seriously affected by the presence of a horizontal density gradient. Assuming that all the field variables are independent of  $y$ , the temperature equation can be written

$$T_t + u \frac{\partial \bar{T}}{\partial x} + w \frac{\partial \bar{T}}{\partial z} = 0, \quad (\text{A.1})$$

where  $\bar{T}$  is the mean temperature field. For wave motion with frequencies

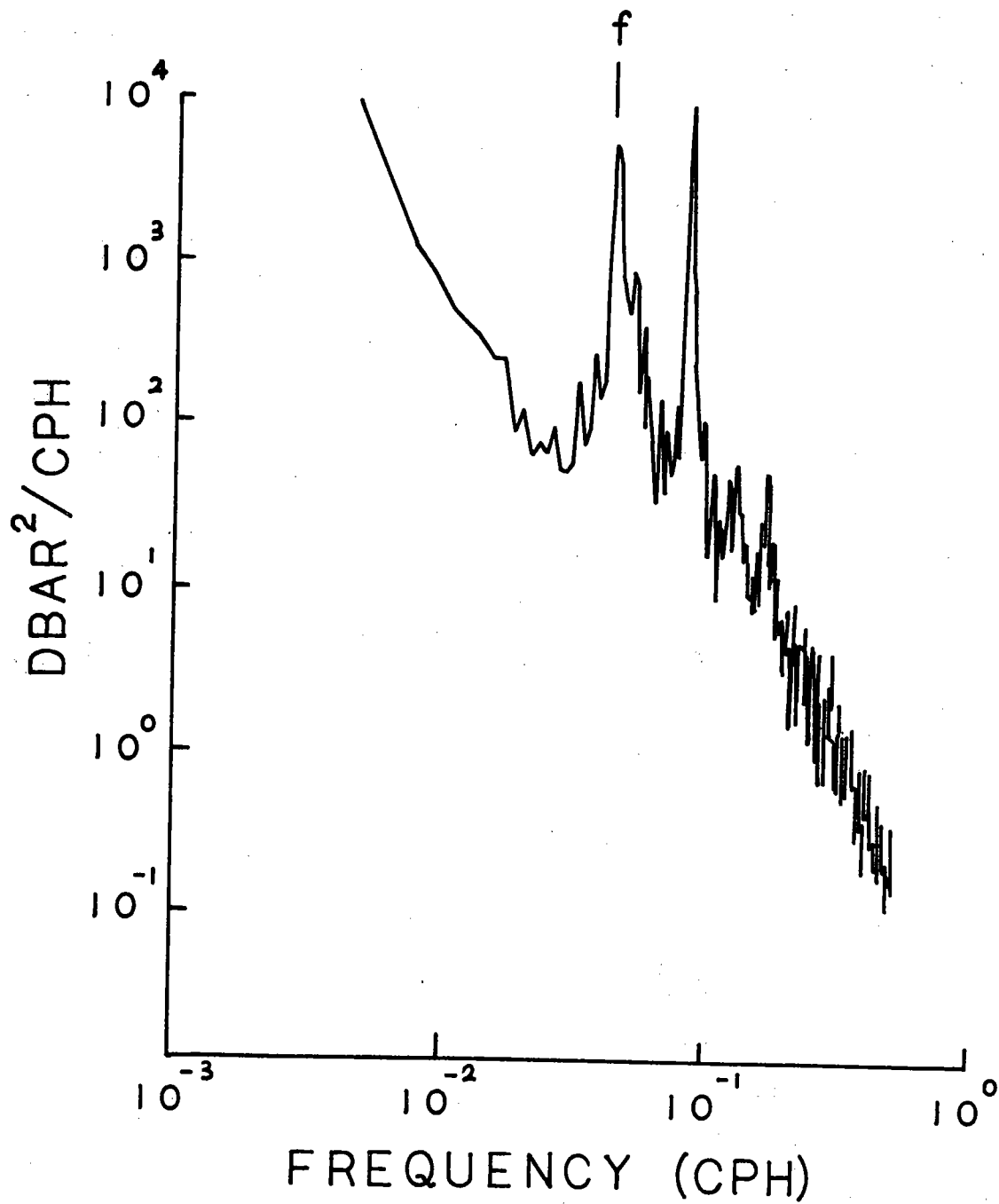


Figure A.2 Pressure spectrum of Record 5482 (31°N, 60°W) at 800 m.

near  $f$ , it can easily be shown that the horizontal advection dominates the vertical advection. Then the temperature spectral shape is the same as that of the horizontal velocity, having an inertial peak. The amplitude of the temperature fluctuation,  $\overline{T'^2}^{1/2}$ , can be estimated as the product of  $\left| \frac{\partial \bar{T}}{\partial x} \right|$  and the radius of inertial circle,  $u_0/f$  ( $u_0$  is a typical horizontal speed of inertial waves). For a typical mid-ocean eddy,  $\left| \frac{\partial \bar{T}}{\partial x} \right|$  in the main thermocline is about  $3 \times 10^{-2}$  deg.C/km (see MODE-1 Atlas Group, 1977). With  $u_0 = 10$  cm/sec and  $f = 7.27 \times 10^{-5}$  sec $^{-1}$ , we have  $\overline{T'^2}^{1/2} \sim 0.04$  deg.C, which is within order of magnitude of the observed values in the main thermocline (c.f. Table A.1, which shows the values for some strong temperature peaks). Therefore this mechanism could, to some extent, explain the observed inertial peaks in temperature spectra.

#### A.2 Mooring motion in the inertial frequency band

If the observed temperature signals are solely caused by the vertical mooring motion, we should have

$$T_t + P_t \frac{\partial T}{\partial p} = 0 \quad (\text{A.2})$$

For a linear vertical temperature gradient, which is approximately the case for small vertical excursions, we should have significant coherence between  $T$  and  $P$  with  $180^\circ$  phase difference. The  $T$ - $P$  coherence was calculated for a great number of stations, and significant coherence with  $180^\circ$  phase difference in the inertial band was found only at those stations where the mooring motion was relatively strong. At these

stations, the temperature spectra indeed have strong inertial peaks. It seems that strong mooring motion is a sufficient (but not necessary) condition for the occurrence of temperature inertial peaks. To test whether the observed temperature peaks are indeed caused by mooring motion, we have calculated for four selected stations the root mean square amplitudes of both temperature and pressure fluctuations in the inertial frequency band, denoted by  $\overline{T'^2}^{1/2}$  and  $\overline{P'^2}^{1/2}$  respectively, and also calculated the corresponding local temperature gradient  $dT/dp$  from CTD casts. By comparing  $\overline{T'^2}^{1/2}$  with  $dT/dP \times \overline{P'^2}^{1/2}$ , we can tell the significance of the contribution of mooring motion to the temperature peaks. These values are listed in Table A.1. For the three records (5482, 5792, and 5492) where mooring motion is strong and the T-P coherence is high, the temperature fluctuations are mainly caused by mooring motion; with weak mooring motion and low T-P coherence, the temperature fluctuations at 5422 cannot be attributed to mooring motion.

Table A.1  
 Tabulation of  $\overline{T'^2}^{1/2}$  (deg),  $\overline{P'^2}^{1/2}$  (dbar),  $dT/dP$  (deg/dbar), and  $\overline{P'^2}^{1/2} \times dT/dP$  (deg) in the main thermocline for selected records.

Record	$\overline{T'^2}^{1/2}$	$\overline{P'^2}^{1/2}$	$dT/dP$	$\overline{P'^2}^{1/2} \times dT/dP$
5482	.252	9.6	.0203	.195
5792	.152	5.34	.0206	.11
5492	.1	2.91	.0202	.06
5422	.16	.586	.0187	.011

### A.3 Summary

For records from moorings with high T-P coherence with  $180^\circ$  phase difference in the inertial frequency band, a prominent inertial peak is usually observed in the temperature spectrum and is mainly caused by mooring motion. For records from moorings with low T-P coherence in the inertial frequency band, the occasional occurrence of temperature peaks is probably due to the advection of horizontal temperature gradient by the strong horizontal motion of inertial waves.

Appendix B Evaluation of Elliptic Integrals with Parameters  
Greater than One

In the calculation of the wave functions  $V(\phi)$  and  $P(\phi)$  using Eqs. (3.27) and (3.19), we need to evaluate the following three quantities  $\xi$ ,  $\frac{d\xi}{d\phi}$ , and  $\frac{d^2\xi}{d\phi^2}$ . From Eq. (3.26),

$$\frac{2}{3} \xi^{3/2} = \int_{\phi}^{\phi_s} (\sin^2 \phi_s - \sin^2 \phi') d\phi', \quad (\text{B.1})$$

we have

$$\frac{d\xi}{d\phi} = -\xi^{-1/2} (\sin^2 \phi_s - \sin^2 \phi)^{1/2}, \quad (\text{B.2})$$

and

$$\frac{d^2\xi}{d\phi^2} = -\frac{1}{2} \xi^{-1} \left( \frac{d\xi}{d\phi} \right)^2 - \frac{1}{2} \xi^{-1} \sin 2\phi \left( \frac{d\xi}{d\phi} \right)^{-1}. \quad (\text{B.3})$$

Once  $\xi$  is known,  $\frac{d\xi}{d\phi}$  and  $\frac{d^2\xi}{d\phi^2}$  can be easily calculated using Eqs. (B.2) and (B.3). The integral on the right-hand side of (B.1) is an elliptic integral of the second kind. Using the notation of Abramowitz and Stegun (1964), (B.1) can be written

$$\frac{2}{3} \xi^{3/2} = m^{-1/2} \left[ E(\phi_s, m) - E(\phi, m) \right], \quad (\text{B.4})$$

where  $m = \frac{1}{\sin^2 \phi_s}$  (hence  $m > 1$ );  $m$  is the parameter and  $\phi$  is the amplitude of the elliptic integrals. Because most of the formulae and numerical methods for the evaluation of elliptic integrals are formulated under the assumption that  $|m| < 1$ , we have to transform the elliptic integrals in (B.4) into their corresponding forms with parameters less than one.



In terms of  $u$  defined as

$$u = \int_0^{\phi} (1 - m \sin^2 \lambda)^{-1/2} d\lambda, \quad (\text{B.5})$$

we have (see Abramowitz and Stegun, 1964; p.593)

$$E(u|m) = m^{1/2} E(um^{1/2} | m^{-1}) - (m-1)u \quad ; \quad (m > 1) \quad (\text{B.6})$$

The relation between  $u$  and  $\phi$  is usually written as

$$\text{sn}(u | m) = \sin \phi, \quad (\text{B.7})$$

where  $\text{sn}$  is a Jacobian elliptic function. The integral in (B.5) is the elliptic integral of the first kind, i.e.,

$$\begin{aligned} u &= F(\phi | m) \\ &= m^{-1/2} F(\theta | m^{-1}) \quad (m > 1) \end{aligned} \quad (\text{B.8})$$

where

$$\theta = \sin^{-1}(m^{1/2} \sin \phi) \quad (\text{B.9})$$

$F(\theta | m^{-1})$  can be calculated by using a rapidly convergent series

(Dwight, 1968) :

$$F(\theta | m^{-1}) = \frac{2\phi}{\pi} K - \sin \theta \cos \theta \left( \frac{1}{2} \frac{A_1}{m} + \frac{1 \cdot 3}{2 \cdot 4} \frac{A_2}{m^2} + \frac{1 \cdot 3 \cdot 5}{2 \cdot 4 \cdot 6} \frac{A_3}{m^3} + \dots \right) \quad (\text{B.10})$$

where

$$K = \int_0^{\frac{\pi}{2}} (1 - m^{-1} \sin^2 \theta)^{-\frac{1}{2}} \text{ (complete elliptic integrals of the 1st kind)}$$

$$= \frac{\pi}{2} (1+p) \left[ 1 + \frac{1}{2^2} p^2 + \frac{1 \cdot 3^2}{2^2 \cdot 4^2} p^4 + \frac{1 \cdot 3^2 \cdot 5^2}{2^2 \cdot 4^2 \cdot 6^2} p^6 + \dots \right],$$

$$p = \frac{[1 - (1 - m^{-1})^{\frac{1}{2}}]}{[1 + (1 - m^{-1})^{\frac{1}{2}}]} ;$$

$$A_1 = \frac{1}{2} , \quad A_2 = \frac{3}{2 \cdot 4} + \frac{1}{4} \sin^2 \theta ,$$

$$A_3 = \frac{3 \cdot 5}{2 \cdot 4 \cdot 6} + \frac{5}{4 \cdot 6} \sin^2 \theta + \frac{1}{6} \sin^4 \theta .$$

with  $u$  known the remaining calculation in (B.6) is  $E(\text{um}^{1/2} | m^{-1})$ ,

which has a similar series representation :

$$E(\text{um}^{1/2} | m^{-1}) = \frac{2\phi}{\pi} E + \sin \alpha \cos \alpha \left( \frac{1}{2} \frac{A_1}{m} + \frac{1 \cdot 3}{2 \cdot 4} \frac{A_2}{m^2} + \frac{1 \cdot 3 \cdot 5}{2 \cdot 4 \cdot 6} \frac{A_3}{m^3} + \dots \right) \text{ (B.11)}$$

where  $\sin \alpha = \text{sh}(\text{um}^{1/2} | m^{-1}) ;$

$$E = \int_0^{\frac{\pi}{2}} (1 - m^{-1} \sin^2 \lambda)^{\frac{1}{2}} d\lambda \text{ (complete elliptic integral of the 2nd kind)}$$

$$= \frac{\pi}{2(1+p)} \left[ 1 + \frac{1}{2^2} p^2 + \frac{1}{2^2 \cdot 4^2} p^4 + \frac{1 \cdot 3^2}{2^2 \cdot 4^2 \cdot 6^2} p^6 + \dots \right] ;$$

$A_1, A_2, A_3 \dots$  are the same as before except that  $\sin \theta$  is replaced by  $\sin \alpha$ .

The value of  $\text{sn}(um^{1/2} | m^{-1})$  can be calculated by using the ascending (increase  $m^{-1}$ ) or descending (decrease  $m^{-1}$ ) transformations (Abramowitz and Stegun, 1964), depending on whether  $m^{-1} > 0.5$  or  $m^{-1} < 0.5$ . Then  $\text{sn}(x | r)$  can be approximated by

$$\text{sn}(x | r) \approx \sin x - \frac{r}{4} (x - \sin x \cos x) \cos x \quad (r \ll 1)$$

or

$$\text{sn}(x | r) \approx \tanh x + \frac{1-r}{4} (\sinh x \cosh x - x) \text{sech}^2 x \quad (r \approx 1).$$

References

- Abramowitz, M., and I.A. Stegun (1964). Handbook of Mathematical Functions. Appl. Math. Ser. 55, National Bureau of Standards, Washinton, D.C., 1046pp.
- Armi, L, and E. D'Asaro (1979). Flow structures of the benthic ocean. J. Geophys. Res. (in press).
- Bell, T.H. (1975). Lee waves in stratified flows with simple harmonic time dependence. J. Fluid Mech., vol. 67, 705-722.
- Bretherton, F.P., and C. Garrett (1969). Wavetrains in inhomogeneous moving media. Proc. Roy. Soc. London, Ser. A, vol. 302, 529-554.
- Briscoe, M. (1975). Preliminary results from the trimmed internal wave experiment (IWEX). J. Geophys. Res., vol. 80, 3872-3884.
- Cairns, J.L., and G.O. Williams (1976). Internal wave observations from a midwater float, 2. J. Geophys. Res., vol. 81, 1943-1950.
- Charney, J.G. (1971). Geostrophic turbulence. J. Atmos. Sci., vol. 28, 1087-1095.
- Desaubies, Y.J.F. (1975). A linear theory of internal wave spectra and coherences near the Vaisala frequency. J. Geophys. Res., vol. 80, 895-899.
- Desaubies, Y.J.F. (1976). Analytical representation of internal wave spectra. J. Phys. Oceanogr., vol. 6, 976-981.
- Dwight, H.B. (1968). Tables of Integrals and Other Mathematical Data. Macmillan, New York, 4th ed., 336pp.
- Eckart, C. (1960) Hydrodynamics of Oceans and Atmospheres. Pergamon Press, New York, 290pp.
- Ekman, V.W. (1905). On the influence of the earth's rotation on ocean currents. Ark. Mat. Astr. Fys., vol. 2, 1-52.
- Eriksen, C.C. (1978). Measurements and models of fine structure, internal gravity waves, and wave breaking in the deep ocean. J. Geophys. Res., vol. 83, 2989-3009.
- Eriksen, C.C. (1979). Evidence for a continuous spectrum of equatorial waves in the Indian Ocean. Submitted to J. Geophys. Res.
- Flattery, T.W. (1967). Hough Functions. Tech. Rep. 21, Dep. of Geophys. Sci., Univ. of Chicago, Chicago, Ill.
- Fofonoff, N.P. (1969). Spectral characteristics of internal waves in the ocean. Deep-Sea Res., supplement to vol. 16, 59-71.

- Fomin, L.M. (1973). Inertial oscillations in a horizontally inhomogeneous current velocity field. *IZV*, vol. 9, 75-83.
- Fomin, L.M., and M.T. Savin (1973). Vertical coherence of inertial motions in the ocean. *IZV*, vol. 9, 331-334.
- Fomin, L.M., and A.D. Yampol'skiy (1975). Vertical structure of inertial motions in the sea. *Oceanology*, vol. 15, 21-26.
- Fu, L.L., and C. Wunsch (1979). Recovery of POLYMODE Array III Clusters A and B. *POLYMODE News*, No. 60 (unpublished manuscript), Woods Hole Oceanogr. Inst., Woods Hole, Mass.
- Garrett, C., and W. Munk (1972 a). Space-time scales of internal waves. *Geophys. Fluid Dyn.*, vol. 2, 225-264.
- Garrett, C., and W. Munk (1972 b). Oceanic mixing by breaking internal waves. *Deep-Sea Res.*, vol. 19, 823-832.
- Garrett, C., and W. Munk (1975). Space-time scales of internal waves : a progress report. *J. Geophys. Res.*, vol. 80, 291-297.
- Garrett, C., and W. Munk (1979). Internal waves in the ocean. Annual Review of Fluid Mechanics, vol. 11, 339-369.
- Geisler, J.E., and E.B. Kraus (1969). The well-mixed Ekman boundary layer. *Deep-Sea Res.*, supplement to vol. 16, 73-84.
- Gonella, J. (1972). A rotary-component method for analysing meteorological and oceanographic vector time series. *Deep-Sea Res.*, vol. 19, 833-846.
- Hendershott, M.C. (1973). Inertial oscillations of tidal period. Progress in Oceanography, vol. 6, 1-27, Pergamon Press, New York.
- Hendry, R.M. (1975). The generation, energetics and propagation of internal tides in the Western North Atlantic Ocean. Ph.D. thesis, Massachusetts Inst. of Tech./Woods Hole Oceanogr. Inst.
- Johnson, W.R., J.C. Van Leer, and C.N.K. Mooers (1976). A cyclesonde view of coastal upwelling. *J. Phys. Oceanogr.*, vol. 6, 556-574.
- Joyce, T. (1977). CTD observations during KNORR 66 Leg II. POLYMODE News, No.33 (unpublished manuscript) Woods Hole Oceanogr. Inst., Woods Hole, Mass.
- Kamenkovich, V.M., and T.B. Tsybaneva (1975 a). Analysis of Laplace's tidal equations in a short-wave approximation (finite longitudinal wave numbers). *Oceanology*, vol. 15, 151-156.

- Kamenkovich, V.M., and T.B. Tsybaneva (1975 b). Analysis of Laplace's tidal equations in a short-wave approximation (large longitudinal wave numbers). *Oceanology*, vol. 15, 271-275.
- Kamenkovich, V.M., and A.V. Kulakov (1977). Influence of rotation on waves in a stratified ocean. *Oceanology*, vol. 17, 260-266.
- Kamenkovich, V.M., V.I. Ul'yanova, and T.B. Tsybaneva (1977). Dispersion relation for gravity and Rossby waves in the ocean. *Oceanology*, vol. 17, 256-259.
- Käse, R.H., and C.L. Tang (1976). Spectra and coherence of wind-generated internal waves. *J. Fish. Res. Board Can.*, vol. 33, 2323-2328.
- Kroll, J. (1975). The propagation of wind-generated inertial oscillations from the surface into the deep ocean. *J. Mar. Res.*, vol. 33, 15-51.
- Kundu, P.K. (1976). An analysis of inertial oscillations observed near Oregon Coast. *J. Phys. Oceanogr.*, vol. 6, 879-893.
- Lamb, H. (1932). Hydrodynamics. Cambridge Univ. Press.
- Leaman, K. (1975). The vertical propagation of inertial waves in the ocean. Ph.D. thesis. Massachusetts Inst. of Tech./Woods Hole Oceanogr. Inst.
- Leaman, K. (1976). Observations on the vertical polarization and energy flux of near-inertial waves. *J. Phys. Oceanogr.*, vol. 6, 894-908.
- Leaman K., and T. Sanford (1975). Vertical energy propagation of inertial waves. *J. Geophys. Res.*, vol. 80, 1975-1978.
- Lindzen, R. (1967). Planetary waves on beta-planes. *Mon. Weather Rev.*, vol. 95, 441-451.
- Longuet-Higgins, M.S. (1965). Planetary waves on a rotating sphere II. *Proc. Roy. Soc. London, Ser. A*, vol. 289, 40-54.
- Longuet-Higgins, M.S. (1968). The eigenfunctions of Laplace's tidal equations over a sphere. *Phil. Trans. Roy. Soc. London, Ser. A*, vol. 262, 511-607.
- Mathews, J., and R.L. Walker (1970). Mathematical Methods of Physics. W.A. Benjamin, 501pp.
- Matsuno, T. (1966). Quasi-geostrophic motions in equatorial areas. *J. Meteorol. Soc. Jap.*, 2(44), 25-43.

- McComas, C.H. (1977). Equilibrium mechanisms within the oceanic internal wave field. *J. Phys Oceanogr.*, vol. 7, 836-845.
- McComas, C.H., and F.P. Bretherton (1977). Resonant interaction of oceanic internal waves. *J. Geophys. Res.*, vol. 82, 1397-1412.
- Miles, J.W. (1974). On Laplace's tidal equations. *J. Fluid Mech.*, vol. 66, 241-260.
- Miles, J.W. (1977). Asymptotic eigensolutions of Laplace's tidal equation. *Proc. Roy. Soc. London, Ser. A*, vol. 353, 377-400.
- MODE-1 Atlas Group (1977). Atlas of the Mid-Ocean Dynamics Experiment (MODE-1). V. LEE and C. Wunsch, editors, Massachusetts Inst. of Tech., Cambridge, Mass.
- Mooers, C.N.K. (1973). A technique for the cross-spectrum analysis of pairs of complex-valued time series, with emphasis on properties of polarized components and rotational invariants. *Deep-Sea Res.*, vol. 20, 1129-1141.
- Mooers, C.N.K. (1975). Several effects of a baroclinic currents on the cross-stream propagation of inertial-internal waves. *Geophys. Fluid Dyn.*, vol. 6, 245-275.
- Moses, H.E. (1971). Vertical shear modes in inertial waves on a rotating earth. *J. Geophys. Res.*, vol. 76, 2156-2163.
- Müller, P., and D.J. Olbers (1975). On the dynamics of internal waves in the deep ocean. *J. Geophys. Res.*, vol. 80, 3848-3860.
- Müller, P., D.J. Olbers, and J. Willebrand (1968). The IWEX spectrum. *J. Geophys. Res.*, vol. 83, 479-500.
- Munk, W. (1979). Internal wave spectra at the buoyant and inertial frequencies. (unpublished manuscript).
- Munk, W., and N. Phillips (1968). Coherence and band structure of inertial motion in the sea. *Rev. Geophys.*, vol. 6, 447-472.
- Nayfeh, A. (1973). Perturbation Methods. Wiley, New York, 425pp.
- Needler, G.T., and P.H. LeBlond (1973). On the influence of the horizontal component of the earth's rotation on long period waves. *Geophys. Fluid Dyn.*, vol. 5, 23-46.
- Oduo, A.B. (1972) A qualitative analysis of the Laplace's tidal equations. *IZV., Atmospheric and Oceanic Phys.*, vol. 8, 752-754.
- Olbers, D.J. (1976). Non-linear energy transfer and the energy balance of the internal wave field in the deep ocean. *J. Fluid Mech.*, vol. 74, 375-399.

- Perkins, H. (1970). Inertial oscillations in the Mediterranean. Ph.D. thesis, Massachusetts Inst. of Tech./Woods Hole Oceanogr. Inst.
- Perkins, H. (1976). Observed effect of an eddy on inertial oscillations. *Deep-Sea Res.*, vol. 23, 1037-1042.
- Philander, S.G.H. (1978). Forced oceanic waves. *Rev. Geophys. Space. Phys.*, vol. 16, 15-46.
- Phillips, N.A. (1966). The equations of motion for a shallow rotating atmosphere and the "traditional approximation". *J. Atmos. Sci.*, vol. 23, 626-628.
- Phillips, N.A. (1968). Reply to Veronis' comments. *J. Atmos. Res.*, vol. 25, 1155-1157.
- Phillips, O.M. (1963). Energy transfer in rotating fluids by reflection of inertial waves. *Phys. Fluids*, vol. 6, 513-520.
- Phillips, O.M. (1977). *The Dynamics of the Upper Ocean*. 2nd ed., Cambridge Univ. Press, 336pp.
- Pollard, R.T. (1970). On the generation by winds of inertial waves in the ocean. *Deep-Sea Res.*, vol. 17, 795-812.
- Pollard, R.T., and Millard, R.C. Jr. (1970). Comparison between observed and simulated wind-generated inertial oscillations. *Deep-Sea Res.*, vol. 17, 813-821.
- Rosenberg, N.W. (1968). Statistical analysis of ionospheric winds II. *J. Atmos. Terres. Phys.*, vol. 30, 907-917.
- Rossby, C.G. (1938). On the mutual adjustment of pressure and velocity distributions in certain simple current systems, Part II. *J. Mar. Res.*, vol. 1, 239-263.
- Sanford, T.B. (1975). Observations of the vertical structure of internal waves. *J. Geophys. Res.*, vol. 80, 3861-3871.
- Schmitz, W.J. Jr. (1978). Observations of the vertical distribution of low frequency kinetic energy in the Western North Atlantic. *J. Mar. Res.*, vol. 36, 295-310.
- Schott, F. (1971). Spacial structure of inertial-period motions in a two layered sea, based on observations. *J. Mar. Res.*, vol. 29, 85-102.
- Spiegel, E.A., and G. Veronis (1960). On the Boussinesq approximation for a compressible fluid. *Astrophys. J.*, vol. 131, 442-447.
- Stern, M.E. (1977). Interaction of inertia-gravity waves with the wind. *J. Mar. Res.*, vol. 35, 479-498.



- Stewartson, K., and J.A. Rickard (1969). Pathological oscillations of a rotating fluid. *J. Fluid Mech.*, vol. 35, 759-773.
- Stewartson, K., and I.C. Walton (1976). On waves in a thin shell of stratified rotating fluid. *Proc. Roy. Soc. London, Ser. A*, vol. 349, 141-156.
- Thompson, R.O.R.Y. (1978). Observation of inertial waves in the stratosphere. *Q. J. R. Met. Soc.*, vol. 104, 691-698.
- Uchupi, E. (1971). Bathymetric Atlas of the Atlantic, Caribbean and Gulf of Mexico. Rept. 71-72, Woods Hole Oceanographic Inst., 10 Charts.
- US Polymode Organizing Committee (1976). US POLYMODE Program and Plan. Cambridge, Mass.
- Veronis, G. (1956). Partition of energy between geostrophic and non-geostrophic oceanic motions. *Deep-Sea Res.*, vol. 3, 157-177.
- Veronis, G. (1968). Comments on Phillips' proposed simplification of the equations of motion for a shallow rotating atmosphere. *J. Atmos. Sci.*, vol. 25, 1154-1155.
- Webster, F. (1968). Observations of inertial-period motions in the deep sea. *Rev. Geophys.*, vol. 6, 473-490.
- White, W.B. (1972). Doppler shift in the frequency of inertial waves observed in moored spectra. *Deep-Sea Res.*, vol. 19, 595-600.
- Wimbush, M., and W. Munk (1970). The benthic boundary layer. The Sea, vol. 4, part 1, New York, Wiley, 731-758.
- Wunsch, C. (1976). Geographical variability of the internal wave field: A search for sinks and sources. *J. Phys. Oceanogr.*, vol. 6, 471-485.
- Wunsch, C. (1977). Response of an equatorial ocean to a periodic monsoon. *J. Phys. Oceanogr.*, vol. 7, 497-511.
- Wunsch, C., and J. Dahlen (1974). A moored temperature and pressure recorder. *Deep-Sea Res.*, vol. 21, 145-154.
- Wunsch, C., and A.E. Gill (1976). Observations of equatorially trapped waves in Pacific sea level variations. *Deep-Sea Res.*, vol. 23, 371-390.
- Wunsch, C., and R. Hendry (1972). Array measurements of the bottom boundary layer and the internal wave field on the continental slope. *Geophys. Fluid Dyn.*, vol. 4, 101-145.
- Wunsch, C., and S. Webb (1979). The climatology of deep ocean internal waves. *J. Phys. Oceanogr.*, vol. 9, 235-243.

Biographical Note

The author was born on October 10, 1950 in Taipei, Taiwan. He attended Lung-An Elementary School, Ta-An Junior High School, and Chien-Kuo High School. He earned his B.S. degree in Physics from National Taiwan University in June, 1972. As a R.O.T.C. officer, he served in the Chinese Marine Corps for two years. He came to the United States in 1974. After finishing the first year of graduate study in Physical Oceanography at the University of Miami, he was admitted to the Joint Program in Oceanography of M.I.T./W.H.O.I.. He was married to Cecilia C. Liu on March 26, 1977.